Solution Combustion Catalysts for the Water-Gas Shift Reaction

Presented by

Marianne Werle van der Merwe

Dissertation submitted to the University of Cape Town

in partial fulfilment of the requirements

for the degree of

Master of Science in Engineering

April 2019

Supervised by:

Prof. Jack C.Q Fletcher

Dr. Jack V. Fletcher

Mr Niels Luchters

HySA/Catalysis Centre of Competence
Catalysis Institute
Department of Chemical Engineering
University of Cape Town

Synopsis

In the context of a growing world population, more sustainable solutions for energy generation are required. Fuel cells supplied with hydrogen generated from fuel processing trains have emerged as a potential medium-term solution due to their improved efficiency and lower greenhouse gas-emissions. This study focuses on the development of a compact, efficient design for fuel processing trains. More specifically, reduction in the size of the largest component, the Water Gas-Shift (WGS) reactor, which could be achieved by an increase in the catalytic activity via alternative catalyst synthesis techniques. Solution combustion synthesis (SCS) is one such technique that could be used since it allows for the preparation of highly-dispersed Pt oxide particles on low surface area CeO_2 with a reproducible metal loading and a defined Pt particle size.

The aim of this study was to investigate the "conventional" impregnation approach of supports prepared via SCS versus the one-shot SCS approach (support and active metal prepared in one step) for the synthesis of 1 wt.% Pt/CeO_2 catalysts for the WGS reaction using a reformate feed stream. It was hypothesized that the preferential formation of metallic Pt species supported on CeO_2 can be achieved using a glycine-nitrate combustion system with excess glycine fuel (stoichiometric ratios of glycine to nitrate oxidants > 1) i.e. the Pt is reduced during the one-shot SCS approach. The catalysts were characterized by XRD, N_2-physisorption, ICP-AES, TEM and XPS, and their activity towards the WGS reaction was evaluated with a synthetic reformate stream (50 % H_2, 6.67 % CO, 6.67 % CO_2, 33.3 % H_2O, 3.36 % He).

Initial characterization results of the catalysts prepared by the one-shot SCS approach confirmed the reproducible synthesis of Pt particles supported on nano-sized CeO_2 with low surface areas. Furthermore, TEM and XPS results of the one-shot SCS prepared catalysts indicated that the Pt species were mainly present as Pt oxide particles on the surface of the CeO_2 supports. However, for combustion systems with excess fuel, formation of some metallic Pt was observed together with the more prevalent Pt oxide particles. The catalysts prepared by the "conventional" impregnation approach had higher activities towards the WGS reaction than the one shot SCS catalysts. This was attributed to the smaller Pt particles achieved using this "conventional" synthesis approach (approximately 1 nm compared to 3 nm).

One-shot SCS is a viable synthesis approach for the preparation of 1 wt.% Pt/CeO_2 catalysts as this method allows for the preparation of highly-dispersed Pt oxide particles on low surface area CeO_2 with a reproducible metal loading and a defined Pt particle size. However, the characterization results indicated that using a combustion system with excess fuel resulted in the preferential formation of Pt oxide phases as opposed to the desired metallic Pt phase, therefore refuting the hypothesis of this study. Nevertheless, it is recommended to repeat the synthesis of the 1 wt.% Pt/CeO_2 catalysts in an inert atmosphere as this has shown to favour the formation of metallic species (Cross *et al.*, 2014).

This study was unsuccessful in preparing catalysts using a glycine-nitrate one-shot SCS system that were more active than the "conventionally" prepared catalysts. However, it is recommended that other fuel types, such as urea, also be investigated. These alternative fuel types could combine the good Pt dispersion achieved using the one-shot SCS approach with potentially smaller Pt particle sizes, thereby increasing the catalyst's activity towards the WGS reaction (Vita *et al.*, 2015a).

Acknowledgements

I would like to thank my supervisors, Professor Jack Fletcher, Dr JV Fletcher and Mr Niels Luchters, for giving me the opportunity to pursue my dream of conducting research into catalyst development. I greatly appreciate your support, advice and constructive suggestions as I developed my research project. Thank you for your willingness to share your knowledge of the field. I am grateful to all my supervisors for providing me the freedom to investigate many characterization techniques, some of which sadly never made it into my final report. I would also like to specifically thank Dr JV Fletcher and Mr Niels Luchters for their assistance in my laboratory work.

I am also extremely grateful to Assoc. Prof. Stefania Specchia and Dr. Giuliana Ercolini for hosing me at the Politecnico di Torino. My experience in Italy was both invaluable professionally and personally. Thank you for demonstrating to me how to safely conduct the solution combustion synthesis reaction. Your generous hearts made me feel very welcomed in Polito. Another big thank you must go to Prof. Patricia Kooyman for obtaining the TEM and HAADF images of my samples. Your continual support and encouragement gave me the confidence that I could successfully complete my project. I would also like to thank Dr Bryan Doyle for performing the XPS measurements of my samples, and his expertise on the topic. I am grateful your willingness to answer all of my questions via email and Skype.

I would like to also thank the following people, institutions and funding sources:

- Stephen Roberts for your continual interest and availability to help.
- Technical staff at UCT: Waldo Koorts, Gideon Kaufmann, Rachel Cupido, and Portia Johnson for assisting me in setting up my laboratory space to conduct my combustion synthesis reactions.
- Sandeeran Govender for training me and assisting me with the use of the Analytical Laboratory facilities, and the fruitful discussion regarding solution combustion synthesis and various characterization techniques.
- The admin personnel who always made my life easier: Lee-Anne Kallum, Leigh Hendricks, Shireen Heugh, Belinda Davids and Bridgette Cloete. I always walked away with a smile.
- The Department of Chemical Engineering and HySA Catalysts for providing the use of their facilities and resources.
- Thank you to HySA Catalysis for funding my research and travel opportunities.
- Thank you to the Ada & Bertie Levenstein bursary and the National Research Fund for the financial support.
- Benjamin Hall and Cara Bea Davidson for their input, advice and support during my write-up.

Finally, I would like to thank my family for their continual encouragement and invaluable support during my Master's.

"Trust in the Lord with all your heart, and lean not on your own understanding" Proverbs 3:19

Declaration

I know the meaning of plagiarism and declare that all the work in the document, save for that which is properly acknowledged, is my own. This thesis/dissertation has been submitted to the Turnitin module (or equivalent similarity and originality checking software) and I confirm that my supervisor has seen my report and any concerns revealed by such have been resolved with my supervisor.

Signed by candidate

Marianne Werle van der Merwe

8 November 2018

Table of Contents

Synopsis i

Acknowledgements ii

Declaration iii

Table of Contents iv

List of Figures vii

List of Tables xi

Nomenclature xii

1. Introduction 1

2. Literature Review 3

2.1. The Hydrogen Economy and Fuel Cells 3

2.2. Fuel Processing 4

2.3. The Water-Gas Shift Reaction 5

2.4. Fundamentals of the Solution Combustion Catalyst Synthesis Method 8

2.4.1. Thermodynamic Considerations 10

2.4.2. SCS Parameters 13

2.5. Pt Supported on Ceria Catalysts by SCS 17

2.5.1. Influence of Fuel Type 17

2.5.2. Influence of Fuel-Oxidant Ratio 18

2.5.3. Influence of Oxidant Type 20

2.5.4. Phase Control 21

2.6. The Choice Precursors for One-shot SCS of Pt/CeO_2 22

3. Research Objectives, Hypothesis and Key Questions 24

4. Experimental Methodology 25

4.1. Support and Catalyst Synthesis 25

4.1.1. Incipient Wetness Impregnation 27

4.1.2. Solution Combustion Synthesis Method 27

4.2. Catalyst Characterization 29

4.2.1. Thermogravimetric Measurements 29

4.2.2. X-Ray Diffraction (XRD) 29

4.2.3. BET Surface Area 29
4.2.4. Inductively Coupled Plasma – Atomic Emission Spectroscopy (ICP-AES) 30
4.2.5. Transmission Electron Microscopy 31
4.2.6. X-Ray Photoelectron Spectroscopy (XPS) 31
4.3. Catalyst Performance Evaluation 33
5. Results 35
5.1. Reproducibility 35
5.2. Thermogravimetric Measurements 35
5.2.1. Cerium (III) Nitrate Hexahydrate 35
5.2.2. Cerium (IV) Ammonium Nitrate 37
5.2.3. Glycine 39
5.3. Characterization of the CeO_2 supports 40
5.3.1. Thermogravimetric measurements 40
5.3.2. X-Ray Diffraction 43
5.3.3. Brunauer-Emmet-Teller Specific Surface Area 44
5.4. Characterization of the Catalysts 45
5.4.1. Thermogravimetric measurements 45
5.4.2. X-Ray Diffraction 48
5.4.3. Brunauer-Emmet-Teller Specific Surface Area 49
5.4.4. Inductively Coupled Plasma – Atomic Emission Spectroscopy 50
5.4.5. Transmission Electron Microscopy 52
5.4.6. X-Ray Photoelectron Spectroscopy 53
5.5. Water-Gas Shift Activity Measurements 56
6. Discussion 58
7. Conclusions and Recommendations 62
8. References 63
Appendix A: Summary of the Synthesis Redox Reactions 71
A.1. Redox Reactions 71
A.1.1. Synthesis of CeO_2 (SCS, CN+GLC) supports: 71
A.1.2. Synthesis of CeO_2 (SCS, CAN+GLC) supports: 71

A.1.3. Synthesis of SCS (CN+GLC) catalysts: 72
A.1.4. Synthesis of SCS (CAN+GLC) catalysts: 73
A.2 Chemicals Used 74
Appendix B: Stainless-steel Mesh Cage Design 75
Appendix C: Summary of the Characterizations 76
C.1. X-Ray Diffractograms 76
C.2. N_2-physisorption 78
C.2.1. N_2 adsorption-desorption isotherms 78
C.2.2. Linearized BET fitted isotherms 79
C.3 Transmission Electron Microscopy Images 81
C.3.1.1. Background theory of TEM 81
C.3.1.2. Bright-field and HAADF Images 82
C.3.1.2. Pt particle size distributions 88
C.4 XPS Spectra 90
C.4.1. Theoretical Background of XPS 90
C.4.2. Raw XPS Spectra 94
C.4.3. Fitted Peak Parameters 96
C.5. Summary of Characterizations 98
Appendix D: Water Gas-Shift Activity Evaluation 99
D.1. Catalyst Loading Procedure 99
D.2. WGS Temperature Programme 100
D.3. Catalyst loading sheet 101
Appendix E: EBE Faculty “Assessment of Ethics in Research Projects Form” 102

List of Figures

Figure 2.1: Schematic of a polymer electrolyte membrane (PEM) fuel cell (Larminie and Dicks, 2003) 4

Figure 2.2: Schematic of three-step fuel processor train and fuel cell configuration..... 5

Figure 2.3: Combustion ignition modes: (a) external heating and (b) local ignition..... 9

Figure 2.4: Temperature-time profiles of (a) external heating and (b) VCS mode (Varma *et al.*, 2016) 9

Figure 2.5: Calculated adiabatic flame temperatures for the synthesis of CeO_2 using CAN+GLC and CN+GLC combustion systems varying fuel-oxidant ratios (φ) (Kang, Ozgur and Varma (2018). 13

Figure 2.6: Effect of the fuel-oxidant ratio on the nature of combustion 16

Figure 4.1:Different approaches for the synthesis of 1 wt.% Pt/CeO_2 catalysts..... 25

Figure 4.2 Schematic of the supports and catalysts synthesized within this study; solid black lines denote sets, coloured boxes denote subsets..... 26

Figure 4.3 Naming system of the sets of CeO_2 supports, IWI catalysts and SCS catalysts..... 27

Figure 4.4:Solution Combustion Synthesis process 27

Figure 5.1: TGA-DTG-DTA curves of cerium (III) nitrate hexahydrate in N_2 (100 Sml/min) at 10 °C/min heating rate. For the theoretically calculated composition changes at the indicated points see Table 5.1..... 36

Figure 5.2: TGA-DTG-DTA curves of cerium (IV) ammonium nitrate in N_2 (100 Sml/min) at 10 °C/min heating rate. For the theoretically calculated compositions at the indicated points, see Table 5.2.... 38

Figure 5.3: TGA-DTG-DTA curves of glycine in N_2 (100 Sml/min) at 10 °C/min heating rate..... 39

Figure 5.4: TGA-DTG-DTA curves of the CeO_2 (CN+GLC) supports synthesized using varying fuel-oxidant ratios..... 41

Figure 5.5: TGA-DTG-DTA curves of the CeO_2 (CAN+GLC) supports synthesized using varying fuel-oxidant ratios..... 42

Figure 5.6: XRD crystallite size of the CeO_2 supports synthesized using (a) varying furnace temperatures and (b) varying Ce-precursors (CN and CAN) and fuel-oxidant ratios (φ = 0.5, 1, 1.25). 43

Figure 5.7: BET surface areas of the CeO_2 (CN+GLC) and CeO_2 (CAN+GLC) supports determined by N_2-physisorption..... 45

Figure 5.8: TGA-DTG-DTA curves of the SCS (CN+GLC) catalysts supports synthesized using varying fuel-oxidant ratios..... 46

Figure 5.9: TGA-DTG-DTA curves of the SCS (CAN+GLC) catalysts supports synthesized using varying fuel-oxidant ratios. 47

Figure 5.10: XRD crystallite sizes of the sets of (a) SCS and (b) IWI catalysts. 48

Figure 5.11: BET surface areas of the sets of (a) SCS and (b) IWI catalysts..... 49

Figure 5.12: Fitted C 1s spectrum of the (a, c, e) SCS (CAN+GLC) catalysts and (b, d, f) SCS (CN+GLC) catalysts. 53

Figure 5.13: Fitted Pt 4f spectrum of the (a, c, e) SCS (CAN+GLC) catalysts and (b, d, f) SCS (CN+GLC) catalysts. 55

Figure 5.14: The CO conversion versus time-on-stream (in hours of the SCS and IWI catalysts. 56

Figure 8.1: Stainless-steel Mesh Cage 75

Figure 8.2: XRD diffraction patterns of CeO_2 (SCS) powders synthesized using cerium nitrate hexahydrate (CN) and a fuel-oxidant ratio = 0.50 with varying furnace temperatures (400 °C, 500 °C, 600 °C, 700 °C) with the referenced pattern for cubic CeO_2 (JCPDS01-081-0792). 76

Figure 8.3: XRD diffraction patterns of CeO_2 (SCS) powders synthesized using cerium nitrate hexahydrate (CN) and cerium (IV) ammonium nitrate (CAN) and varying fuel-oxidant ratios (φ = 0.50, 1.00, 1.25) with the referenced pattern for cubic CeO_2 (JCPDS01-081-0792)..... 76

Figure 8.4: XRD diffraction patterns of 1 wt.% Pt/CeO_2 (SCS) powders synthesized using cerium nitrate hexahydrate (CN) and cerium (IV) ammonium nitrate (CAN) and varying fuel-oxidant ratios (φ = 0.50, 1.00, 1.25) with the referenced pattern for cubic CeO_2 (JCPDS01-081-0792)..... 77

Figure 8.5: XRD diffraction patterns of 1 wt.% Pt/CeO_2 (IWI) powders with the referenced pattern for cubic CeO_2 (JCPDS01-081-0792). 77

Figure 8.6: N_2-physisorption isotherms of the set of CeO_2 supports synthesized using cerium nitrate hexahydrate (CN) and cerium (IV) ammonium nitrate (CAN) and varying fuel-oxidant ratios (φ = 0.5, 1, 1.25). 78

Figure 8.7: N_2-physisorption isotherms of the set of SCS catalysts synthesized using cerium nitrate hexahydrate (CN) and cerium (IV) ammonium nitrate (CAN) and varying fuel-oxidant ratios (φ = 0.5, 1, 1.25). 78

Figure 8.8: N_2-physisorption isotherms of the set of IWI catalysts synthesized using the set of CeO_2 supports synthesized using cerium nitrate hexahydrate (CN) and cerium (IV) ammonium nitrate (CAN) and varying fuel-oxidant ratios (φ = 0.5, 1, 1.25). 78

Figure 8.9: Linearized BET fitted isotherms of CeO_2 supports synthesized using cerium nitrate hexahydrate (CN) and cerium (IV) ammonium nitrate (CAN) and varying fuel-oxidant ratios (φ = 0.5, 1, 1.25). 79

Figure 8.10: Linearized BET fitted isotherms of SCS catalysts synthesized using cerium nitrate hexahydrate (CN) and cerium (IV) ammonium nitrate (CAN) and varying fuel-oxidant ratios (φ = 0.5, 1, 1.25). 79

Figure 8.11: Linearized BET fitted isotherms of IWI catalysts synthesized using cerium nitrate hexahydrate (CN) and cerium (IV) ammonium nitrate (CAN) and varying fuel-oxidant ratios (φ = 0.5, 1, 1.25). 79

Figure 8.12: (A) Bright field TEM images and corresponding (B) HAADF images of the SCS (CAN+GLC, 0.5) catalyst. 82

Figure 8.13: (A) Bright field TEM images and corresponding (B) HAADF images of the SCS (CAN+GLC, 1) catalyst. 82

Figure 8.14: (A) Bright field TEM images and corresponding (B) HAADF images of the SCS (CAN+GLC, 1.25) catalyst. 83

Figure 8.15: (A) Bright field TEM images and corresponding (B) HAADF images of 1.0 wt.% Pt/CeO_2 (SCS, CN–0.50) catalyst..... 83

Figure 8.16: (A) Bright field TEM images and corresponding (B) HAADF images of 1.0 wt.% Pt/CeO_2 (SCS, CN–1.00) catalyst..... 84

Figure 8.17: (A) Bright field TEM images and corresponding (B) HAADF images of 1.0 wt.% Pt/CeO_2 (SCS, CN–1.25) catalyst..... 84

Figure 8.18: (A) Bright field TEM images and corresponding (B) HAADF images of 1.0 wt.% Pt/CeO_2 (IWI, CN–0.50) catalyst..... 85

Figure 8.19: (A) Bright field TEM images and corresponding (B) HAADF images of 1.0 wt.% Pt/CeO_2 (IWI, CN–1.00) catalyst..... 85

Figure 8.20: (A) Bright field TEM images and corresponding (B) HAADF images of 1.0 wt.% Pt/CeO_2 (IWI, CN–1.25) catalyst..... 86

Figure 8.21: (A) Bright field TEM images and corresponding (B) HAADF images of 1.0 wt.% Pt/CeO_2 (IWI, CAN–0.50) catalyst. 86

Figure 8.22: (A) Bright field TEM images and corresponding (B) HAADF images of 1.0 wt.% Pt/CeO_2 (IWI, CAN–1.00) catalyst. 87

Figure 8.23: (A) Bright field TEM images and corresponding (B) HAADF images of 1.0 wt.% Pt/CeO_2 (IWI, CAN–1.25) catalyst. 87

Figure 8.24: Pt particle size distributions of the SCS (CN+GLC) catalysts: (a) φ = 0.50, 99 particles counted, (b) φ = 1.00, 256 particles counted and (c) φ = 1.25, 296 particles counted. 88

Figure 8.25: Pt particle size distributions of the SCS (CAN+GLC) catalysts: (a) φ = 0.50, 88 particles counted, (b) φ = 1.00, 86 particles counted and (c) φ = 1.25, 186 particles counted. 88

Figure 8.26: Pt particle size distributions of the IWI (CN+GLC) catalysts: (a) φ = 1.00, 233 particles counted and (b) φ = 1.25, 39 particles counted. 88

Figure 8.27: Pt particle size distributions of the IWI (CAN+GLC) catalysts: (a) φ = 0.50, 80 particles counted and (b) φ = 1.00, 1032 particles counted. 89

Figure 8.28: Photoelectric Effect: Initial adsorption of a photon and resultant ejection of an Oxygen 1s level photoelectron and the secondary emission of an Auger electron due to relaxation. 90

Figure 8.29: Survey spectra of SCS (CAN+GLC, 1) catalyst. 91

Figure 8.30: The Linear, Shirley and Tougaard spectral background subtraction methods. 93

Figure 8.31: Raw C 1s spectrum of the (a, c, e) SCS (CAN+GLC) catalysts and (b, d, f) SCS (CN+GLC) catalysts. 94

Figure 8.32: Raw Pt 4f spectrum of the (a, c, e) SCS (CAN+GLC) catalysts and (b, d, f) SCS (CN+GLC) catalysts. 95

Figure 8.33: Reactor tube packing layers 99

Figure 8.34: Flowrence Water Gas Shift Operating Procedure 100

List of Tables

Table 2.1: Elemental oxidizing and reducing Valences 10

Table 2.2: Fuels commonly used in SCS 14

Table 2.3: Common Ce-precursors 15

Table 4.1: Feed composition for the WGS reaction and the volumetric flow rates for each reactor ... 33

Table 4.2: Operating conditions 34

Table 5.1: Evaluation of the TGA curves of cerium (III) nitrate hexahydrate (see Figure 5.1). 37

Table 5.2: Evaluation of the TGA curves of cerium (IV) ammonium nitrate using the postulation posed by Pokol, Leskelä and Niinistö (1994) (see Figure 5.2). 38

Table 5.3: Evaluation of the TGA curves of the set of CeO_2 supports (see Figure 5.4 and Figure 5.5). 42

Table 5.4: Evaluation of the TGA curves of the set of SCS catalysts (see Figure 5.8 and Figure 5.9).... 47

Table 5.5: Pt loadings of the sets of SCS and IWI catalysts determined from ICP-AES analysis. 51

Table 5.6: TEM determined average Pt particle size for the sets of SCS and IWI catalysts. 52

Table 5.7: Valence distribution of the Pt species (the Pt^0, Pt^{2+} and Pt^{4+} contributions) of the set of SCS catalysts. 55

Table 5.8: Average CO conversions of the IWI and SCS catalysts 57

Table 8.1: Chemicals used 74

Table 8.2: Fitted BET “c” constant 80

Table 8.3: C 1s Fitted Singlet Peak Parameters 96

Table 8.4: Pt 4f Fitted Doublet Peak Parameters 97

Table 8.5: Summary of morphological properties of the CeO_2 supports, and IWI and SCS catalysts ... 98

Table 8.6: Water-Gas Shift operating procedure steps 100

Table 8.7: Catalyst loading sheet of the IWI and SCS catalysts for the WGS activity measurements 101

Nomenclature

Symbol	Description
R^2	Goodness of fit constant
%	Percentage
ΔE_0	Natural line width of a photoelectron peak
∑	Sum of
°	Degree (radian)
°/min	Degree (radian) per minute
°C	Degree Celsius
°C/min	Degree Celsius per minute
A_{CS}	Mean cross-sectional area occupied by a molecule (nm^2)
Ar	Argon
BE	Binding energy
BET	Brunauer-Emmett-Teller
BF-STEM	Bright-field scanning transmission electron microscopy
BF	Bright-field
c	BET constant (dimensionless)
C	Carbon (element)
C 1s	Photoelectron peak ascribed to the 1s orbital of carbon
CAN	Ammonium cerium nitrate
Ce	Cerium (element)
CeO_2	Cerium (IV) oxide
c_{light}	Speed of light
cm	Centimetre
cm^3	Cubic millimetre
CN	Cerium nitrate hexahydrate
CO	Carbon monoxide
DTA	Differential thermal analysis
DTG	Differential thermogravimetric analysis
eV	electron volts
FEG	field emission gun

F_i	Molar flow rate of component i (mol/s)
FWHM	Full width half maximum
g	Gram
GC	Gas chromatograph
GL	Gaussian-Lorentzian ratio
GLC	Glycine
h	Planck's constant
H_2	Hydrogen
H_2O	Water
HAADF	High-angle annular dark-field
HCl	Hydrochloric acid
He	Helium
HNO_3	Nitric acid
I_0	Intensity of the photoelectrons emanating from the surface atoms
ICP-AES	Inductively Coupled Plasma – Atomic Emission Spectrometry
$I_{depth\ d}$	Intensity of the photoelectrons originating from a depth, d
IWI	Incipient wetness impregnation
j	Total angular momentum
K	Shape factor (0.9)
KE	Kinetic energy
kV	kilo Volts (1000 volts)
L	Litre
λ	Wavelength of radiation
l	Electron angular momentum
$\lambda_{K\alpha 1}$	Wavelength of Kα1 x-ray
M	Multiplicity of the p, d and f orbitals
m^2/g	Square meters per gram
mA	Milliamperes
mg	Milligram
M_i	Molecular mass of component i (g/mol)
min	Minute

ml	Millilitre
mm	Millimetre
ms	Milliseconds
MS5A	Molsieve 5A
n	Sample size
N_2	Nitrogen
N_A	Avogadro's constant
nm	Nanometre (1 x 10^{-9} m)
OSC	Oxygen storage capacity
p	Partial vapour pressure
p/p_0	Relative pressure
p_0	Saturation pressure
psi	Pounds per square inch
Pt	Platinum (element)
Pt 4f	Photoelectron peak ascribed to the 4f orbital of platinum
Pt^0	Metallic platinum (oxidation state = 0)
Pt^{2+}	Oxidized platinum (oxidation state = 2+)
Pt^{4+}	Oxidized platinum (oxidation state = 4+)
Pt-Cl	Chloroplatinic acid
Pt-n	Tetra ammine platinum (II) nitrate, $Pt(NH_3)_4(NO_3)_2$
rpm	Revolutions per minute
S	Slope
s	Second
s	Electron spin quantum number
SCS	Solution combustion synthesis
$SGHSV_{wet}$	Standard wet gas hourly space velocity
Sml	Millilitre at standard temperature and pressure
Sml/min	Millilitre at standard temperature and pressure per minute
STEM	Scanning transmission electron microscopy
STP	Standard temperature and pressure (0 °C and 1 atm)
TCD	Thermal conductivity detector

TEM	Transmission electron microscopy
TGA	Thermogravimetric analysis
u	Atomic unit of mass
UHV	Ultra-high vacuum
$V_{catalyst}$	Volume of catalyst (cm^3)
VCS	Volume combustion synthesis
V_i	Volumetric flow rate of component i (cm^3/hour)
v_m	Volume of gas for a monolayer coverage
vol.%	Volume percentage
W	Catalyst weight
wt	Weight
wt.%	Weight percentage
$\bar{x}$	Average
X_{CO}	Percentage conversion of CO
x_i	i^{th} data value
XPS	X-Ray Photoelectron Spectroscopy
YI	y-intercept
β	Full width half maximum of diffraction peak
θ	Diffraction peak angle
λ_{IMFP}	Inelastic Mean Free Path (IMFP)
µA	Microamperes
µm	Micrometre (1×10^{-6} m)
ν	Frequency of radiation
ρ_{STP}^{vap}	Density of vapour at STP (g/dm^3)
τ	Lifetime of core hole (s)
φ	Fuel-oxidant ratio
χ^2	chi-squared value (goodness of fit)

1. Introduction

Due to a growing global population (9 billion by 2040), the world's primary energy demand is expected to increase by 30 % by 2040 according to the *World Energy Outlook 2016* report by the International Energy Agency (2016). This growing demand for fossil fuels by developed and developing nations puts a strain on fossil fuel reserves. The progressive depletion of fossil fuel reserves will result in future increases in fuel costs and could lead to economy destabilization of the many countries who rely heavily on fossil fuels as their primary means of energy generation.

In view of the demand for more fossil fuels to sustain a growing population, certain countries have acknowledged the large amounts of greenhouse gases generated through fossil fuel consumption has had a detrimental effect on the earth's climate. Recognizing the need to reduce greenhouse gas-emissions to combat global warming, parties of the United Nations have signed the Paris Agreement on climate change mitigation (United Nations, 2015). Most governments have since introduced new policies and regulations around carbon dioxide (CO_2) emissions as it has been identified as a key greenhouse gas contributing to global warming and climate change. The *World Energy Outlook 2016* report by the International Energy Agency (IEA) presents a future scenario of what the global energy sector would look like if all the nations adhere to the pledges they made as part of the Paris Agreement. In light of these climate change mitigation policies, the IEA's report has highlighted the predicted change in the energy source mix for the world's primary energy demand with an increase in the contribution of renewable energy sources to energy generation, such as hydro, bioenergy, solar, and wind. The need for clean and sustainable energy sources has therefore recently received significant attention to determine a viable solution to replace fossil fuels for energy generation.

Within this drive for the development of cleaner fuels and energy production technologies, hydrogen and fuel cells have gained a lot of attention due to its potentially low greenhouse gas emissions and higher efficiency in converting chemical energy into power. Development of fuel cells has mainly been focussed on the transport and small stationary power supply sectors. At the heart of these developments is a Platinum Group Metal (PGM) catalyst for fuel cell applications. South Africa has 95% of the world's PGM reserve. Recognizing their potential to become a key player in the world hydrogen economy, South Africa established their own hydrogen and fuel cell technologies programme called Hydrogen South Africa (HySA). Fuel cell developments for the African continent are focussed on small, stationary electricity generation applications for remote, off-the-grid communities who otherwise would not have access to a stable supply of electricity due to the high capital costs of extending the national electrical grids.

However, for fuel cells to be a reliable power source within these remote locations, a stable source of hydrogen is required. Hydrogen is not naturally found in abundant reserves in its diatomic form. Currently, approximately 90 % of hydrogen production arises from fossil fuel sources. It is possible to produce hydrogen from hydrocarbon sources using the energy generated from renewable energy sources such as wind, solar or biomass (Specchia, 2011), however there is very limited renewable energy generation infrastructure on the African continent. Fuel processing train technology allows for the on-board production of hydrogen for fuel cell applications from liquid hydrocarbon sources such as petroleum. In this way, the capital cost issue relating to the distribution and storage of hydrogen within Africa are eliminated and most importantly, the existing fossil fuel storage and distribution infrastructure can be utilized. For this reason, within the African context, electricity generation via a fuel processor and fuel cell train utilizing locally available fossil fuel sources provides an attractive solution.

SOLUTION COMBUSTION SYNTHESIS CATALYSTS FOR THE WATER-GAS SHIFT REACTION

One of the keys to success of fuel processing trains is the activity and efficiency of the catalysts. The performance of catalysts is intrinsically associated with their composition, structure and morphology, and these properties are directly affected by the catalyst synthesis route (Patil *et al.*, 2008). The manufacturing complexities and costs of the catalysts is a critical part of the successful development of fuel processor and fuel cell train technologies. In this study, two synthesis methods for the preparation of 1 wt.% Pt/CeO_2 catalyst for application in the Water-Gas Shift (WGS) reactor section within the fuel processor were evaluated: incipient wetness impregnation (IWI) and solution combustion synthesis (SCS). Incipient wetness impregnation is one of the most common synthesis methods used to make supported metal catalysts. Solution combustion synthesis has gained attention as a synthesis method for metal oxide and supported metal catalysts due to their ability to form nano-sized powders in a simple and fast manner with the ease of scaling up the quantities produced (Patil *et al.*, 2008; Alves *et al.*, 2013). The major difficulty with this new synthesis method is the lack of understanding of how the different combustion parameters affect the resulting powder's properties which influences it catalytic activity for the Water-Gas Shift reaction.

2. Literature Review

2.1. The Hydrogen Economy and Fuel Cells

The need to develop cleaner and efficient renewable energy generation processes comes from the drive to move the world's energy system away from a fossil fuel-based system towards a more environmentally sustainable energy-based system. The fossil fuel-based energy system has placed severe strain on the environment. Concerns regarding irreversible climate change, depleting fossil fuel reserves, and rising levels of pollution has led to the introduction environmental legislation regarding the reduction of CO_2 emissions (United Nations, 2015). This has led to the development of new energy generation processes which can be suitable replacements to the fossil fuel-based systems and meet the sustainability goals. Recently, the possibility of a hydrogen economy has received a lot of attention. The term "hydrogen economy" has been used to describe large-scale energy systems that use hydrogen as its main energy carrier (Kleijn and Voet, 2014). Hydrogen is seen as a clean energy source as it has zero emissions and therefore has been regarded as a clean alternative to fossil fuels (Kleijn and Voet, 2014).

Nevertheless, there are still concerns with the feasibility and sustainability of the implementation of such an energy generation system (Andrews and Shabani, 2011). For the implementation of this system a sustainable, reliable source of hydrogen is required. Typically, hydrogen is produced from fossil fuels though there are several renewable energy technologies which can be used to produce hydrogen, such as solar cells, wind power, biomass, etc. However, the latter technologies face several technical and economic barriers. These processes are typically very capital intensive and use niche or scarce resources which constrain scale-up and implementation to meet a continuous energy demand (Kleijn and Voet, 2014). Besides the challenges that these technologies face in producing hydrogen, a whole new series of processes, infrastructures and safety regulations are required for the transport and use of hydrogen as a fuel which all have their own challenges and limitations (Mazloomi and Gomes, 2012). Hence, it has been recommended to develop hydrogen energy systems powered from liquid fossil fuels as an intermediate solution while advances are made in addressing the challenges faced by the large-scale supply of hydrogen generated from renewable sources (Ogden, 1999). Additionally, such systems can already make use of existing fossil fuel mining and transport infrastructure reducing the capital costs of implementation.

Fuel cells are regarded as a highly efficient energy generation system with hydrogen as the fuel (Larminie and Dicks, 2003). A fuel cell converts hydrogen (H_2) and oxygen (O_2) through an electrochemical reaction into electricity and water (H_2O) over two half cells separated by an electrolyte, see Figure 2.1 (Larminie and Dicks, 2003). The anode and cathode serve as both catalysts for the half-reactions and as electrodes to transport the electrons within the fuel cell. Fuel cells are highly reliable with long life-times as there are no moving parts within the system. Fuel cell technology has been termed "clean" or free from carbon emissions as the only by-product of the main fuel cell reaction is pure water. However, it should be noted that the hydrogen generation needed for the fuel cell comes with CO_2 emissions. Fuel cells are highly efficient at converting fuel into electricity compared to conventional combustion engines and are very quiet. These two properties are important in the development of stationary power generation systems which will compete with generators for electricity generation within the African continent.

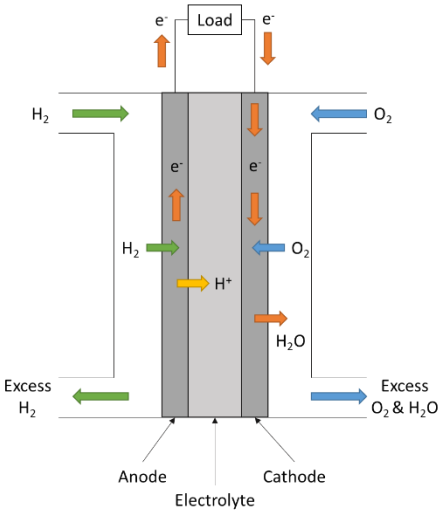

Figure 2.1: Schematic of a polymer electrolyte membrane (PEM) fuel cell (Larminie and Dicks, 2003)

The polymer electrolyte membrane (PEM) fuel cell is the most commonly used fuel cell due to its sustained high power density, low weight, low operating temperature (~ 80 °C), fast start-up, compact design, and long stack life (Faur Ghenciu, 2002; Larminie and Dicks, 2003). In PEM fuel cells, noble metal-based catalysts are used for both the anode and cathode. Development of PEM fuel cells for the application in the automotive industry and stationary power generation systems has seen remarkable progress in the last decade (Ersoz *et al.*, 2006; Specchia, 2011). Nonetheless, their success as commercial electricity generation technologies that can compete with combustion engines, steam turbines, or batteries lies in the development of efficient and inexpensive fuel processors for the on-board generation of hydrogen (Ahmed and Krumpelt, 2001; Qi *et al.*, 2007). Fuel processors can produce and purify hydrogen from hydrocarbon sources on an as-needed basis. This on-board hydrogen generation system eliminates any complexities regarding hydrogen storage and transport. Hydrogen generation from fossil fuels via fuel processors limit emissions to predominantly CO_2 with few of the harmful hydrocarbons released as observed during the combustion of fossil fuels (Faur Ghenciu, 2002).

2.2. Fuel Processing

A fuel processing train is a stage-wise set of unit reactors which produces a hydrogen rich gas stream appropriate as a feedstock for low temperature PEM fuel cells from of commonly available hydrocarbon fuels, such as liquified petroleum gas (LPG) (Larminie and Dicks, 2003; Shekhawat *et al.*, 2011). PEM fuel cells require a highly pure hydrogen stream with less than 50 ppm carbon monoxide as this is the poisoning limit of the PGM fuel cell catalyst (Faur Ghenciu, 2002). This requirement creates the need for a three-step reforming and hydrogen purification process, see Figure 2.2.

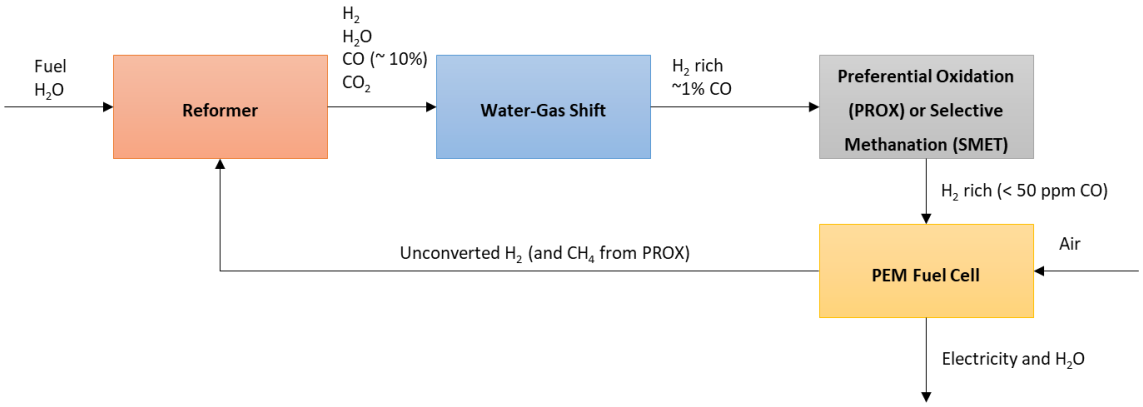

Figure 2.2: Schematic of three-step fuel processor train and fuel cell configuration

Firstly, a reformer converts a hydrocarbon feedstock into a reformate stream rich in hydrogen (H_2) with high levels of carbon monoxide (~ 10% CO). Typically, a steam reformer is used as it produces a stream with a high H_2/CO ratio which is beneficial for H_2 production (Holladay *et al.*, 2009). The reformate stream contains a large amount of water (H_2O) which is beneficial as it meets the humidity level requirements for optimal performance of the PEM fuel cell. Next, two CO clean-up stages are required to reduce the amount of CO below the required limit for a hydrogen feed to a PEM fuel cell: a water-gas shift (WGS) reactor followed by either a preferential oxidation (PROX) reactor or selective methanation (SMET) reactor. The WGS reactor reduces the amount of CO to ~ 1 vol.% with the added advantage of increasing the amount of H_2 within the stream. A PROX or SMET reactor is used to further reduce the concentration of CO to the required amount either by preferentially oxidizing CO to CO_2 (PROX) or converting CO into CH_4 (SMET).

The WGS component of the fuel processors is of most interest for size optimization as it is the largest component (Zalc and Loffler, 2002; Alijani and Irankhah, 2013). In order to develop a compact design for a fuel processor, the size of the WGS reactor needs to be reduced. A key factor contributing to the large design is the amount of catalyst required for this reaction. To reduce the amount of catalyst required, a more active catalyst needs to be developed. The activity of a catalyst is a function of its morphological properties which are determined by the synthesis method (Patil *et al.*, 2008; Lee and Yoo, 2014). The catalyst preparation method plays a critical role in determining the catalyst's activity and stability. Therefore, reduction of the size of the WGS reactor could possibly be achieved by an increase in the catalytic activity via alternative catalyst synthesis techniques.

2.3. The Water-Gas Shift Reaction

The WGS reaction is a mildly exothermic, equilibrium limited reaction (Newsome, 1980).

$$CO\ (g) + H_2O\ (g) \leftrightarrow CO_2(g) + H_2\ (g)\ \ \Delta H = -41.2\ kJ/mol \qquad \text{Equation 2.1}$$

$$K_p = exp\left(\frac{4577.8}{T} - 4.33\right) \qquad \text{Equation 2.2}$$

Industrially, two WGS stages are required for a high conversion of CO. High CO conversions are thermodynamically favoured at lower temperatures however, the reaction is kinetically limited at these lower temperatures. Hence, two reactors with inter-stage cooling are required to achieve high conversions of CO: a high temperature shift (HTS) reactor (350 – 400 °C) to drive the WGS reaction kinetically, followed by a low temperature shift (LTS) reactor (180 – 240 °C) to drive the WGS reaction

thermodynamically towards high conversions of CO (Faur Ghenciu, 2002). This two-stage reactor configuration is typically used in the ammonia process for purification of the hydrogen stream required in the Haber process (Twigg, 1989).

The classical commercial HTS catalyst formulation used in industry is an iron-chromium based catalyst (de Araújo and do Carmo Rangel, 2000; Shekhawat *et al.*, 2011). Chromium oxide is added as a stabilizer preventing sintering of the iron oxide and loss of surface area, thereby retarding deactivation of the catalyst (Bohlbro, 1969). Conventionally, copper-based catalysts are used for the LTS reaction (Twigg, 1989; Yahiro *et al.*, 2007). These copper-based catalysts have shown good activity towards the WGS reaction at low temperatures with no methanation activity (Twigg, 1989). The $Cu/ZnO/Al_2O_3$ catalysts is the most favoured catalyst formulation for the LTS reaction in industry. The preparation method has been found to influence the activity of this $Cu/ZnO/Al_2O_3$ catalysts (Shekhawat *et al.*, 2011).

For application in fuel processors, the conventional two-stage HTS and LTS reactor system is not feasible as this configuration is very large (Semelsberger and Borup, 2005; Alijani and Irankhah, 2013). Fuel processors require a single-stage reactor system for the WGS reaction. The technical importance of this WGS reactor is part of the CO clean-up requirement of the reformate stream to produce a highly pure hydrogen feedstock which can be fed to the fuel cell. The added advantage of using the WGS reaction is that while decreasing the CO content there is an increase in the yield of hydrogen.

The typical temperature range for the WGS reactor within the fuel-processing train is 280 - 320 °C (Faur Ghenciu, 2002; Alijani and Irankhah, 2013). The industrial iron-chromium and Cu-ZnO catalyst formulations are also not suitable for this medium temperature (~ 300°C) single-stage reactor system within the fuel-processor. The iron-based HTS catalyst is prone to coke formation at these lower temperatures (Smith R J *et al.*, 2010). The copper-based LTS catalyst would be kinetically limited at ~ 300 °C, which would result in the requirement of larger reactor volumes to achieve the desired CO conversion. Furthermore, the HTS and LTS catalysts are required to be activated prior to the WGS reaction through a lengthy pre-conditioning reduction process. This lengthy pre-conditioning process is undesirable for fuel processors with frequent start-up/shut-down cycles (Liu *et al.*, 2005). Additionally, the activated HTS and LTS catalysts are pyrophoric making them very sensitive to air which can lead to safety issues.

These concerns regarding the lengthy activation processes and instability of the industrial HTS and LTS catalysts render them unsuitable for the single-stage medium temperature WGS reactor. For these reasons, alternative catalyst formulations to the HTS and LTS catalyst formulations with high activities at medium temperatures (~ 300°C) towards the WGS reaction have been the focus of development for the application in fuel processors. These medium-temperature catalysts are required to be highly stable under typical reformate stream compositions with a steady outlet CO concentration, non-pyrophoric, require no pre-conditioning procedures. They are also required to be highly selective to the formation of H_2 and CO_2, with no side reactions such as methanation (Faur Ghenciu, 2002; Ladebeck and Wagner, 2013).

Most research attention has been focused on non-precious metal catalysts and precious group metal (PGM) catalysts for the WGS reaction in fuel processors (Faur Ghenciu, 2002). The aspect that separates the two groups of catalysts is cost and activity: non-precious metals are significantly cheaper than PGM catalysts but are less active at medium temperatures than PGM catalysts.

PGM catalysts have shown to able to meet these requirements for the application in fuel processors (Faur Ghenciu, 2002; Alijani and Irankhah, 2013). These catalysts shown good activity at temperatures in the range of 250 – 350 °C and are non-pyrophoric. Of these PGM catalysts, platinum (Pt) based catalysts are considered the leading catalysts for the WGS reaction due to their significantly higher activity compared to other PGM catalysts, such as Rh, Ru and Pd based catalysts (Radhakrishnan *et al.*, 2006; Shekhawat *et al.*, 2011; Xu *et al.*, 2012). For this reason, extensive studies on Pt-based catalysts for the WGS reactor in fuel processors have been done (Faur Ghenciu, 2002; Jacobs *et al.*, 2005; Azzam *et al.*, 2007; Panagiotopoulou *et al.*, 2007; Kalamaras *et al.*, 2011).

Typically, Pt is supported on various oxide supports, such as CeO_2, TiO_2, ZrO_2, and Al_2O_3 (Azzam *et al.*, 2007). These oxide supports vary in their reducibility, or in other words, the oxygen mobility within the lattice framework of the support. It is know that Pt supported on reducible metal oxide supports, such as CeO_2, are bifunctional: both the Pt metal and the reducible metal oxide support take part in the reaction (Faur Ghenciu, 2002; Kalamaras *et al.*, 2011). Most literature studies have been focussed on Pt supported on CeO_2 or modified CeO_2 supports as these catalysts have been found to be highly active towards the WGS reaction in the range of 250 – 350 °C (Panagiotopoulou *et al.*, 2007; Kalamaras *et al.*, 2011; Alijani and Irankhah, 2013). Ceria has the ability to rapidly undergo reversible reduction (from Ce^{4+} to Ce^{3+}). This reducibility creates oxygen vacancies within the crystal structure (Montini *et al.*, 2016). As ceria easily shifts between its two oxidation states (+4 and +3), it can "store" and "donate" oxygen for the oxidation of CO and hydrocarbons on the surface (Trovarelli *et al.*, 2001). This unique feature is called ceria's Oxygen Storage Capacity (OSC).

To date, various methods have been introduced and developed for the synthesis of Pt supported on CeO_2 catalysts for the WGS reaction. Traditionally, these supported metal catalysts have been prepared using step-wise unit operations (Jacobs *et al.*, 2005; Ricote *et al.*, 2006; Azzam *et al.*, 2007; Roh *et al.*, 2012). Firstly, the support is synthesized using one of several techniques such as homogeneous precipitation (Chen and Chen, 1993; Chu *et al.*, 1993; Sepúlveda-Escribano *et al.*, 1998), hydrothermal synthesis (Hirano and Kato, 1996), or sol-gel synthesis (Yu *et al.*, 2005; Meira *et al.*, 2016). Then, the metal is added to the support, typically via impregnation (Pinna, 1998; Lee and Yoo, 2014). Impregnation of the support involves contacting the support with an aqueous solution of the desired metal precursor (typically a salt). The catalyst is then activated by means of thermal treatment to decompose the metal precursor to the more active species, typically the metal oxide form (Lee and Yoo, 2014). In the case of Pt/CeO_2 catalysts for the WGS reaction, the pure metal form is the active species and therefore subsequent reduction of the metal oxide under hydrogen gas is required (Mei *et al.*, 2015). The synthesis method used for the supports must be chosen such that the supports retain their physical and crystallographic properties while undergoing the thermal and reduction preparation processes used in the step-wise conventional impregnation approach.

Previous studies have reported the used of an alternative method, namely Solution Combustion Synthesis, for the preparation of effective and durable Pt/CeO_2 catalysts for the WGS reaction (Bera *et al.*, 2004; Gayen *et al.*, 2010). The advantages of SCS over the conventional impregnation approach is the method's simplicity, short preparation times and versatility (Patil *et al.*, 2008; Alves *et al.*, 2013). SCS can be used to synthesize CeO_2 supports which can be used in the conventional impregnation approach (Purohit *et al.*, 2001; Kang *et al.*, 2018), or to prepare Pt/CeO_2 catalysts in a single-step approach called one-shot SCS where the support and the active metal are prepared simultaneously in one step (Bera *et al.*, 2004; Gayen *et al.*, 2010).

These studies reported Pt/CeO_2 catalysts with highly dispersed Pt particles on highly crystalline CeO_2 supports. Gayen *et al.* (2010) concluded that these properties of the one-shot SCS Pt/CeO_2 catalysts made them competitive with the conventional impregnated catalysts for the WGS reaction.

2.4. Fundamentals of the Solution Combustion Catalyst Synthesis Method

Solution Combustion Synthesis (SCS) was accidently discovered the late 1980s. Kingsley and Patil (1988) placed a mixture of aluminium nitrate and urea in a muffled furnace at 500 °C and observed a combustion reaction taking place. The mixture boiled, foamed and ignited with an incandescent flame at a temperature of approximately 1350 °C, resulting in the formation of a white, fluffy powder. Kingsley and Patil (1988) identified this powder as fine α-alumina. SCS has since been used to synthesize a variety of nano-sized materials, such as metal oxides, supported metal catalysts, alloys and sulphides (Varma *et al.*, 2016). It has also been used to coat structured materials, such as cordierite monoliths (Vita *et al.*, 2014; Vita *et al.*, 2015b; Specchia *et al.*, 2017).

SCS has been defined as a self-propagating redox reaction of an aqueous solution of metal salts (oxidizers) and fuel(s) (reducing agents) which results in the formation of nanocrystalline solid oxide materials (Alves *et al.*, 2013). SCS has several key defining features that distinguishes it from other synthesis methods (Mukasyan and Dinka, 2007; Varma *et al.*, 2016). The molecular level mixing, due to the aqueous nature of starting solution, allows for the formation of highly uniform solids on the nanoscale (Mukasyan and Dinka, 2007). Furthermore, due to the high reaction temperatures, products with a high degree of crystallinity and purity are synthesized. Additionally, calcination as a final thermal treatment is often not required as the desired phase composition is already achieved after SCS (Mukasyan and Dinka, 2007). Lastly, highly porous nano-sized powders are synthesized due to the large amount of gases that are generated within the short duration of the combustion reaction. These gases inhibit particle growth, break up any agglomerates formed and create nano-sized pores within the particles (Alves *et al.*, 2013).

SCS is also often called Volume Combustion Synthesis (VCS) within literature (Varma *et al.*, 1998; Patil *et al.*, 2008; Alves *et al.*, 2013). This was used to specifically describe the method of ignition of SCS by uniform, external heating of the solution (see Figure 2.3 (a)). Another method of ignition commonly used is local ignition of the solution (usually by means of a heated tungsten wire) resulting in a self-propagating combustion wave proceeding through the solution.

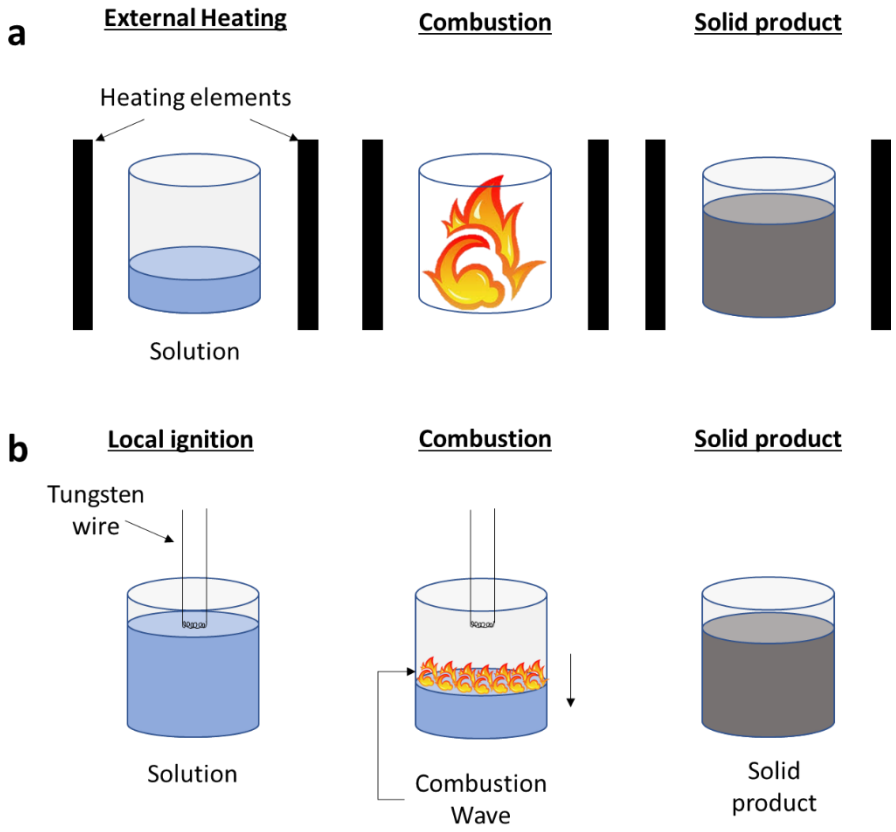

Figure 2.3: Combustion ignition modes: (a) external heating and (b) local ignition.

The temperature-time profiles of two different combustion ignition modes are very similar (see Figure 2.4). The profiles are characterized by a quick, sharp rise in temperature as the combustion mixture ignites.

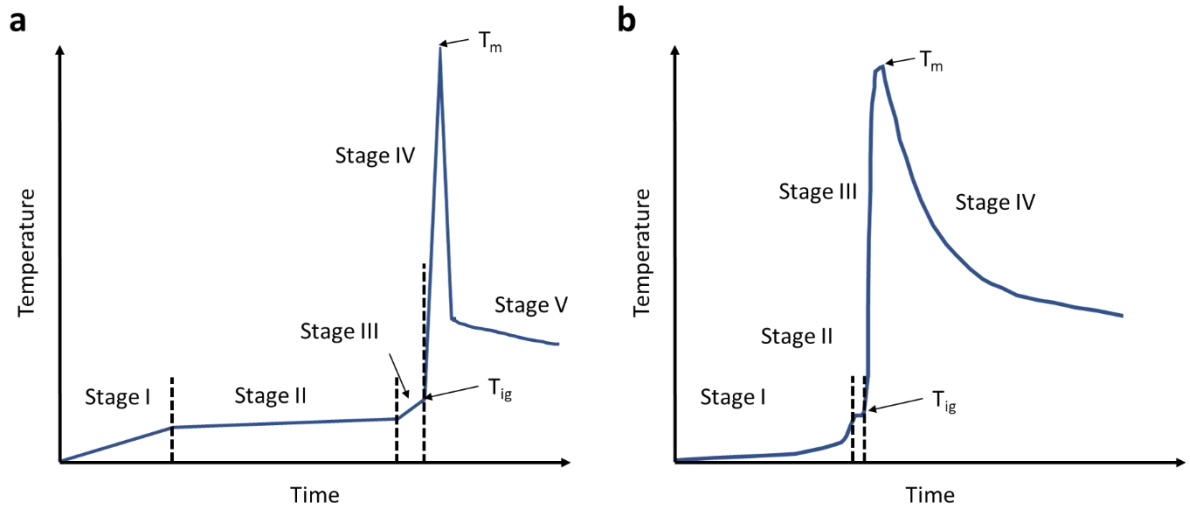

Figure 2.4: Temperature-time profiles of (a) external heating and (b) VCS mode (Varma *et al.*, 2016)

The key difference in the temperature-time profiles is the time taken for the "dehydration" of the solution (evaporation of the free water of solution and hydration water of the precursors). In the external heating ignition mode, there is a longer period in which the dehydration takes place. Firstly,

the temperature of the solution increases (Stage I) to the point where evaporation of the water occurs. Then, the temperature of the solution remains constant for a long period of time (Stage II) whilst the free and bound water evaporates. The next stage (Stage III) is heating of the viscous gel, followed by ignition of the mixture (ignition temperature: T_{ig}). The combustion reaction's temperature rapidly increases to its maximum value (T_m) followed by rapid cooling (Stage V) of the solid product after the combustion reaction. In the local ignition mode, the temperature of a small volume of the solution rapidly increases (Stage I) as it is locally heated to initiate the combustion reaction. The free and bound water in the small volume of solution rapidly evaporates (Stage II) prior to ignition of the combustion reaction. The combustion reaction propagates through the rest of the solution as a combustion wave front (Stage III).

SCS is considered an attractive synthesis method for catalysts due to the simple nature of the synthesis route and short reaction times. The composition, homogeneity, morphology, and stoichiometry of the products can be tuned, and they exhibit good crystalline and high purity. Moreover, the process is also easily scaled up which makes it economically attractive (Aruna and Mukasyan, 2008; Patil *et al.*, 2008).

2.4.1. Thermodynamic Considerations

For any sustained combustion reaction to occur, three elements need to be present simultaneously: heat, oxygen and fuel, often referred to as the "fire triangle". Heat is required to raise a materials' temperature to its ignition point. The presence of the fuel and oxygen is required to sustain the combustion reaction. If any of these elements are not present, the exothermic reaction cannot occur.

SCS is unique as it has all three elements present within the solution itself. The oxygen required for the fuel to burn is provided *in-situ* by means of the oxidants; and the heat released by the redox reaction is larger than the heat required to sustain the reaction. Hence, SCS is defined as a self-propagating redox reaction that takes place between fuel and oxidants (Patil *et al.*, 2008). Nonetheless, heat is still required to initiate the reaction.

To understand this complex exothermic reaction, the principles of propellant chemistry are often used to describe the reactions taking place in SCS (Patil *et al.*, 2008). The heat of reaction is directly linked to the fuel-oxidant ratio of the redox reaction, which is the ratio in which the fuel and the oxidants are mixed in solution. Jain, Adiga and Verneker (1981) developed a method of calculating the oxidizing valence (OV) of the oxidants and the reducing valence (RV) of the fuels in the redox reaction mixture, and from this calculate the fuel-oxidant ratio (φ) for redox mixture. The overall oxidizing or reducing valence is calculated as the sum of the elemental valences of the molecule. The elemental oxidizing and reducing valences used in this calculation are tabulated below:

Table 2.1: Elemental oxidizing and reducing Valences

Element	Oxidizing/Reducing Valence
C	+4
N	0
H	+1
O	-2

When calculating the oxidizing/reducing valence of a compound, hydration water is disregarded as it does not affect the overall valence of the compound. For example, the oxidizing valance of cerium (IV) ammonium nitrate ($(NH_4)_2Ce(NO_3)_6$) oxidant can thus calculated as follows:

$$OV_{(NH_4)_2Ce(NO_3)_6} = (8 \times 0) + (8 \times +1) + (1 \times +4) + (18 \times -2) = -24 \qquad \text{Equation 2.3}$$

The reducing valence of glycine ($C_2H_5NO_2$) fuel is also calculated similarly:

$$RV_{C_2H_5NO_2} = (2 \times +4) + (5 \times +1) + (1 \times 0) + (2 \times -2) = +9 \qquad \text{Equation 2.4}$$

Below is a demonstration of the method presented by Jain, Adiga and Verneker (1981) which can be used to determine the fuel-oxidant ratio for the synthesis CeO_2 using cerium (IV) ammonium nitrate as the oxidant and glycine as the fuel. For an ideal SCS reaction, it is assumed that only N_2, CO_2 and H_2O are the gaseous products formed, with O_2 either being consumed or produced depending on the fuel-oxidant ratio. First, start with the thermal decomposition reaction of the oxidant (Equation 2.5) and the combustion reaction of n mols of the fuel (Equation 2.6):

$$(NH_4)_2Ce(NO_3)_6 \rightarrow CeO_2 + 4N_2 + 4H_2O + 6O_2 \qquad \text{Equation 2.5}$$

$$nC_2H_5NO_2 + \frac{9}{4}nO_2 \rightarrow 2nCO_2 + \frac{1}{2}nN_2 + \frac{5}{2}nH_2O \qquad \text{Equation 2.6}$$

The overall SCS reaction is then given as a combination of the two equations, with O_2 written as a reactant which is consumed:

$$(NH_4)_2Ce(NO_3)_6 + nC_2H_5NO_2 + 6\left[\frac{3}{8}n - 1\right]O_2 \rightarrow CeO_2 + 2nCO_2 + \left[\frac{1}{2}n + 4\right]N_2 + \left[\frac{5}{2}n + 4\right]H_2O \qquad \text{Equation 2.7}$$

The overall reaction is then altered to be written in terms of the fuel to oxidant ratio (φ):

$$\varphi = \frac{3}{8}n \qquad \text{Equation 2.8}$$

Note that the ratio of $\frac{3}{8}$ corresponds to the ratio of the reducing and oxidizing valences of glycine (+9) and ammonium cerium nitrate (-24). Furthermore, the fuel-oxidant ratio is a function of the number of moles of glycine (n). The overall reaction can now be written in terms of the fuel-oxidant ratio rather than the number of moles of fuel (n):

$$(NH_4)_2Ce(NO_3)_6 + \frac{8}{3}\varphi C_2H_5NO_2 + 6[\varphi - 1]O_2 \rightarrow CeO_2 + \frac{16}{3}\varphi CO_2 + \left[\frac{4}{3}\varphi + 4\right]N_2 + \left[\frac{20}{3}\varphi + 4\right]H_2O \qquad \text{Equation 2.9}$$

The mixture is defined as fuel-lean for $\varphi < 1$ and fuel rich for $\varphi > 1$. Fuel-lean mixtures produce molecular oxygen, and fuel-rich mixtures require molecular oxygen from the air for complete combustion. When no molecular oxygen is produced or required, the redox mixture is defined as

stoichiometric (φ = 1). The oxygen required for the combustion of the fuel is provided *in-situ* by the thermal decomposition of the oxidant. This method presented by Jain, Adiga and Verneker (1981) has been widely used to calculate the fuel-oxidant ratio of multicomponent redox mixtures (Pino *et al.*, 2003, 2006; Jardim *et al.*, 2015; Vita *et al.*, 2015a; Vita *et al.*, 2016).

The fuel-oxidant ratio is important as it strongly influences the reaction enthalpy ($\Delta H^{\circ}_{reaction}$). The heat of the reaction is calculated from the heat of formation of the reactants ($\Delta H^{\circ}_{i,formation(products)}$) and products ($\Delta H^{\circ}_{i,formation(reactants)}$) (Fogler, 2006; Patil *et al.*, 2008):

$$\Delta H^{\circ}_{reaction} = \sum_{i} v_i \Delta H^{\circ}_{i,formation(products)} - v_i \Delta H^{\circ}_{i,formation(reactants)} \qquad \text{Equation 2.10}$$

For calculations of the heat of the reaction, it is common practice to assume complete combustion takes place and no residual carbon forms. Any side reactions, such as fuel hydrolysis and thermal decomposition reactions are also neglected. Hence, for enthalpy calculations, the ideal overall redox reaction is used (see Equation 2.9). The stochiometric coefficients (v_i) of the reactants and products are a function of the fuel-oxidant ratio (φ), see Equation 2.9. Maximum heat is released for a stoichiometric SCS system. For extreme fuel-lean cases, the reaction can be endothermic ($\Delta H^{\circ}_{reaction} > 0$); this implies there is not enough fuel present in solution and the thermal decomposition of the oxidant is the dominating reaction. Hence, there is a minimum fuel-oxidant ratio for which the redox reaction becomes exothermic ($\Delta H^{\circ}_{reaction} < 0$) and self-propagating (Hwang *et al.*, 2006; González-Cortés and Imbert, 2013).

For combustion temperature calculations, the combustion reaction is often considered to be adiabatic (Patil *et al.*, 2008). It is assumed that very little heat is transferred to the surroundings due to the short reaction time of the highly exothermic reaction. Consequently, due to the assumed thermal isolation of the system, the maximum calculated combustion temperature (T_m) is the adiabatic reaction temperature (T_{ad}) (Patil *et al.*, 2008). The adiabatic flame temperature can be calculated from the enthalpy of the reaction and the reaction temperature (Fogler, 2006; Patil *et al.*, 2008):

$$\Delta H^{\circ}_{reaction} = \int_{298\ K}^{T_{adtiabatic}} \sum_{i} v_i C_{p(products)} dT \qquad \text{Equation 2.11}$$

However, the actual flame temperature is never as high as the adiabatic flame temperature due to some heat losses to the environment, incomplete combustion and secondary reactions taking place (González-Cortés and Imbert, 2013; Varma *et al.*, 2016). Furthermore, the gas evolution has an advection effect on the reaction whereby the gas molecules carry heat away from the combustion system (Alves *et al.*, 2013; Varma *et al.*, 2016).

Thermodynamic software packages, such as "HSC Chemistry 5.11" and "Thermo", are often used to perform calculations of the enthalpy and the adiabatic flame temperature of SCS reactions as a function of varying fuel-oxidant ratio (Shiryaev, 1995; Varma *et al.*, 2016). These software packages optimize the Gibbs free energy of the combustion systems which contains multiple species in multiple phases. Below is an example of the calculation of the adiabatic flame temperature of two SCS combustion system for the synthesis of CeO_2 for varying fuel-oxidant ratios: (1) the CAN+GLC combustion system which uses cerium (IV) ammonium nitrate (CAN) as the oxidant and glycine (GLC)

as the fuel and (2) the CN+GLC combustion system which uses cerium (III) nitrate hexahydrate (CN) as the oxidant with glycine (GLC) as the fuel (Kang *et al.*, 2018).

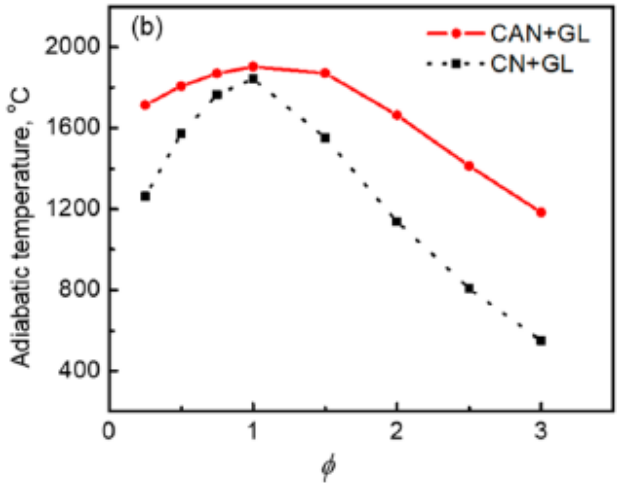

Figure 2.5: Calculated adiabatic flame temperatures for the synthesis of CeO_2 using CAN+GLC and CN+GLC combustion systems varying fuel-oxidant ratios (φ) (Kang, Ozgur and Varma (2018).

Studies which used these software packages to calculate the flame temperature obtain a maximum flame temperature for a stoichiometric fuel-oxidant ratio (González-Cortés and Imbert, 2013; Kang *et al.*, 2018). It should be noted that older studies simply used Equation 2.11 to calculate the flame temperature; these studies report linear increases in flame temperature with increasing fuel-oxidant ratio (Purohit *et al.*, 2001; Hadke *et al.*, 2015).

2.4.2. SCS Parameters

There are three parameters of the SCS reaction that strongly affect the morphology and composition of the synthesized powders: the fuel type, oxidant type and the fuel-oxidant ratio.

Fuel type

The fuel in the SCS system serves three main purposes within the redox reaction mixture, and hence, compounds require several specific properties to be regarded as a fuel for SCS (Patil *et al.*, 2008). Fuels are a source of C, N and H for combustion, which results in the formation of the gaseous products (mainly CO_2, H_2O and NO_x). Fuels aid in the homogeneous mixing by forming complexes with the metal ions in solution (Patil *et al.*, 2008; Alves *et al.*, 2013). Lastly, fuels decompose to form several key compounds which aid in the combustion reaction, such as combustible gases as HNCO and NH_3 (Patil *et al.*, 2008). Fuels therefore require the following properties to fulfil these three purposes:

- Soluble in H_2O
- Readily forms complexes with various metal ions
- Low ignition temperature (< 500 °C)
- Combustion should yield a large volume of gases
- Readily available

Typical fuels used include urea (UR), glycine (GLC) and oxalyldihydrazide (ODH). Table 2.2 tabulates the structures, reducing valences, standard enthalpy of combustion and the amount of gaseous products (CO_2, H_2O, and N_2) released due to complete combustion of 1 mol of fuel for each fuel type.

Table 2.2: Fuels commonly used in SCS

Fuel	Formula	Molecular structure	Reducing Valence	$\Delta H^{\circ}_{formation}$ (kcal/mol)	Gas Products (mol)
Glycine (GLC)	$C_2H_5NO_2$	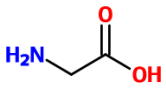	+9	-123[b]	5
Urea (UR)	CH_4N_2O	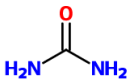	+6	-80[a]	4
Oxalyldihydrazide (ODH)	$C_2H_6N_4O_2$	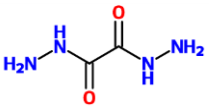	+10	-71[c]	7

a Hadke *et al.* (2015)
b Supplementary information of Morfin *et al.* (2016)
c Supplementary information of Morfin *et al.* (2016)

Below are the combustion reactions for each fuel type:

$$UR: \quad CH_4N_2O + \frac{3}{2}O_2 \rightarrow CO_2 + N_2 + 2H_2O \qquad \text{Equation 2.12}$$

$$GLC: \quad C_2H_5NO_2 + \frac{9}{4}O_2 \rightarrow 2CO_2 + \frac{1}{2}N_2 + \frac{5}{2}H_2O \qquad \text{Equation 2.13}$$

$$ODH: \quad C_2H_6N_4O_2 + \frac{5}{2}O_2 \rightarrow 2CO_2 + 2N_2 + 3H_2O \qquad \text{Equation 2.14}$$

The type of ligand groups (carboxylic acid group, -COOH; amine group, -NH_2) present in the fuel plays an important role in controlling the mixing homogeneity, the amount of gas formation and the exothermicity of the combustion reaction (Patil *et al.*, 2008; Alves *et al.*, 2013). Therefore, the choice of fuel is critical as it directly influences the properties of the resulting powders, and for this reason it has been found that some fuels are specific to certain classes of oxides. For example, it is known that urea is specific to alumina (Zhuravlev *et al.*, 2013) and other related oxides, and oxalyldihydrazide is specific for Fe_2O_3 and ferrites (Patil *et al.*, 2008; Alves *et al.*, 2013). This fuel specificity appears to be linked to the strength of the metal-ligand complexes formed within the solution (Patil *et al.*, 2008). For example, glycine can facilitate the complexation of a large amount of metallic ions due to the two different ligand groups it possesses (-COOH and -NH_2) (Alves *et al.*, 2013). When in an aqueous solution, the glycine molecule can become bipolar, or zwitterionic. The presence of both an amine and carboxylic group creates the possibility of the internal transfer of a hydrogen ion (H^+) creating the presence of both positive (-NH_3^+) and negative charges (-COO^-) at the ends of the glycine molecule. This allows the glycine molecule to create metal-ligand complexes with metal ions of various sizes, preventing any selective precipitation of compounds within the solution (Alves *et al.*, 2013). This aids in creating homogeneous powder products (Alves *et al.*, 2013).

The amount and types of ligands present also determines the volume of gases formed upon combustion of the fuel. Gas evolution has two main effects on the SCS reaction: (1) an advection effect

whereby the formed gas molecules carry heat away from the combustion system, and (2) a suppressive effect on particle agglomeration and particle growth. These two phenomena directly influence the powder's morphology, surface area and porosity (Alves *et al.*, 2013). Furthermore, the exothermicity of the SCS reaction is strongly dependent on the enthalpy of combustion of the fuel. The use of a fuel with a higher enthalpy of combustion, such as oxalyldihydrazide, results in a higher flame temperature (Vita *et al.*, 2015a). The flame temperature of a combustion reaction influences the powder's crystalline quality and particle sizes (Alves *et al.*, 2013; Hadke *et al.*, 2015; Varma *et al.*, 2016). Studies have shown that fuels that burn with higher temperatures are usually associated with combustion products with high crystalline quality and larger particle sizes (Purohit *et al.*, 2001; Murugan *et al.*, 2008; Vita *et al.*, 2015a).

Oxidant type

Within SCS, the oxidants are the metal precursors used for the synthesis of the support (and the active metal in the case of one-shot SCS). Typical oxidants are metal salts such as nitrates, sulphates and carbonates (Alves *et al.*, 2013). Nitrate metal precursors are most commonly used due to their great water solubility. For example, Table 2.3 tabulates the oxidizing valences, standard enthalpy of decomposition, and the amount of gaseous products (CO_2, H_2O, and N_2) released due to the complete decomposition of 1 mol of the two most common nitrate Ce-precursors used in SCS (cerium (III) nitrate hexahydrate, CN; and cerium (IV) ammonium nitrate, CAN).

Table 2.3: Common Ce-precursors

Support Precursor	Formula	Oxidizing valence	$\Delta H^{\circ}_{decomposition}$ (kcal/mol)	Gas Products (mol)
Cerium (III) nitrate hexahydrate (CN)	$Ce(NO_3)_3.6H_2O$	-15	-729[a]	11
Cerium (IV) ammonium nitrate (CAN)	$(NH_4)_2Ce(NO_3)_6$	-24	-620[b]	14

a Hadke *et al.* (2015)

b Supplementary information of Morfin *et al.* (2016)

Below are the decomposition reactions for the two most common Ce-precursors:

$$CN: \quad Ce(NO_3)_3.6H_2O \rightarrow CeO_2 + \frac{3}{2}N_2 + \frac{7}{2}O_2 + 6H_2O \qquad \text{Equation 2.15}$$

$$CAN: \quad (NH_4)_2Ce(NO_3)_6 \rightarrow CeO_2 + 4N_2 + 4H_2O + 6O_2 \qquad \text{Equation 2.16}$$

Likewise with the fuel choice, the choice in oxidant type (nitrate, ammonium nitrate, etc.) also influences the mixing homogeneity, amount of gas formation and the reaction enthalpy (Patil *et al.*, 2008; Alves, Bergmann and Berutti, 2013). The enthalpy of thermal decomposition of CAN is lower than that of CN (-620 kcal/mol vs 729 kcal/mol), hence a SCS combustion with this oxidant type will have a higher flame temperature (as previously shown in Figure 2.5).

Fuel-Oxidant Ratio

The occurrence of the SCS reaction is limited to specific fuel-oxidant ratios (Hwang *et al.*, 2006; Alves *et al.*, 2013). The fuel-oxidant ratio dictates whether a reaction proceeds in a fuel-lean or fuel-rich environment. If the fuel-oxidant ratio is extremely low (much less than stoichiometric ratio of oxidant and fuel), the solution cannot be ignited. The combustion system is termed fuel-lean if the fuel-oxidant is less than 1, but a reaction can still occur. In this regime, the combustion reaction is slow and is termed "smouldering" as it does not burn with a flame (see Figure 2.6, φ = 0.25, and 0.5). The slower reaction rate is due to the lower enthalpy of reaction. At fuel-oxidant ratios closer to 1, the combustion reaction starts to proceed with a flame. For stoichiometric and fuel-rich conditions ($\varphi > 1$), the combustion reaction burns with a luminous flame and maximum temperature (see Figure 2.6, φ = 1, and 1.25). Under fuel-rich conditions, the oxidants cannot provide enough *in-situ* oxygen for complete combustion of the fuel. Hence, molecular oxygen from the air is required. For fuel-rich conditions, the rate of diffusion of oxygen to the reaction zone can limit the combustion reaction to the point where for extreme fuel-rich cases the combustion reaction ceases to occur.

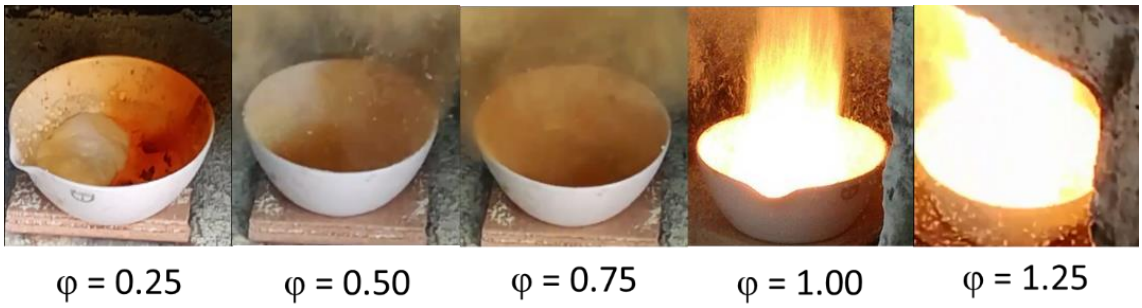

Figure 2.6: Effect of the fuel-oxidant ratio on the nature of combustion

The flame temperature of the combustion is maximized using a stoichiometric fuel-oxidant ratio. The combustion temperature affects the particle growth rate, with higher growth rates observed at higher temperatures (Alves *et al.*, 2013; Vita *et al.*, 2015a; Morfin *et al.*, 2016). The amount of gaseous products released increases with increasing fuel-oxidant ratio (Zhou *et al.*, 2014). The gas evolution is a determining factor in the formation of highly porous nano-particles as it suppresses particle agglomeration and growth. It is therefore considered that the fuel-oxidant ratio plays the most important role in controlling particle morphology (crystallite size, surface area and agglomeration of the product) as it controls the interplay between the effects of the combustion temperature and the gas evolution (Alves *et al.*, 2013).

2.5. Pt Supported on Ceria Catalysts by SCS

Over the past few decades, many literature studies have focussed on the influence of the fuel type and its concentration (the fuel-oxidant ratio) as well as the oxidant type on the particle size and microstructure of CeO_2 supports (Purohit *et al.*, 2001; Bianchetti *et al.*, 2002; Mokkelbost *et al.*, 2004; Kang *et al.*, 2018) and Pt supported on CeO_2 catalysts (Bera *et al.*, 2004; Gayen *et al.*, 2010; Nguyen *et al.*, 2015; Morfin *et al.*, 2016; Vita *et al.*, 2016). The foundation in understanding how the SCS parameters influence the properties of the powders lies in the thermodynamics of the combustion reaction (see section 2.4.1). The complex interaction of the simultaneous effects of the flame temperature and the gas evolution determines the physical properties of the synthesized powders.

2.5.1. Influence of Fuel Type

It has been theorized in several studies that for one-shot combustion-synthesized Pt/CeO_2 catalysts, the platinum either forms as (1) Pt metal clusters or (2) platinum oxide clusters on the support as separate entities or as (3) Pt ions incorporated into the CeO_2 lattice (Bera *et al.*, 2000; Bera *et al.*, 2003a). The preferential formation of Pt as either clusters or ions appears to be linked to the flame temperature of the combustion system which has been shown to be a function of fuel type (Bera *et al.*, 2004; Gayen *et al.*, 2010; Nguyen *et al.*, 2015; Morfin *et al.*, 2016).

Platinum particle formation has been observed by Morfin *et al.* (2016) and Nguyen *et al.* (2015) using a cerium (IV) ammonium nitrate and glycine combustion system (CAN+GLC). In these studies, the formation of highly dispersed platinum particles of roughly 4 nm on nanosized CeO_2 crystallites were reported. Morfin *et al.* (2016) performed MicroRaman spectroscopy on the Pt/CeO_2 catalyst synthesized using the CAN+GLC combustion system. Raman spectra of this catalyst showed a broad band across 500 – 750 cm^{-1}. Morfin *et al.* (2016) concluded that this is due to the formation of sub-stoichiometric platinum oxide species on the surface of the CeO_2 support. Morfin *et al.* (2016) further investigated the effect of using a different fuel, oxalyldihydrazide (ODH), on the formation of the platinum species. Raman spectra of this catalyst showed a lack of bands ascribed to Pt-O vibrations associated with oxidized platinum species. However, the spectra showed a band at 548 cm^{-1} ascribed to the vibration of the Pt–O–Ce bond indicating a strong interaction between the platinum species and the CeO_2 support.

A number of other studies also examined the use of a CAN+ODH combustion system for the synthesis of 1 wt.% Pt/CeO_2 catalysts (Bera *et al.*, 2000; Bera *et al.*, 2003a; Bera *et al.*, 2003b; Pino *et al.*, 2003, 2006). In these studies, the formation of stable solid solution of $Ce_{1-x}Pt_xO_{2-\delta}$ using a CAN+ODH combustion system was reported. The authors observed a lack of visual evidence of Pt clusters on CeO_2 nanosized crystallites under Transmission Electron Microscopy (TEM) studies. Rietveld refinement analysis from the X-Ray Diffraction (XRD) spectra suggested an inclusion of Pt ions into the lattice due to strong lattice contraction. The CeO_2 lattice parameters of the catalysts were smaller than the reference cubic fluorite lattice parameter. Lattice contraction occurs due to the incorporation of the smaller Pt^{2+} (0.80 Å) and Pt^{4+} (0.62 Å) cations resulting in the formation lattice defects (Zhang *et al.*, 1993; Scanlon *et al.*, 2011). Furthermore, X-Ray Photoelectron Spectroscopy (XPS) confirmed that the Pt ions were stabilized in the 2+ and 4+ oxidation states with no observation of metallic phase Pt. Extended X-ray adsorption fine structure (EXAFS) studies indicated that the coordination numbers and bond distances of the Pt, Ce and O species were consistent with $–\square–Pt^{2+}–O–Ce^{4+}–$ linkages. The results from these studies are consistent with properties of Pt cation insertion into the CeO_2 lattice structure.

In summary, Pt oxide clusters were synthesized using a glycine combustion system (Nguyen *et al.*, 2015; Morfin *et al.*, 2016) whereas Pt ions incorporated into the CeO_2 lattice were synthesized using an oxalyldihydrazide combustion system (Bera *et al.*, 2000; Bera *et al.*, 2003a; Bera *et al.*, 2003b; Pino *et al.*, 2003, 2006). The enthalpy of the oxalyldihydrazide combustion system was roughly double the corresponding glycine combustion system (ODH: $-\Delta H^0$ (298K) = 717 kcal/mol; GLC: $-\Delta H^0$ (298K) = 444 kcal/mol). The difference in reaction enthalpy of the glycine and oxalyldihydrazide combustion systems indicates that the exothermicity of the combustion reaction is a factor in determining whether Pt insertion into the crystal lattice or Pt cluster formation on ceria supports occurs during SCS (Pino *et al.*, 2006). The higher reaction enthalpy and associated higher adiabatic flame temperature of the oxalyldihydrazide combustion system provides the necessary activation energy required for the energy intensive Pt incorporation into the CeO_2 lattice (Scanlon *et al.*, 2011).

Furthermore, the fuel type not only affects the Pt species formation, but also the CeO_2 support's microstructure. Typically, smaller ceria crystallite sizes are observed for combustion systems with fuels that have lower flame temperatures. The crystallite sizes of the CeO_2 support synthesized using a urea combustion system are generally smaller than those synthesized using a glycine or oxalyldihydrazide combustion system (Purohit *et al.*, 2001; Mokkelbost *et al.*, 2004; Murugan *et al.*, 2008; Vita *et al.*, 2015a; Vita *et al.*, 2016). The lower reaction temperatures are accompanied with slower particle growth rates. Therefore, the CeO_2 supports synthesized using fuels that have lower flame temperatures result in smaller crystallite sizes and larger surface areas.

2.5.2. Influence of Fuel-Oxidant Ratio

In addition to the fuel type, its concentration relative to the oxidants in the SCS aqueous solution (the fuel-oxidant ratio) also has an effect on the properties of the synthesized metal oxides and supported metal catalysts. Many studies have been carried out regarding the influence of the fuel-oxidant ratio on the properties of metal oxides (Purohit *et al.*, 2001; Bianchetti *et al.*, 2002; Mokkelbost *et al.*, 2004; Hadke *et al.*, 2015; Kang *et al.*, 2018). However, less is reported for its effect on the supported metal catalysts.

Different trends in the support crystallite size with increasing fuel-oxidant ratio are seen for the use of different fuel types. Hadke *et al.* (2015) reported that for the synthesis of nano-crystalline nickel oxide, a maximum in NiO crystallite size was observed for a stoichiometric fuel-oxidant ratio using a glycine combustion system, with smaller crystallites observed for fuel-lean and fuel-rich fuel-oxidant ratios. On the other hand, for a urea combustion, increasing the fuel-oxidant ratio resulted in almost no change in the crystallite size. Furthermore, the nickel oxide crystallite sizes obtained using the glycine combustion system were roughly three times as larger as the crystallites obtained using the urea combustion system. Hadke *et al.* (2015) did not provide an explanation for the difference in the trends of the crystallite size with increasing fuel-oxidant ratio for the glycine and urea combustion systems. However, Hadke *et al.* (2015) did report that that the use of urea led to nickel oxide powders with a spherical shape due to the precipitation of nickel hydroxide out of solution.

The different trends in the crystallite size with increasing fuel-oxidant ratios of glycine and urea combustion systems was also observed for the synthesis of bare CeO_2 supports. The studies by Murugan *et al.* (2008), and Purohit *et al.* (2001) reported that for urea combustion systems with cerium nitrate hexahydrate as the Ce-precursor, the CeO_2 crystallite size increased with increasing fuel-oxidant ratio. On the other hand, the CeO_2 crystallite sizes synthesized using glycine combustion

systems (Hwang *et al.*, 2006; Murugan *et al.*, 2008; Kang *et al.*, 2018) indicated a maximum in crystallite size for a stoichiometric fuel-oxidant ratio, similar to the results found by Hadke *et al.* (2015) for nickel oxide powders.

It is not trivial to address the reason for the difference in trends of the crystallite size with increasing fuel-oxidant ratios for the glycine and urea combustion systems. It might be related to fuel specificity. Glycine is a better fuel to use for the synthesis of nickel oxide powders, as it doesn't allow for the precipitation of the metals out of solution as seen with the use of urea (Hadke *et al.*, 2015). It could be extrapolated that there also appears to be some fuel specificity with glycine for the synthesis of CeO_2 as the trends in crystallite sizes of CeO_2 with increasing fuel-oxidant ratio were very similar those observed for nickel oxide.

In addition to the variation in crystallite size with increasing fuel-oxidant ratios, both Hadke *et al.* (2015) and Kang *et al.* (2018) observed carbon residues on the nickel oxide and CeO_2 powders synthesized using fuel-lean and fuel-rich conditions. The results by Hadke *et al.* (2015) showed that the amount of carbon residue found on NiO powders increased with increasing fuel-oxidant ratio (determined using a LECO series 230 carbon-sulphur analyser). The use of the glycine combustion system led to a lower percentage of carbonaceous residue compared to the urea route (0.18 % vs 0.36%). Kang *et al.* (2018) investigated the influence of different Ce-precursors (CN and CAN) and the fuel-oxidant ratio on the morphological properties of bare CeO_2 supports. Kang *et al.* (2018) observed carbon residues via Raman spectroscopy for fuel-oxidant ratios of $\varphi > 2$.

In the review paper by Aruna and Mukasyan (2008), it was mentioned that calcination may be required as a final synthesis step following SCS. Calcination can be carried out as a final thermal treatment to ensure the removal of any organic species/surfactants left on the surface of the catalyst after synthesis (Pinna, 1998; Regalbuto, 2006; Lee and Yoo, 2014). Generally, it is argued that calcination is not required after SCS as the flame temperature is high enough (>> 500 °C) to decompose all of the fuel and metal precursors despite the short duration of the synthesis reaction. However, as indicated in the studies by Hadke *et al.* (2015) and Kang *et al.* (2018), there were some carbon residues left on the surface of the metal oxides (although very minimal). Calcination of the nickel oxide powders at 800 °C did result in the reduction of the carbon content to 0.09 % (Hadke *et al.*, 2015). Therefore, the possibility of the requirement of calcination as a final step following SCS cannot be disregarded.

To date, according to the knowledge of the author, only one study has been carried out on the influence of the fuel-oxidant ratio on the supported metal catalysts (Murugan *et al.*, 2008). In this study, 5 wt.% Mn/CeO_2 catalysts were synthesized with varying fuel-oxidant ratios and fuel types (glycine and urea), along with the corresponding bare CeO_2 supports. Murugan *et al.* (2008) observed similar variations in the CeO_2 crystallite size with increasing fuel-oxidant ratio for the 5 wt.% Mn/CeO_2 catalysts and the bare CeO_2 supports. The CeO_2 crystallite sizes of the 5 wt.% Mn/CeO_2 catalysts were larger than the bare CeO_2 supports for all fuel-oxidant ratios. The use of glycine to synthesize 5 wt.% Mn/CeO_2 in a one-shot approach (synthesis of both the CeO_2 support and the Mn metal) also led to the formation of the largest CeO_2 crystallite size for a stoichiometric fuel-oxidant ratio as observed for the bare CeO_2 supports. It can therefore be assumed that the presence of the Mn precursor in the glycine combustion solution does not affect the trend observed in CeO_2 crystallite size with increasing fuel-oxidant ratio.

Similar to the studies done on the synthesis of 1 wt.% Pt/CeO_2 catalyst using an oxalyldihydrazide combustion (Bera *et al.*, 2000; Bera *et al.*, 2003a; Bera *et al.*, 2003b; Pino *et al.*, 2003, 2006), Murugan *et al.* (2008) also observed the formation of highly dispersed Mn ions in the CeO_2 lattice.

Murugan *et al.* (2008) observed variations in the valence distribution of the Mn ions (differences in the contribution of the Mn^{2+}, Mn^{3+} and Mn^{4+} oxidation states) with increasing fuel-oxidant ratio. Preferential formation of the Mn^{2+} ion in the ceria lattice was observed when using a fuel-rich ($\varphi = 1.3$) glycine combustion system. This was as a result of the preferential ability of the bipolar glycine molecule to form complexes with the Mn^{2+} ion in solution. As the Mn^{2+} ion is stabilized in solution via the glycine-metal ion complex formation, the preferential formation of Mn^{2+} ions in the ceria lattice under fuel-rich conditions was observed. Varying the fuel-oxidant ratio between fuel-lean and fuel-rich ratios, varied the amount of this glycine-Mn^{2+} ion complex formation. For this reason, a variation in the valence distribution of the Mn ions (Mn^{2+}, Mn^{3+} and Mn^{4+}) was observed when varying the fuel-oxidant ratio. It was also concluded that the variations in the valence distribution were also due to several other factors: (1) the different flame temperatures at each fuel-oxidant ratio, (2) the occurrence of either combustion or thermal decomposition of the precursors depending on the conditions (either fuel-lean or fuel rich), and (3) the quenching of the combustion system due to excess fuel at high fuel-oxidant ratios. Murugan *et al.* (2008) concluded that a one-shot SCS approach can be used to tune the physical and chemical properties of the 5 wt.% Mn/CeO_2 with careful selection of the fuel type and fuel-oxidant ratio.

2.5.3. Influence of Oxidant Type

In the one-shot synthesis of Pt/CeO_2 catalysts, the Ce-precursor and the Pt salt are considered oxidants.

The typical Ce-precursors are cerium (III) nitrate hexahydrate (CN) and cerium (IV) ammonium nitrate (CAN). The use of CAN is generally associated with larger CeO_2 crystallite sizes and surface areas for bare CeO_2 supports and CeO_2 supported metal catalysts (Hwang *et al.*, 2006; Vita *et al.*, 2015a; Morfin *et al.*, 2016; Vita *et al.*, 2016; Kang *et al.*, 2018). The difference in the crystallite size and surface area has been attributed to the higher flame temperature and larger volume of gaseous product formation with the use of CAN. Kang *et al.* (2018) also reported that bare CeO_2 supports synthesized using CN and CAN had similar concentrations of Ce^{3+} in the lattice structure, indicating that there is no preferential formation of lattice defects between the two precursors.

The use of the different Ce-precursors did influence the amount of carbon residuals observed on the Ni/CeO_2 catalysts synthesized using a one-shot SCS approach. Vita *et al.* (2015a) reported that more carbonaceous residues were observed on the catalysts synthesized using the CAN precursor. The use of CAN resulted in a 6 wt.% carbon residue on the Ni/CeO_2 catalysts whereas no carbon residue was observed via temperature-programmed oxidation (TPO) with the use of CN. However, TPO is not a very sensitive technique for determining low concentrations of carbon residues on the surface of the Ni/CeO_2 catalysts. Therefore, caution should be taken when interpreting the claim that no carbon residues were observed on the catalyst synthesized using CN. As discussed earlier, carbon residues were observed via Raman spectroscopy on bare CeO_2 supports synthesized using a fuel-rich glycine combustion (Kang *et al.*, 2018). Therefore, the possibility of carbonaceous residues on CeO_2 supported metal catalysts synthesized using the CN precursor cannot be disregarded.

Other studies looked at the influence of the type of Pt salt precursor on the structure of Pt/CeO_2 catalysts (Gayen *et al.*, 2010; Morfin *et al.*, 2016). The two most common Pt-precursors used in the synthesis of Pt on CeO_2 catalysts is hexachloroplatinic (IV) acid, H_2PtCl_6, (denoted as Pt-Cl) and tetra-ammine platinum (II) nitrate, $(NH_4)_2Pt(NO_3)_2$, (denoted as Pt-n).

The use of the Pt-Cl salt as a Pt precursor has been concluded to be problematic, regardless of the synthesis route (impregnation or one-shot SCS). It has been recorded that high levels of chlorine contamination were present in 1 wt.% Pt/CeO_2 catalysts synthesized using the Pt-Cl salt in the range

of 0.3 – 0.7 wt.% chlorine (Bera *et al.*, 2000; Bera *et al.*, 2003b; Pino *et al.*, 2003; Jardim *et al.*, 2015; Morfin *et al.*, 2016). Despite calcination at 800 °C for 2 hours, Pino *et al.* (2003) found that not all of the chloroplatinic acid had dissociated. Chlorine contamination reduces the CeO_2 support's oxygen transport ability by forming CeOCl species on the surface of the ceria support (Kondarides and Verykios, 1998). For this reason, the use of Pt-Cl salt in the synthesis of Pt/CeO_2 catalysts for the WGS reaction is discouraged.

Morfin *et al.* (2016) reported that for one-shot SCS Pt/CeO_2 catalysts, the Pt salt influenced the oxidation state of the Pt species. Morfin *et al.* (2016) reported that for 1 wt.% Pt/CeO_2 catalysts prepared using the Pt-n salt, the Raman spectra showed a broad peak across 500 – 750 cm^{-1}. This was attributed to the formation of sub-stoichiometric Pt oxides. On the other hand, the catalysts prepared using the Pt-Cl salt showed sharp peaks at 591 cm^{-1} and 689 cm^{-1} which are characteristic of the vibrations of Pt-O-Ce and Pt-O bonds. Morfin *et al.* (2016) concluded that the use of the Pt-Cl salt resulted in the formation of platinum oxides on CeO_2, whereas the use of the Pt-n results in the formation of sub-stoichiometric Pt oxides.

Since Mei *et al.* (2015) reports that the active phase is metallic Pt for the WGS reaction, the sub-stoichiometric Pt oxides as seen by Morfin *et al.* (2016) suggests that Pt-n may not be suitable as a platinum precursor as an additional reduction step post SCS is required to activate the catalysts. However, as mentioned in the previous section, the ability to tune the oxidation states of the supported metal by varying the fuel-oxidant ratio has been observed for the one-shot synthesis of Mn/CeO_2 catalysts using a glycine combustion system (Murugan *et al.*, 2008). Having highlighted this aspect of SCS, the following section will address the ability of phase control that SCS provides.

2.5.4. Phase Control

SCS has shown to be able to provide the ability to *in-situ* alter the synthesised phase of the metal compound between a metal oxide, pure metal and alloy (in the case of multi-metal systems) by adjusting the SCS parameters such as the fuel type and fuel-oxidant ratio (Rao *et al.*, 2004; Murugan *et al.*, 2008; Manukyan *et al.*, 2013; Cross *et al.*, 2014; Kumar *et al.*, 2015). This involves a careful balance between SCS parameters to achieve a desired combustion environment (oxidising or reducing) to achieve a desired metal phase, while still retaining a combustion temperature and gas evolution for favourable morphological properties. It is believed that the formation of pure metals and alloys occur as secondary reactions after the formation of the initial metal oxide (Wen and Wu, 2014). The reduction of the metal oxide is brought about by either the presence of excess fuel, which acts as a reducing agent, or by presence of gaseous products which are strong reducing agents. This *in-situ* reduction of the metal oxide to metal (or alloy in the case of multi-metal systems) occurs at the combustion wave front (Kumar *et al.*, 2011; Manukyan *et al.*, 2013).

Several studies have reported the formation of pure nickel through the use of a fuel-rich glycine combustion system (Kumar, Wolf and Mukasyan, 2011; Manukyan *et al.*, 2013; Cross *et al.*, 2014). The use of glycine as a fuel results in the formation of NH_3 gas, which is a strong reducing agent (Li *et al.*, 2007; Kumar *et al.*, 2011; Manukyan *et al.*, 2013; Kang *et al.*, 2018). The thermal decomposition of glycine can be divided up into three different sections according to the thermogravimetric analysis results from Manukyan *et al.*, (2013), Kumar, Wolf and Mukasyan (2011) and Li *et al.* (2007).

The first thermal decomposition step of glycine occurs at approximately 240 – 310 °C. This corresponds to the formation of dipeptide and 2,5-piperazinedione and NH_3, H_2O and CO_2 gases via deamination and dehydration reactions of glycine:

$$C_2H_5NO_2 \rightarrow dipeptide + 2{,}5 - piperazinedione + NH_3 + H_2O + CO_2 \qquad \text{Equation 2.17}$$

The next two decomposition steps involve the formation of more gaseous products due to the further thermal decomposition of the solid products (dipeptide and 2,5-piperazinedione). At roughly 450 °C, Manukyan *et al.* (2013) reported the formation of HCN, HNCO, NH_3, H_2O and CO_2 gases, whereas Kumar, Wolf and Mukasyan (2011) and Li *et al.* (2007) reported only the formation of HCN, HNCO and CO. Nonetheless, all three studies concluded that one of the main gaseous products formed was NH_3.

The studies by Kumar *et al.* (2011) and Manukyan *et al.* (2013) concluded that the preferential formation of pure nickel as opposed to nickel oxide under fuel-rich conditions was due to *in-situ* reduction of the NiO particles to metallic Ni by the excess amounts of NH_3 gas released from the combustion of the glycine fuel. This endothermic reduction reaction occurred at temperatures greater than 450 °C:

$$3NiO + 2NH_3 \rightarrow 3Ni + 3H_2O + N_2 \qquad \text{Equation 2.18}$$

The heat required for this reaction was provided by the excess heat of the SCS reaction. Hence, a fuel-rich glycine-nitrate combustion system creates an *in-situ* reducing gaseous atmosphere which can lead to the formation of pure metals.

2.6. The Choice of Precursors for One-shot SCS of Pt/CeO_2

The review of literature studies on the synthesis of CeO_2 and Pt/CeO_2 (as well as other studies done on similar CeO_2 based catalysts) revealed that the fuel type, oxidant type and the fuel-oxidant ratio strongly influence the morphological and chemical properties of CeO_2 supports and Pt/CeO_2 catalysts. The surface areas of the CeO_2 supports can be maximized using a fuel type that has a lower flame temperature. Larger CeO_2 support surface areas are beneficial for the high dispersion of the active metal on the support. Many studies agree that the WGS reaction occurs at the interface of the CeO_2 support and the Pt species (Liu *et al.*, 2010; Kalamaras *et al.*, 2011; Jain *et al.*, 2015). Therefore, maximizing the CeO_2 support surface area and Pt dispersion is a key factor in enhancing the catalyst's activity. Furthermore, the oxidation state of the Pt species is also an important factor in determining the activity of the catalyst towards the WGS reaction. Mei *et al.* (2015) reported that catalysts with a higher percentage of the metallic phase of Pt (Pt^0) as opposed to Pt^{2+} and Pt^{4+}, had higher WGS activities.

Several studies have reported the formation of highly dispersed platinum oxide particles on nano-sized CeO_2 crystallites using a one-shot SCS system with glycine as the fuel, either CN or CAN as the Ce-precursor, and Pt-n as the Pt precursor (Gayen *et al.*, 2010; Nguyen *et al.*, 2015; Morfin *et al.*, 2016). This formation of an undesirable phase of the Pt species via one-shot SCS could possibly be altered by exploring the phase control that SCS provides.

Recent evidence suggests that the formation of NH_3 gas from the decomposition of excess glycine (fuel-rich conditions) creates a reducing gaseous environment at the combustion front, which leads to the subsequent reduction of metal oxides to their pure metal form (Kumar, Wolf and Mukasyan, 2011; Manukyan *et al.*, 2013; Cross *et al.*, 2014). Morfin *et al.* (2016) reported that for 1 wt.% Pt/CeO_2 catalysts prepared via a stoichiometric glycine-nitrate combustion system with a Pt-n salt, sub-stoichiometric Pt oxides were formed. It could also be postulated that the use of the glycine-nitrate

combustion system led to the formation of partially reduced Pt on ceria due to the formation of NH_3 gas upon the combustion of glycine which created a reducing atmosphere.

As the study by Murugan *et al.* (2008) revealed that the oxidation state of the supported metal can be altered by tuning the fuel-oxidant ratio, it is hypothesized that the use of the Pt-n salt in combination with a fuel-rich glycine-nitrate combustion system would result in the formation of a more favourable oxidation state of the Pt species (namely metal Pt particles). This could possibly result in a complete one-step preparation and activation synthesis approach, whereby the CeO_2 and Pt are synthesized in one step, as well as accomplishing the activation of the Pt/CeO_2 catalyst by means of *in-situ* reduction.

3. Research Objectives, Hypothesis and Key Questions

The aim of the study is to compare the Pt/CeO_2 catalysts prepared using the conventional impregnation approach and the one-shot SCS approach for the WGS reaction.

The objectives of this study are therefore to:

- Synthesize CeO_2 supports using the SCS method
- Synthesize 1 wt.% Pt/CeO_2 using incipient wet impregnation (IWI) of the CeO_2 support synthesized via SCS
- Synthesize active Pt nano-crystallites supported on CeO_2 supports using the one-shot SCS approach
- Determine the activity of the synthesized 1 wt.% Pt/CeO_2 catalysts towards the water-gas shift reaction

It is hypothesized that active metallic phase Pt nano-crystallites supported on CeO_2 for the water-gas shift reaction can be synthesized via the SCS method by carrying out the combustion reaction under fuel-rich conditions ($\varphi > 1$) to create a reducing environment. The reducing environment is created by the formation of NH_3 gas from the decomposition of excess glycine using a fuel-rich glycine-nitrate combustion system. To test the hypothesis above, the following key questions should be answered:

- How does the fuel-oxidant ratio affect the combustion temperature?
- Does the type of support precursor affect the crystallite size and BET surface area of the CeO_2 crystallites formed using SCS?
- Does the fuel-oxidant ratio affect the crystallite size and BET surface area of the CeO_2 crystallites formed using SCS?
- Can the BET surface area of the CeO_2 be driven to a maximum using combination of an appropriate support precursor and fuel-oxidant ratio?
- Given the available technique of XPS, can the different oxidation states of Pt (Pt^0, Pt^{2+} or Pt^{4+}) be determined?
- If the oxidation states of the Pt on ceria can be determined, does the fuel-oxidant ratio affect the type of Pt phases present on the CeO_2 surface for the catalysts prepared via one-shot SCS?
- How do the one-shot SCS Pt/CeO_2 catalysts compare to the impregnated catalysts regarding CO conversion for the water-gas shift reaction?

4. Experimental Methodology

4.1. Support and Catalyst Synthesis

The conventional approach of synthesizing metal supported catalysts is a two-step process namely, the synthesis of the support followed by impregnation of the support with the active metal. SCS has been used to synthesize a variety of metal oxide supports, however, in the last decade, a novel approach of using SCS to synthesize both the support and the active metal in a one-step approach has been explored.

The conventional approach – using incipient wetness impregnation – and the one-shot SCS approach were employed in synthesizing 1 wt.% Pt/CeO_2 catalysts in this study (see Figure 4.1). A set of cerium (IV) oxide supports (CeO_2) were prepared using SCS and are collectively denoted as "CeO_2". This set was used for characterisation of the SCS prepared ceria supports, as well as to prepare the 1 wt.% Pt/CeO_2 catalysts via conventional incipient wetness impregnation. This set of catalysts is collectively denoted as "IWI". The one-shot SCS approach of synthesizing 1 wt.% Pt/CeO_2 was also employed; this set of catalysts is collectively denoted as "SCS". Collectively, there are three sets of synthesized samples representing each step of the two different catalyst synthesis approaches which were characterized as: (1) the CeO_2 supports synthesized by SCS for the conventional two-step impregnation approach, (2) the IWI catalysts prepared from the CeO_2 supports, and (3) the one-shot SCS catalysts.

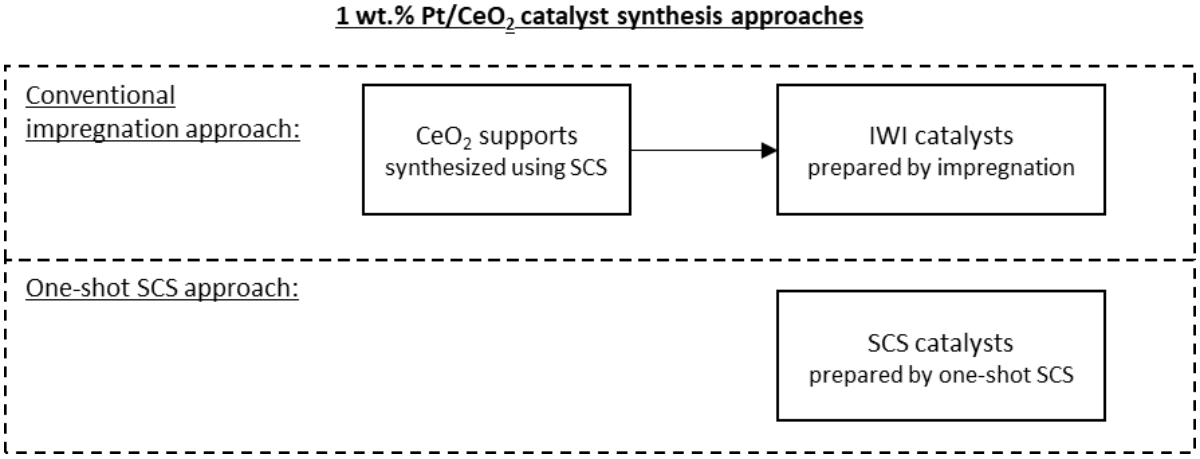

Figure 4.1:Different approaches for the synthesis of 1 wt.% Pt/CeO_2 catalysts

For the synthesis of the sets of CeO_2 supports and the SCS catalysts, the Ce-precursor type and fuel-oxidant ratio (φ = 0.5, 1, 1.25) of the combustion systems were varied within this study. This created subsets within the sets of CeO_2 supports, IWI catalysts and SCS catalysts.

Two glycine (denoted as GLC) combustion systems with the different Ce-precursor types were used for the synthesis of the sets of CeO_2 supports and the SCS catalysts. The two oxidants were cerium (III) nitrate hexahydrate (denoted as CN) and cerium (IV) ammonium nitrate (denoted as CAN). These glycine combustion systems using the two Ce-precursors were denoted as "CN+GLC" and "CAN+GLC" respectively.

Appendix A: Summary of the Synthesis Redox Reactions provides details regarding the formulation of the overall SCS reaction equations for the CN+GLC and CAN+GLC combustion systems used for the synthesis of the sets of CeO_2 supports and the SCS catalysts. The use of these two combustion systems results in the formation of two subsets of supports and catalysts within the collective sets of the CeO_2 supports and the SCS catalysts. Consequently, as the set of the CeO_2 supports were used in the synthesis of the IWI catalysts, this also leads to two subsets of catalysts within the collective set of the IWI catalysts. Furthermore, within each of the subsets of supports and catalysts, the fuel-oxidant ratio used in each of the CN+GLC and CAN+GLC combustion systems was also varied (φ = 0.5, 1, 1.25). This resulted in three different synthesis conditions for the synthesis of the supports and catalysts within each of the subsets. Overall, there are six different supports and catalysts within each of the collective sets of "CeO_2" supports and the "IWI" and "SCS" catalysts. Figure 4.2 provides a more detailed structure of the different sets and subsets of the ceria supports and 1 wt.% Pt/CeO_2 catalysts synthesized in this study.

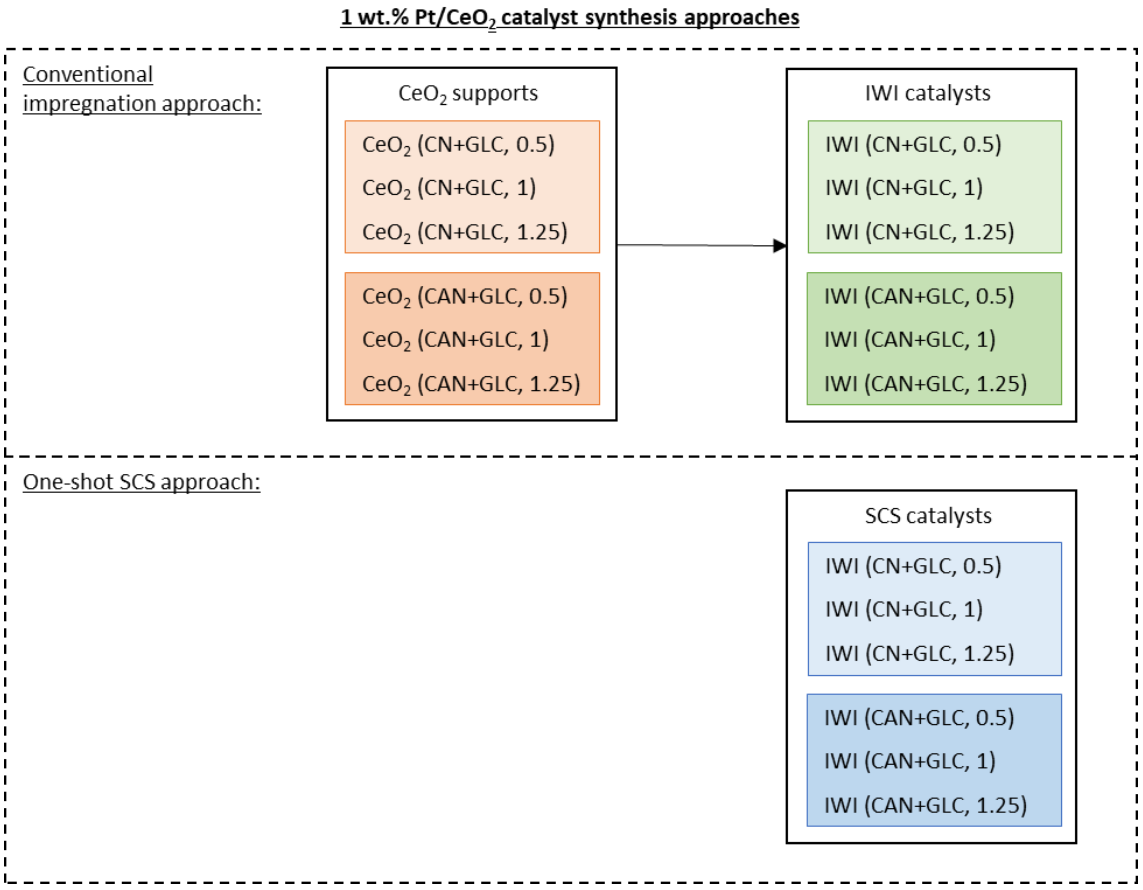

Figure 4.2 Schematic of the supports and catalysts synthesized within this study; solid black lines denote sets, coloured boxes denote subsets.

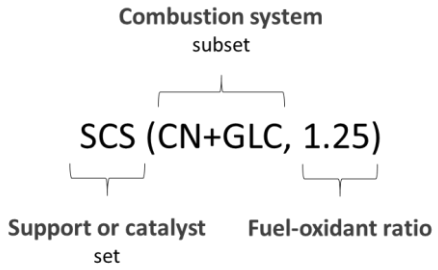

Figure 4.3 Naming system of the sets of CeO_2 supports, IWI catalysts and SCS catalysts.

The naming system used within this study is depicted in Figure 4.3 above. The first part of the name refers to the specific set of either "CeO_2" supports or to sets of the "IWI" and "SCS" catalysts. The combustion system and the fuel-oxidant ratio used are denoted within the brackets. For example, "SCS (CN+GLC, 1.25)" would refer to the individual catalyst sample synthesized using the one-shot CN+GLC combustion system and a fuel-oxidant ratio of 1.25.

In addition to the set of CeO_2 supports synthesized as detailed previously, a series of CeO_2 (CN+GLC) supports were synthesized with a fixed fuel-oxidant ratio of 0.25 and in which the furnace temperature was varied (400 °C, 500 °C, 600 °C, 700 °C). This was for the sole purpose of optimizing the temperature of the furnace. Results indicated that the furnace temperature had no effect on the properties of the CeO_2 supports (see section 5.3.2). A furnace temperature of 400 °C was used in the synthesis of the above mentioned CeO_2 supports and SCS catalysts.

4.1.1. Incipient Wetness Impregnation

Tetra-ammine platinum (II) nitrate (0.040 g) was dissolved in approximately 3 ml deionized H_2O. The CeO_2 support (2 g) was spread evenly in a 250 cm^3 ceramic crucible and placed on a hot plate set at 120 °C. The aqueous tetra-ammine platinum (II) nitrate, $Pt(NH_4)_4(NO_3)_2$, solution was dripped evenly over the CeO_2 to wet the entire surface. The wet powder was then stirred using a glass rod. This was repeated until all the aqueous solution has been used. The resulting catalyst is subsequently calcined at 350 °C in static air for 3 hours.

4.1.2. Solution Combustion Synthesis Method

The SCS synthesis approached followed a two-step process: pre-dehydration of the aqueous redox reaction mixture and combustion of the aqueous mixture, see Figure 4.4.

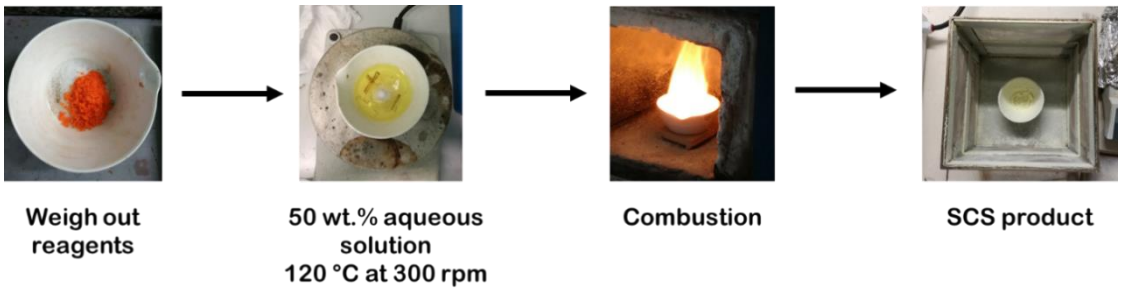

Figure 4.4:Solution Combustion Synthesis process

The precursors were weighed out separately to synthesize 2 g samples according to desired amount required for each specific combustion system and fuel-oxidant ratio. The precursors were weighed out

from least to most hygroscopic: glycine → ammonium cerium (IV) nitrate → cerium (III) nitrate hexahydrate → tetra-ammine platinum (II) nitrate. The solid precursors were then dissolved in deionized H_2O to make up a 50 wt.% solution. This solution was placed in a 250 cm^3 ceramic crucible on a hot plate at 120 °C. The solution was stirred at 300 rpm until a viscous gel-like solution formed due to the partial evaporation of the water. The hot ceramic crucible was then transferred to a stainless-steel mesh cage (see Appendix B: Stainless-steel Mesh Cage Design for the cage design details) which was transferred into the pre-heated (400 °C) Labofurn 1.4 L furnace from Kiln Contracts (Pty) Ltd. Initially, the solution boiled and frothed as it underwent dehydration. At the point of complete dehydration, the mixture self-ignited and a large volume of gases were released. The combustion reaction resulted in the formation of a very fine, voluminous powder. The stainless-steel mesh cage was then removed from the furnace and allowed to cool down, and then the powder product was retrieved.

4.2. Catalyst Characterization

The following section details the characterization techniques used in this study.

4.2.1. Thermogravimetric Measurements

Simultaneous Thermogravimetric and Differential Thermogravimetric Analysis (TGA-DTG), and Differential Thermal Analysis (DTA) was performed on the SCS precursors (CN, CAN and GLC) and the sets of CeO_2 supports, IWI and SCS catalysts using the TA Instruments Discovery Series SDT650 instrument controlled by the TA Instruments Trios v4.2.1.36612 software. These thermogravimetric measurements were used to determine the mechanisms of the thermal decomposition of the SCS precursors and the amount of residuals left on the combustion synthesized powders (the sets of CeO_2 supports and SCS catalysts). The analysis was carried out in a 90 μL alumina crucible using approximately 20 mg of sample under a N_2 atmosphere (flow of 50 ml/min) from 50 – 600 °C at a heating rate of 10 °C/min. The sample was first allowed to equilibrate at 50 °C before proceeding with the linear heating program. The TA Instruments Trios software was used to analyse the DTG curves and the percentage weight losses.

4.2.2. X-Ray Diffraction (XRD)

X-Ray Diffraction (XRD) was used to characterize the crystallinity, atomic structure and phase of the CeO_2 supports, and the SCS and IWI catalysts. Powder diffractograms of the powders were recorded using a Bruker D8 Advance laboratory X-Ray diffractometer equipped with a cobalt source ($\lambda_{K\alpha1}$ = 0.178897 nm, slit width = 1.0 mm) and a position sensitive detector (LYNXEYE XE, Bruker AXS) at 20 kV and 5 mA. The diffraction patterns were recorded over a scan range of 20 - 120° at a rate of 1.50°/min. The reference pattern from the International Centre for Diffraction Data (2008) (ICDD) database were used to assign the cubic fluorite CeO_2 phase present in the sets of CeO_2 supports, SCS catalysts and IWI catalysts using the Diffrac.Eva software. Additionally, the mean crystallite sizes were determined from the X-Ray line broadening of the reflection peak using the Scherrer equation (Scherrer, 1912):

$$d = \frac{K\lambda}{\beta cos\theta} \qquad \text{Equation 4.1}$$

where d is the crystallite size, λ is the radiation wavelength, θ is the maximum diffraction peak angle, and β is the full width at half maxima (FWHM) of the peak. The crystallite sizes of the ceria supports for the sets of CeO_2 supports, SCS catalysts and IWI catalysts were calculated using the line broadening of the most intense reflection of the CeO_2 crystallographic structure, the (111) peak, and a shape factor (K) of 0.9 (Ertl *et al.*, 2008).

4.2.3. BET Surface Area

A Micromeritics TriStar II 3020 Surface Area and Porosity Analyzer was used to conduct standard N_2-physisorption to determine the Brunauer-Emmett-Teller (BET) surface areas of the CeO_2 supports, and the SCS and IWI catalysts. N_2-physisorption was chosen to determine the textural properties CeO_2 and 1 wt.% Pt/CeO_2 powders based on the IUPAC recommendation of using this technique for porous materials with a specific surface area larger than 5 m^2/g (Sing, 1982). It was expected that these powders would have specific surface areas larger than 10 m^2/g based on the results obtained by

Purohit *et al.* (2001), Morfin *et al.* (2016) and Kang, Ozgur and Varma (2018) who found specific surface areas between 10 and 40 m^2/g.

Approximately 100 mg of powder was loaded in the sample tube and degassed under vacuum at 120 °C overnight in a VacPrep 061 instrument to remove any physisorbed moisture. The N_2 adsorption-desorption isotherms were measured at – 196 °C. The N_2 adsorption isotherms were used to fit the BET equation using the Micromeritics TriStar II 3020 software (Micromeritics Instrument Corporation, 2007). The fitting strategy applied - the number of accepted data points within the relative pressure (p/p_0) range and the p/p_0 range used– was important as it strongly influenced the BET surface area obtained. The N_2 isotherms were fitted to the linearized BET equation (Brunauer *et al.*, 1938):

$$\frac{1}{v_{STP} \cdot \left(\frac{p_0}{p} - 1\right)} = \frac{1}{v_m c} + \frac{c-1}{v_m c} \cdot \frac{p}{p_0} \qquad \text{Equation 4.2}$$

where $slope = S = \frac{c-1}{v_m c}$ and the $y - intercept = YI = \frac{1}{v_m c}$

where v_{STP} is the volume of N_2 adsorbed at standard temperature and pressure (STP), p is the N_2 partial vapour pressure, p_0 is the N_2 saturated pressure, v_m is the volume of N_2 adsorbed to produce a monolayer coverage on the surface of the sample and c is the dimensionless BET constant which is related to the of N_2 adsorption enthalpy. The left-hand side of Equation 4.2 was plotted versus the relative pressure for a p/p_0 range of 0.01 – 0.17. The linear plots were only considered acceptable if the correlation coefficient was close to 1 and the value of the fitted BET constant "c" was between 50 and 300 (Webb and Orr, 1997). The number of points included in the linear fitting was varied until both constraints were met (see Appendix C.2.2. Linearized BET fitted isotherms for the linearized BET fitted isotherms). Linear regression analysis of the accepted linear BET points was then used to determine slope (S) and the y-intercept (YI), and from this the monolayer coverage of N_2 (cm^3/g) was determined. The BET surface area (cm^3/g) was then calculated from the monolayer coverage of N_2 using the following equation (Brunauer *et al.*, 1938):

$$S_{BET} = \frac{\rho_{STP}^{vap} \cdot N_A \cdot A_{CS}}{M_{N_2}(S + YI)} = \frac{\rho_{STP}^{vap} \cdot N_A \cdot A_{CS}}{M_{N_2}\left(\frac{1}{v_m}\right)} = \frac{v_m \cdot \rho_{STP}^{vap} \cdot N_A \cdot A_{CS}}{M_{N_2}} \qquad \text{Equation 4.3}$$

where ρ_{STP}^{vap} is the density of N_2 vapour at STP (1.25 g/dm^3), N_A is Avogadro's constant, A_{CS} is the mean cross-sectional area occupied by a single N_2 molecule (0.162 nm^2), and M_{N_2} is the molar mass of N_2 (28.014 g/mol).

4.2.4. Inductively Coupled Plasma – Atomic Emission Spectroscopy (ICP-AES)

The platinum loadings of the as-prepared set of SCS catalysts and the calcined set of IWI catalysts was determined using Inductively Coupled Plasma – Atomic Emission Spectrometry (ICP-AES). 100 mg of catalyst sample was pre-digested for 1 hour in a solution of 5.25 ml hydrochloric acid (HCl) and 1.75 ml nitric acid (HNO_3). The solution was then transferred into a MARS-5 microwave digester at 180 °C and 800 psi (ramped up over 25 min) for 10 min. The digested sample was then diluted and injected into the Thermo ICAP 6200 instrument to determine the platinum loadings of the catalysts.

4.2.5. Transmission Electron Microscopy

Transmission Electron Microscopy (TEM) was used to obtain highly magnified images of the SCS and IWI catalysts. Both bright field and dark field images were collected (Appendix C.3.1.1. Background theory of TEM provides details regarding the theoretical background of TEM and the different techniques of collecting bright field and dark field images). Dark field images provide a better structural resolution in comparison with bright field images. This is because darkfield images are formed from the collection of non-Bragg scattered electrons. These electrons have passed close to the atomic nuclei and are elastically scattered. The image formed from these elastically scattered electrons provides good resolution between materials with similar densities, which is required in this study due to the similarity in the atomic masses of Pt (195.084 u) and Ce (140.116 u).

The JOEL JEM-ARM200F double Cs-corrected TEM instrument at the Centre for High Resolution Transmission Electron Microscopy at the Nelson Mandela University was used to collect both BF and high-angle annular darkfield (HAADF) TEM images. The instrument was equipped with a scanning transmission electron microscopy (STEM) unit and an HAADF detector, operated at 200 kV. Quantifoil carbon film supported on copper TEM grids were used to study the powder samples. The powder samples were suspended in a solution of 90 vol.% ethanol and added dropwise onto the grids. Once all the ethanol had evaporated off, the samples were ready for viewing. The BF and HAADF images were used to determine the particle size distribution and dispersion of Pt on the CeO_2 supports of the sets of IWI and SCS catalysts. The sizes of the Pt particles were measured using the open-source ImageJ software package (Rasband, 2016). The same analysis on the BF and HAADF images of the IWI catalysts was carried out by Karen Ssekimpi (2018).

4.2.6. X-Ray Photoelectron Spectroscopy (XPS)

X-Ray Photoelectron Spectroscopy (XPS) was used to determine oxidation states of the Pt species on the surface of the as-prepared set of SCS catalysts. Appendix C.4.1. Theoretical Background of XPS provides details regarding the theoretical background of XPS, spectral features of XPS spectra such as background signal and multiplet splitting, and experimental charge compensation and post-measurement charge correction techniques.

Approximately 10 mg of powder sample was loaded onto 1 x 1 cm carbon tape square. XPS measurements were carried out using a SPECS PHOIBOS 150 spectrometer with a monochromatic Al Kα X-ray source (hν = 1486.71 eV) at the University of Johannesburg. A low energy flood gun was used to counteract the effects of charging (3.5 eV, 20 μA). Survey spectra were collected to determine the elemental species present on the surface of the samples over a binding energy (BE) range of 1356 – 0 eV with an overall energy resolution (photon and analyzer) of 0.8 eV. High-resolution spectra of the C 1s and Pt 4f peaks were recorded with an energy step size of 0.05 eV and an overall energy resolution (photon and analyzer) of 0.8 eV.

The spectral analysis – background spectral subtractions and peak fittings – was carried out using IGOR Pro 6.37 software with the XPST extension package. Firstly, the spectral background intensity was fitted and removed prior to photoelectron peak fitting (see Appendix C.4.1. Theoretical Background of XPS for the different types of background subtraction models). In this study, due to the narrow BE energy range of the high-resolution C 1s and Pt 4f spectra, a Shirley type background subtraction was used. Next, the photoelectron peaks of the C 1s and Pt 4f orbitals were fitted using a mixed Gaussian-Lorentzian line shape. The Gaussian-Lorentzian (GL) ratio is denotated as GL (X %) with a X % contribution with respect to the Gaussian line shape. The Full Width Half Maximum (FWHM) of the

peaks was constrained between 1 eV and 2.5 eV. The asymmetry was kept at 0.001. The peak position (BE), GL ratio (5 – 95 %), and FHWM (1 – 2.5 eV) of each fitted photoelectron peak were adjusted to minimize the chi-squared (χ^2) value to less than 10^{-6} to obtain the best fit. See Table 8.3 and Table 8.4 in Appendix C.4.3. Fitted Peak Parameters for the fitted peak parameters of the C 1s and Pt 4f photoelectron peaks.

The C 1s peaks were fitted using four singlets which represent the different carbon bonds: hydrocarbon (C–C, C–H), alcohol/ether (–COH, –COC–), carbonyl (–C=O) and ester (–OC=O) bonds (Gardner *et al.*, 1995; Estrade-Szwarckopf, 2004). The BEs of the singlets assigned to the alcohol/ether (–COH, –COC–), carbonyl (–C=O) and ester (–OC=O) functionalities were constrained to a shift of +1.2 – 1.6 eV, +2.7 – 3.1 eV and +3.5 – 4.1 eV respectively towards higher BEs with reference to the peak assigned to the hydrocarbon (C–C, C–H) functionality. The singlet assigned to the hydrocarbon (C–C, C–H) functionality was unconstrained in terms of BE. The Pt 4f high-resolution spectra was shifted with respect to the C 1s singlet assigned to the hydrocarbon (C–C, C–H) functionality to correct for the charging effects (Metson, 1999). The $4f_{5/2}$ and $4f_{7/2}$ peaks were fitted using a doublet representing the multiplet splitting of the 4f orbital using a mixed Gaussian-Lorentzian line shape. The peak energy separation and peak area ratio of the doublets were constrained to 3.33 eV and 4:3 respectively (Wagner *et al.*, 1979). The peak position of the doublet assigned to the Pt^0 state was constrained to the reference value of 71.2 $\pm$ 0.5 eV (Wagner *et al.*, 1979). The peak positions of the doublets assigned to the Pt^{2+} and Pt^{4+} oxidation states were constrained to a shift of +1.0 – 3.0 eV and +3.6 – 4.5 eV towards higher BEs with reference to the $4f_{5/2}$ Pt^0 doublet peak based on peak shifting observed in literature (Bera *et al.*, 2000; Bera *et al.*, 2003a; Bera *et al.*, 2003b; Hatanaka *et al.*, 2009).

4.3. Catalyst Performance Evaluation

The SCS and IWI catalysts were evaluated and compared in terms of their catalytic activity towards the Water-Gas Shift (WGS) reaction. A high throughput Flowrence reactor developed by Avantium Technologies was used to conduct the catalytic performance evaluation tests. The Flowrence's reactor setup contains sixteen parallel fix bed reactors. In the effluent section, there is a multi-position valve which allows for alternating online Gas Chromatograph (GC) analysis of the effluent streams from each reactor using a CP-490 Micro-GC from Agilent with the compounds separated over a 20 m MS5 column or a 1 m COX column and detected by a thermal conductivity detector (TCD). Details regarding the full setup and operation of the Flowrence and GC sampling and analysis can be found in the studies done by Luchters *et al.* (2017) and Brown (2017).

Two catalysts from each of the sets of IWI and SCS catalysts were evaluated. The catalysts were chosen such that the same combustion systems (CN+GLC and CAN+GLC) and fuel-oxidant ratios (φ = 1) were used in the synthesis of the SCS catalysts and the CeO_2 supports for the IWI catalysts. The catalysts used in the WGS activity measurements were IWI (CN+GLC, 1), IWI (CAN+GLC, 1), SCS (CN+GLC, 1) and SCS (CAN+GLC, 1). The catalysts (23 mg) were loaded in triplicate within the isothermal zones of the quartz reactor tubes (see Appendix D.1. Catalyst Loading Procedure for more details regarding the reactor loading procedure). Two reactors (no. 2 and 9) were loaded as blanks (filled with only SiC), to allow for GC sampling of the WGS feed. The placements of the reactor tubes within the Flowrence's reactor setup were randomly selected (see Appendix D.1. Catalyst Loading Procedure for more details regarding the placement of the catalysts).

Table 4.1 tabulates the WGS feed composition which simulates the typical effluent stream from the reformer stage in a fuel processor.

Table 4.1: Feed composition for the WGS reaction and the volumetric flow rates for each reactor

Component	**Composition (vol%)**	**Feed Rate (ml/min)**
H_2	50	25
CO	6.67	3.3
CO_2	6.67	3.3
H_2O (g)	33.3	1.7
He	3.36	17
Total	100	50

Table 4.2 tabulates the operating conditions used for the catalyst performance evaluation tests. The catalysts' activity towards the WGS reaction was determined at four different temperatures (300 °C, 310 °C, 320 °C and 330 °C), see Appendix D.2. WGS Temperature Programme for details regarding the temperature programme of the WGS test.

Table 4.2: Operating conditions

Parameter	**Value**
Temperature	300 °C, 310 °C, 320 °C, 330 °C
Pressure	1 bar_g
$SGHSV_{wet}$	200 000 hr^{-1}

The wet gas hourly space velocity (wet GHSV) was determined based on the catalyst loading using the following formula:

$$SGHSV_{wet} = \frac{\dot{V}_{feed}}{V_{catalyst}} \qquad \text{Equation 4.4}$$

where GHSV is the wet gas hourly space velocity ($hours^{-1}$), $\dot{V}_{feed}$ is the volumetric flow rate of the WGS feed per reactor (cm^3/hour) and $V_{catalyst}$ is the volume of the catalyst (cm^3).

The work up of the GC sampling results of the reactors was performed using Microsoft Access software. The carbon monoxide (CO) conversions were calculated using the following equation:

$$X_{CO}(\%) = \frac{F_{CO,in} - F_{CO,out}}{F_{CO,in}} \times 100 \qquad \text{Equation 4.5}$$

where $X_{CO}(\%)$ is the percentage conversion of CO, $F_{CO,in}$ is the molar flow rate of CO to each reactor (mol/min) and $F_{CO,out}$ is the molar flow rate of CO out of each reactor.

5. Results

For this study, a series of CeO_2 supports and one-shot 1 wt.% Pt/CeO_2 catalysts (SCS catalysts) were synthesized using solution combustion synthesis (SCS). A glycine (GLC) fuel system was used with two Ce-precursor types (cerium (III) nitrate hexahydrate (CN) and ammonium cerium (IV) nitrate (CAN)), varying fuel-oxidant ratios (φ = 0.5, 1, 1.25) and furnace temperatures (400 °C, 500 °C, 600 °C and 700 °C). Incipient wetness impregnation (IWI) using tetra amine platinum (II) nitrate, $Pt(NH_4)_4(NO_3)_2$, was used to synthesize 1 wt.% Pt/CeO_2 catalysts (IWI catalysts) from the synthesized CeO_2 supports. This section details the physical characteristics of the synthesized CeO_2 supports, the sets of IWI and SCS catalysts, namely their crystallite sizes, surface areas, Pt loadings, Pt particle sizes and Pt oxidation state variances. Table 8.5 in Appendix C.5. Summary of Characterizations summarizes all the characterization data for these supports and catalysts.

5.1. Reproducibility

An investigation was conducted into the reproducibility of the properties of the powders synthesized using SCS in terms of the powder's XRD crystallite sizes, BET surface areas, ICP-AES for Pt loadings, and thermogravimetric measurements for determining the amount of unreacted reagents present after combustion. For more details regarding these characterization method, see sections 5.3 and 5.4 below.

Four duplicates of CeO_2 supports were synthesized with stoichiometric CN+GLC and CAN+GLC combustion systems using a furnace temperature of 400 °C. Small deviations in the crystallite sizes (26 ± 2 nm and 50 ± 1 nm) and BET surface areas (25 ± 2 m^2/g and 10 ± 2 m^2/g) of CeO_2 supports were observed for CN+GLC and CAN+GLC SCS system, respectively. The average amounts of unreacted reagents for the CN+GLC and CAN+GLC combustion systems were 1.08 ± 0.19 % and 0.78 ± 0.25 %, respectively. The Pt loadings of the SCS catalysts synthesized using both Ce-precursor types corresponded well with the target value of 1 wt.% (CAN: 0.96 ± 0.03 wt.%; CN: 0.96 ± 0.02 wt.%). The one-shot SCS method applied in this study for preparing the various powder materials (CeO_2 supports and 1 wt.% Pt/CeO_2 catalysts) can be considered reproducible.

5.2. Thermogravimetric Measurements

Temperature-programmed decomposition of the SCS reagents (CN, CAN and GLC) was conducted to determine the mechanisms of their thermal decompositions.

5.2.1. Cerium (III) Nitrate Hexahydrate

The TGA-DTG-DTA curves of the mass loss of CN are shown in Figure 5.1. These curves followed a similar trend to those found by Strydom and Vuuren (1987), Papastergiades *et al.* (2009), Ayodele *et al.* (2016), and Kang, Ozgur and Varma (2018). In his pioneering work on lanthanide nitrate decompositions, Wendlandt (1956) found that cerium and samarium nitrate hydrates were the only light lanthanide (III) nitrate hydrates that did not decompose via oxonitrate intermediates. The thermogravimetric measurements of this study indicated that CN underwent two major endothermic decomposition processes. The first major decomposition process involved the loss of the crystal water of hydration over a temperature range 50 – 220 °C in several steps. The anhydrous cerium nitrate ($Ce(NO_3)_3$) decomposed directly into CeO_2 from a temperature of 245 °C with complete decomposition occurring at 450 °C. The thermal decomposition of CN followed the following sequence:

$$Ce(NO_3)_3.6H_2O \xrightarrow[50-245\,^{\circ}C]{-6H_2O} Ce(NO_3)_3 \xrightarrow[245-450\,^{\circ}C]{-NO_x} CeO_2$$ Equation 5.1

The overall measured weight loss between 50 – 600 °C was 59.9 %. The experimental weight losses over the dehydration and anhydrous cerium nitrate decomposition stages were 25.3 % and 34.6 %, which are close to the expected theoretical values of 24.9 % and 35.5 % (see Table 5.1) and correspond well with the results found by the previously mentioned studies. This indicates that the assumptions regarding the composition change over each temperature range is correct as the theoretical mass loss and the experimental mass loss correlated well with each other (within 1.2 %).

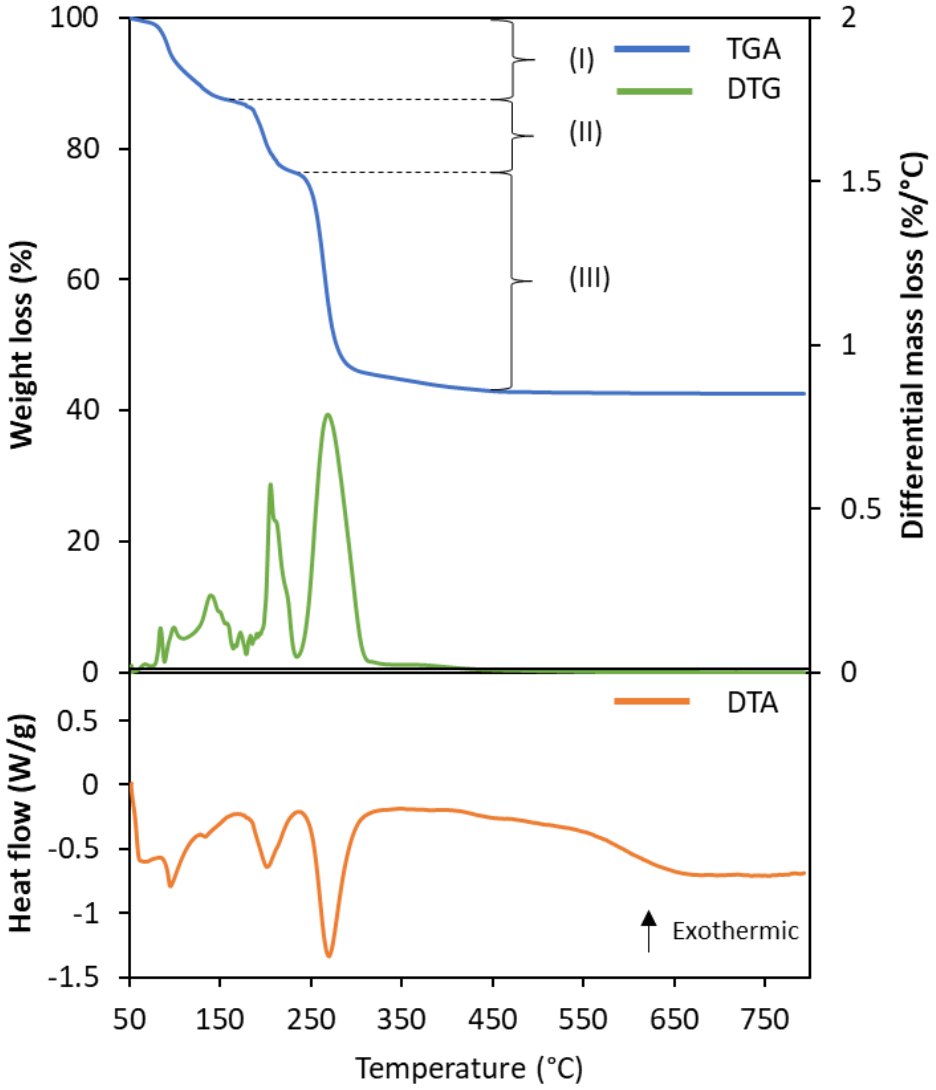

Figure 5.1: TGA-DTG-DTA curves of cerium (III) nitrate hexahydrate in N_2 (100 Sml/min) at 10 °C/min heating rate. For the theoretically calculated composition changes at the indicated points see Table 5.1.

Table 5.1: Evaluation of the TGA curves of cerium (III) nitrate hexahydrate (see Figure 5.1).

Change	Temperature range (°C)	Observed Mass Change (%)	Proposed composition change	Theoretical Mass Change (%)
Initial	50	-	$Ce(NO_3)_3.6H_2O$	-
(I)	50 – 160	11.6	$Ce(NO_3)_3.6H_2O \xrightarrow{-3H_2O} Ce(NO_3)_3.3H_2O$	12.4
(II)	160 – 245	13.6	$Ce(NO_3)_3.3H_2O \xrightarrow{-3H_2O} Ce(NO_3)_3$	12.4
(III)	245 – 450	34.6	$Ce(NO_3)_3 \xrightarrow{-NO_x} CeO_2$	35.5

5.2.2. Cerium (IV) Ammonium Nitrate

The TGA-DTA and DTA curves of CAN showed a three-step endothermic decomposition process with a weak inflexion point of the TGA curve at ~240 °C (see Figure 5.2). Similar to Wendlandt's (1956) findings for CN, ammonium cerium (IV) nitrate (CAN) also did not undergo thermal decomposition via oxonitrate intermediates (Březina and Rosický, 1963; Pokol *et al.*, 1994; Bondioli *et al.*, 1999; Shih and Huang, 2013). Pokol, Leskelä and Niinistö (1994) observed a two-step thermal decomposition process with a weak inflexion point at ~250 °C under similar conditions. They used *ex situ* measurements to confirm the presence of paramagnetic cerium (III) as an intermediate at 210 °C. Hence, Pokol, Leskelä and Niinistö (1994) proposed that CAN directly decomposed to $Ce(NO_3)_3$ over a temperature range of 170 – 255 °C and was quickly followed by the thermal decomposition to CeO_2 with complete decomposition occurring at 290 °C. The thermal decomposition of CAN thus followed the following sequence:

$$(NH_4)_2Ce(NO_3)_6 \xrightarrow[50-255\,℃]{-NH_3,\ NO_x} Ce(NO_3)_3 \xrightarrow[255-290\,℃]{-NO_x} CeO_2 \qquad \text{Equation 5.2}$$

In contrast to results found by Pokol, Leskelä and Niinistö (1994), Bondioli *et al.* (1999) proposed that CAN decomposed to form $Ce(NO_3)_4$ as an intermediate as the experimental mass-loss values observed by Bondioli *et al.* (1999)corresponded more closely with a $Ce(NO_3)_4$ intermediate product opposed to $Ce(NO_3)_3$. Using the postulation by Pokol, Leskelä and Niinistö (1994), the theoretically calculated weight losses of the two decomposition stages (40.5 % and 28.1 %) were in close agreement with the experimental weight losses (41.2 % and 27.1 %), see Table 5.2. The theoretical weight losses of the two decomposition stages calculated using the postulation of $Ce(NO_3)_4$ as the intermediate product as proposed by Bondioli *et al.* (1999) did not correlate well with the experimental weight losses. The theoretically calculated weight loss of the first decomposition stage was much smaller than the experimentally observed weight loss (29.2 % compared to 41.2 %). This indicates that the assumption regarding the postulation of $Ce(NO_3)_3$ as the intermediate product is correct as the theoretical mass loss and the experimental mass loss correlated well with each other (within 1.0 %).

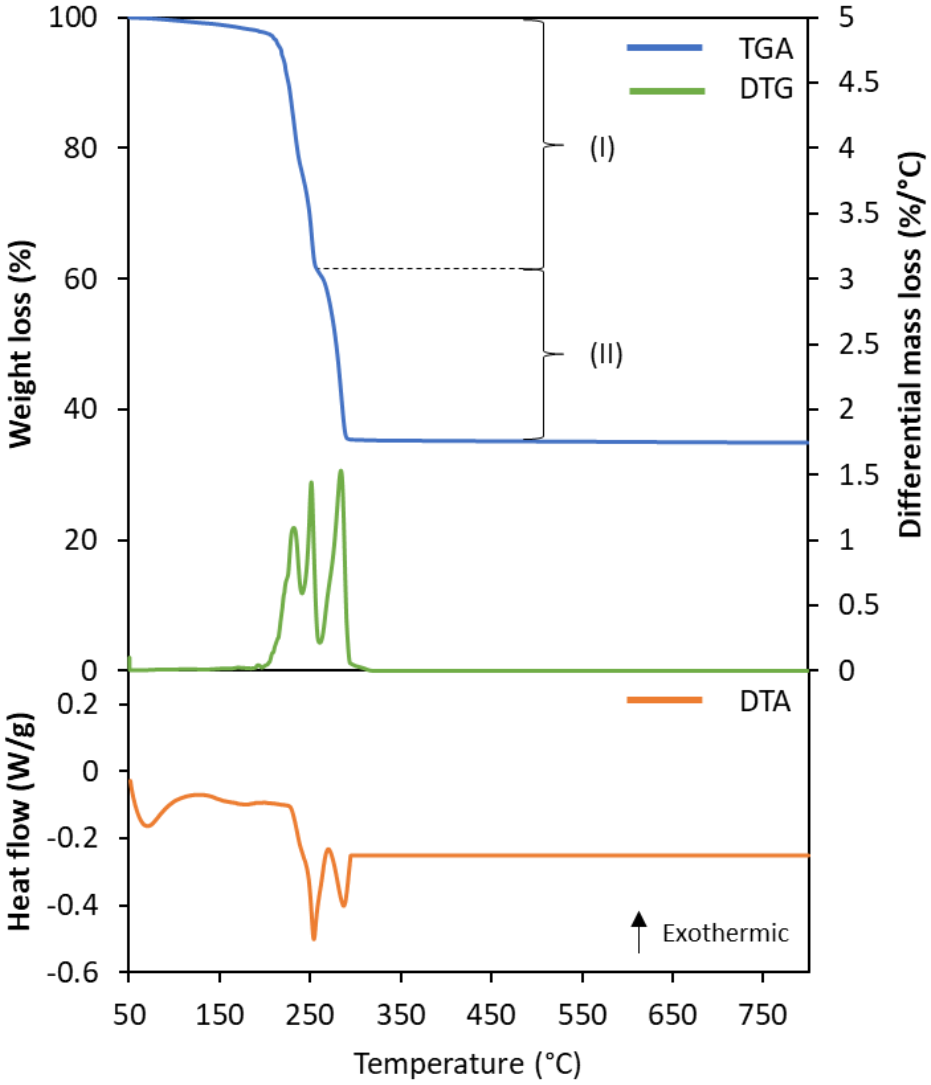

Figure 5.2: TGA-DTG-DTA curves of cerium (IV) ammonium nitrate in N_2 (100 Sml/min) at 10 °C/min heating rate. For the theoretically calculated compositions at the indicated points, see Table 5.2.

Table 5.2: Evaluation of the TGA curves of cerium (IV) ammonium nitrate using the postulation posed by Pokol, Leskelä and Niinistö (1994) (see Figure 5.2).

Change	Temperature range (°C)	Observed Mass Change (%)	Proposed composition change	Theoretical Mass Change (%)
Initial	50	-	$(NH_4)_2Ce(NO_3)_6$	-
(I)	50 – 255	41.2	$(NH_4)_2Ce(NO_3)_6 \xrightarrow{-NH_3,\ NO_x} Ce(NO_3)_3$	40.5
(III)	255 – 290	27.1	$Ce(NO_3)_3 \xrightarrow{-NO_x} CeO_2$	28.1

5.2.3. Glycine

The TGA-DTG-DTA curves of glycine showed three weight loss stages (see Figure 5.3). The thermal decomposition of glycine was characterized by two sharp weight losses of 2.91 wt.% in the 220 – 230 °C temperature range and 49.5 wt.% between 238 and 310 °C. This was followed by a gradual weight loss stage from 310 – 600 °C. The overall weight loss measured over 50 – 600 °C was 78.6 wt.%. Complete decomposition was not achieved at 600 °C in agreement with the results from Kumar, Wolf and Mukasyan (2011) who observed complete decomposition at 627 °C. The temperature ranges and shapes of the TGA-DTG-DTA curves of glycine correspond well with those found in literature (Li *et al.*, 2007; Kumar, Wolf and Mukasyan, 2011; Kang, Ozgur and Varma, 2018).

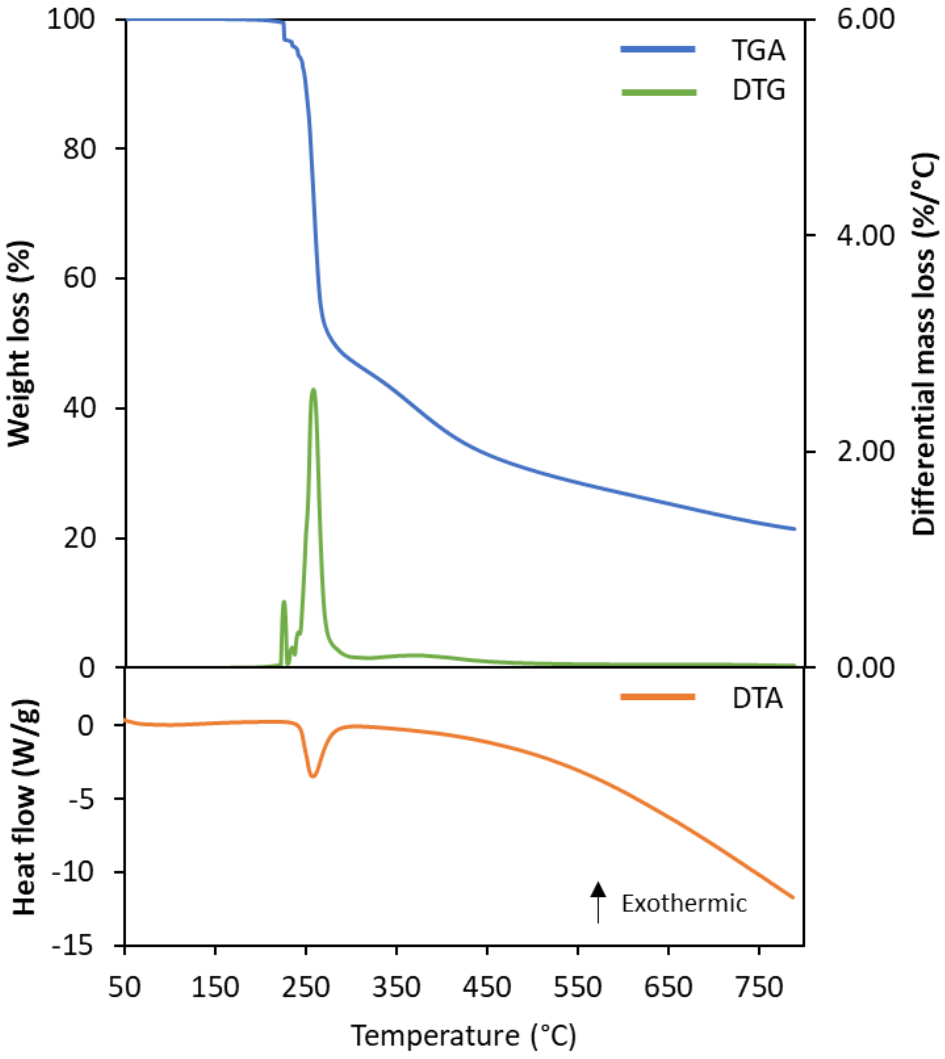

Figure 5.3: TGA-DTG-DTA curves of glycine in N_2 (100 Sml/min) at 10 °C/min heating rate.

5.3. Characterization of the CeO_2 supports

This section details the physical characteristics of the set of CeO_2 supports synthesized by SCS for the conventional two-step impregnation approach prior to impregnation. This represents the first set of samples as detailed in section 4.1.

5.3.1. Thermogravimetric measurements

Thermogravimetric measurements of the set of CeO_2 support powders were performed to determine the extent of combustion of the CN+GLC and CAN+GLC combustion systems used to synthesize these supports. The TGA-DTG-DTA curves of the CeO_2 (CN+GLC) and CeO_2 (CAN+GLC) support powders are shown in Figure 5.4 and Figure 5.8 respectively. Thermogravimetric measurements of the set of CeO_2 support powders exhibited a weight loss upon temperature-programmed treatment up to a maximum temperature of 600 °C. The overall weight loss of the CeO_2 (CN+GLC) and CeO_2 (CAN+GLC) support powders over the temperature range of 50 – 600 °C was in the range of 0.8 – 3.7 %, see Table 5.3.

The TGA curves of the CeO_2 (CN+GLC) and CeO_2 (CAN+GLC) support powders showed a weight loss of 1.3 ± 0.5 % over the temperature range of 50 – 200 °C. The corresponding broad DTGA peaks indicated the maximum weight loss transition occurred at ~100 °C. The DTA peaks indicated that it was an endothermic process that had occurred. This endothermic weight loss which occurred at ~100 °C was attributed to the removal of physisorbed water from the surface of the CeO_2 support powders.

The CeO_2 (CN+GLC) and CeO_2 (CAN+GLC) supports synthesized using the fuel-lean conditions (φ = 0.5) were the only support powders for which an additional weigh loss peak above 100 °C was observed. The second broad weight loss peak of ~ 2.5 % over the temperature range of 200 – 600 °C was observed for the CeO_2 (CN+GLC, 0.5) and CeO_2 (CAN+GLC, 0.5) support powders. The temperature range for these broad weight losses corresponded with the decomposition temperature ranges of the CN, CAN and GLC precursors which are predominantly in the range of 220 – 550 °C. This was an indication of incomplete combustion and thermal decomposition of the residual carbon and nitrate residues from the fuel and from the nitrate Ce-precursors respectively. The incomplete decomposition of the Ce-precursors could be expected as these were in excess under the fuel-lean combustion conditions.

Compared to the average weight loss that occurred within the combustion reaction (~ 72 %), the overall weight loss (0.8 – 3.7 %) of the CeO_2 (CN+GLC) and CeO_2 (CAN+GLC) support powders due to residual, partially unreacted SCS precursors is considered very small. Hence, it is considered that complete combustion of the SCS reaction occurred. For this reason, calcination of the set of CeO_2 supports prior to impregnation for the synthesis of the set of IWI catalysts was not carried out.

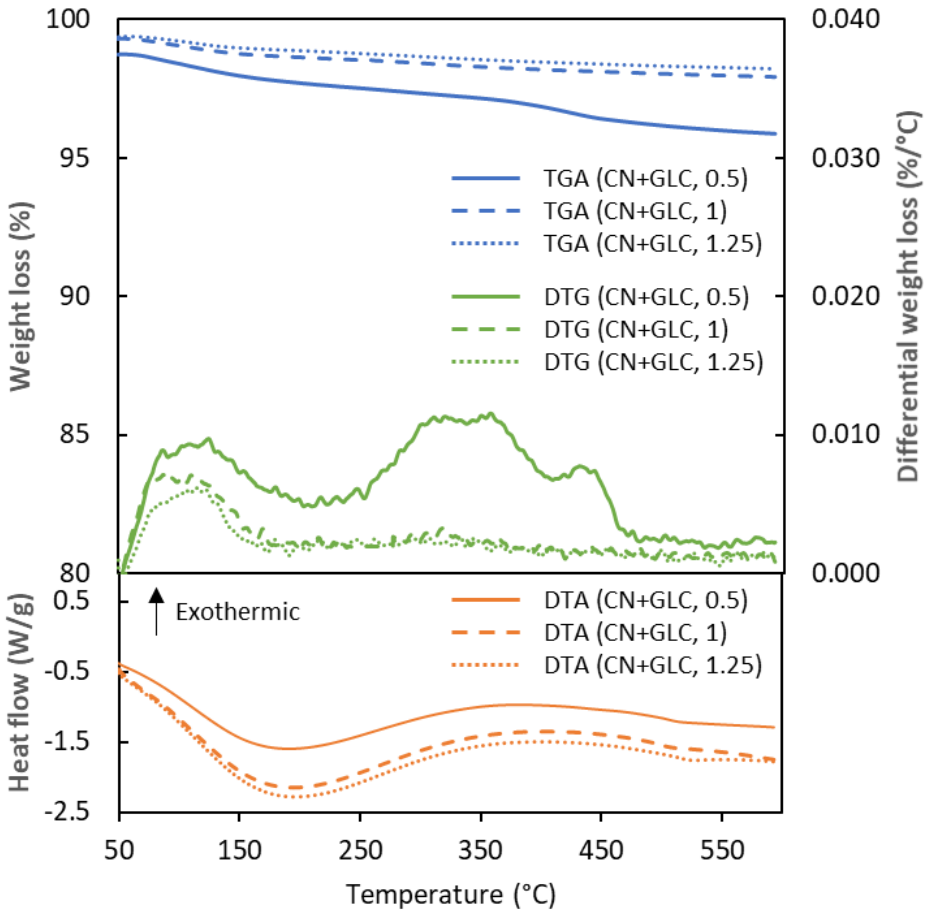

Figure 5.4: TGA-DTG-DTA curves of the CeO_2 (CN+GLC) supports synthesized using varying fuel-oxidant ratios.

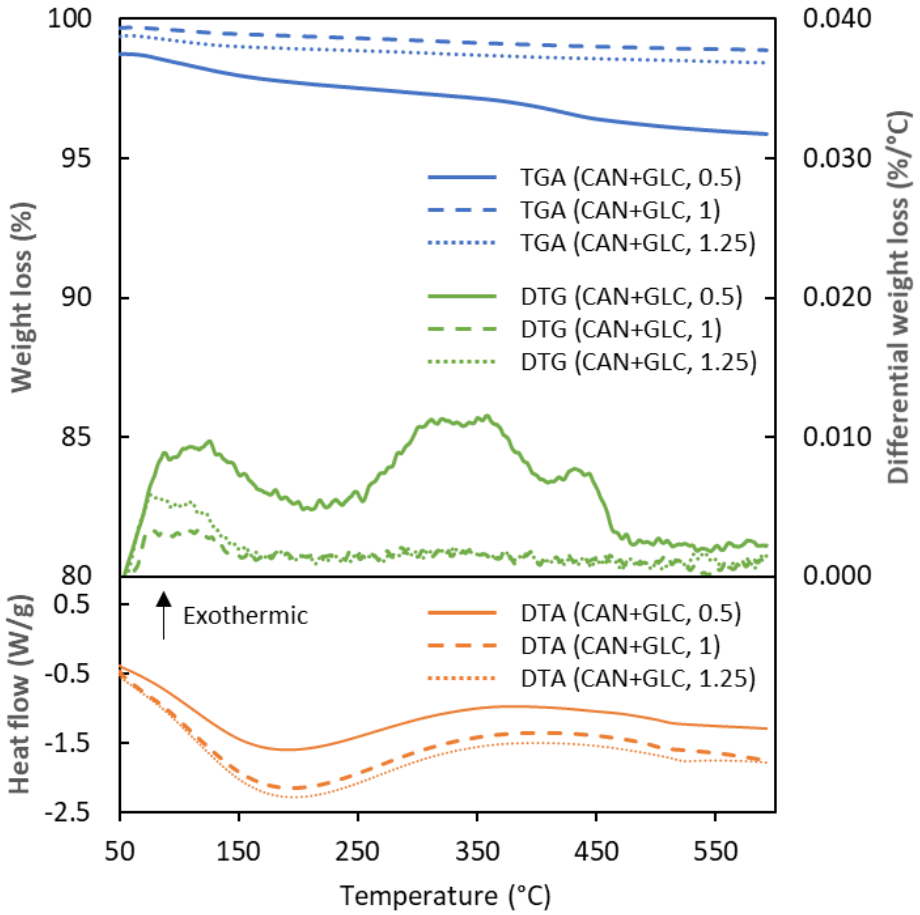

Figure 5.5: TGA-DTG-DTA curves of the CeO_2 (CAN+GLC) supports synthesized using varying fuel-oxidant ratios.

Table 5.3: Evaluation of the TGA curves of the set of CeO_2 supports (see Figure 5.4 and Figure 5.5).

CeO_2 Support	**Temperature range (°C)**	**Observed Mass Change (%)**
CeO_2 (CN+GLC, 0.5)	50 – 200	1.0
	200 – 600	2.7
CeO_2 (CN+GLC, 1)	50 – 600	1.4
CeO_2 (CN+GLC, 1.25)	50 – 600	1.2
CeO_2 (CAN+GLC, 0.5)	50 – 200	1.0
	200 – 600	2.4
CeO_2 (CAN+GLC, 1)	50 – 600	0.8
CeO_2 (CAN+GLC, 1.25)	50 – 600	1.0

5.3.2. X-Ray Diffraction

The XRD spectra of the CeO_2 supports synthesized using different furnace temperatures and the CN+GLC and CAN+GLC combustion systems with varying fuel-oxidation ratios are shown in Figure 8.2 and Figure 8.3 in Appendix C: Summary of the Characterizations.

All the CeO_2 supports were indexed to the cubic phase fluorite, space group structure (*Fm-3m*, JCPDS01-081-0792) corresponding to reflections of the (111), (200), (220), (311), and (222) planes (International Centre for Diffraction Data, 2008) using the Diffrac.Eva software. The Scherrer equation was used to calculate the CeO_2 crystallite sizes from the line broadening of the (111) reflection (Scherrer, 1912), see Figure 5.6 a) and b) for the crystallite sizes.

The diffractograms of the CeO_2 supports synthesized using the different furnace temperatures exhibited very similar diffraction intensities. The crystallite sizes of the CeO_2 supports synthesized using the different furnace temperatures were very similar with an average size of 7 ± 1 nm, see Figure 5.6 a). The furnace temperature therefore had no effect on the crystallinity and the crystallite sizes of the CeO_2 supports. As no advantageous effect was observed for the use of higher furnace temperatures, a lower temperature (400°C) was used in the consequent synthesis of the CeO_2 supports and SCS catalysts using the CN+GLC and CAN+GLC combustion systems with varying fuel-oxidation ratios.

For the CeO_2 (CN+GLC) and CeO_2 (CAN+GLC) supports synthesized using the different fuel-oxidant ratios, there were observed differences in the diffraction peak intensities. The stoichiometric CN+GLC and CAN+GLC combustion systems exhibited the most intense diffraction peaks, with the fuel-lean combustion cases exhibiting lower and broader diffraction peaks. The line broadening of the fuel-lean combustion systems indicated towards a lower crystalline quality. Similar to the differences in the diffraction peak intensities, there was also a variation in the CeO_2 crystallite sizes with varying fuel-oxidant ratio. A maximum in CeO_2 crystallite size was observed for the CeO_2 supports synthesized using the stoichiometric CN+GLC and CAN+GLC combustion systems (25 nm and 39 nm respectively), see Figure 5.6 b). The smallest crystallite sizes were observed for the CeO_2 supports synthesized using a fuel-lean combustion system (φ = 0.5).

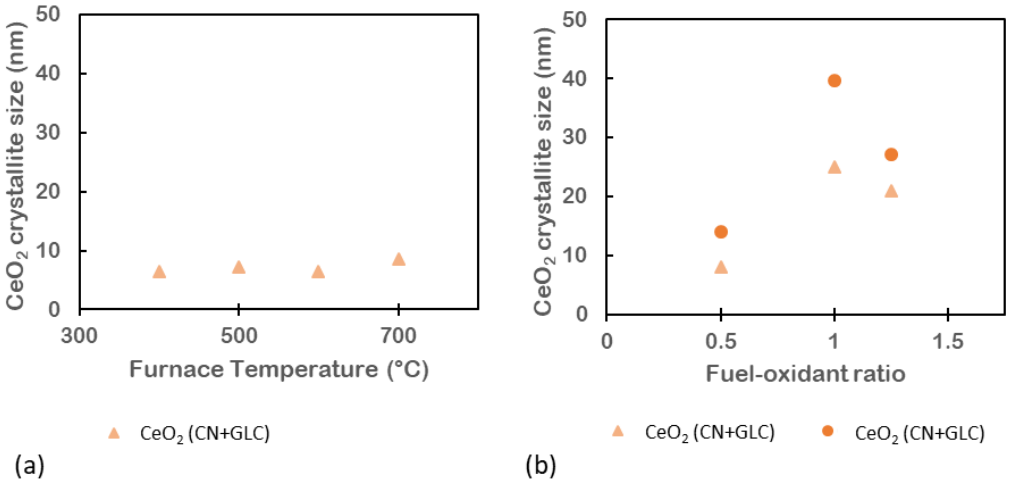

Figure 5.6: XRD crystallite size of the CeO_2 supports synthesized using (a) varying furnace temperatures and (b) varying Ce-precursors (CN and CAN) and fuel-oxidant ratios (φ = 0.5, 1, 1.25).

In agreement with the results of Kang, Ozgur and Varma (2018), Mokkelbost *et al.* (2004) and Purohit *et al.* (2001), this study also shows that the degree of crystallinity and crystallite size of ceria

supports depended on the chosen fuel-oxidant ratio. The difference in crystalline quality and crystallite size with varying fuel-oxidant ratio was attributed to the difference in the flame temperatures of the combustion systems which is dependent on the adopted SCS parameters (Ce-precursor type and fuel-oxidant ratio). The stoichiometric combustion systems ($\varphi = 1$) are associated with the maximum flame temperatures and hence powders synthesized using this ratio had the highest crystalline quality and crystallite sizes.

There was no significant difference observed in the crystalline quality or crystallite sizes of the CeO_2 supports using the two different Ce-precursors (CN and CAN) although a larger CeO_2 crystallite size using the CAN precursor was expected due to the higher flame temperature. This result suggests that the slightly higher flame temperature (CAN: 1900 °C vs CN: 1850 °C for $\varphi = 1$) of the CAN+GLC system was opposed by the associated higher gas evolution (CAN: 21.4 moles vs CN: 15.3 moles for $\varphi = 1$). The expected larger particle size was therefore suppressed by the cooling effect of the larger gas evolution.

To sum up, the results of this study confirm that the fuel-oxidant ratio subsequently has a larger influence on the crystalline quality and crystallite size than the Ce-precursor type as the fuel-oxidant ratio has the greatest effect on the flame temperature as discussed in section 2.4.2.

5.3.3. Brunauer-Emmet-Teller Specific Surface Area

The Brunauer-Emmet-Teller (BET) specific surface areas of the CeO_2 (CN+GLC) and CeO_2 (CAN+GLC) supports were determined by N_2-physisorption. Appendix C.2. N2-physisorption summarises the N_2 adsorption-desorption isotherms of the CeO_2 (CN+GLC) and CeO_2 (CAN+GLC) supports. The isotherms exhibited a composite shape of a type II isotherm shape and a type IV isotherm shape according to the IUPAC classification (Thommes *et al.*, 2015). This type of isotherm shape is characteristic of materials with a broad pore size distribution in the meso (2 – 50 nm) and macro (> 50 nm) pore range. The hysteresis loop was a type H3 loop which indicates a disordered porous material with a nonuniform pore network. The low adsorption at low p/p_0 ratios indicated that few micropores existed.

N_2-physisorption of CeO_2 (CN+GLC) and CeO_2 (CAN+GLC) supports demonstrated low surface areas (11 – 32 m^2/g), see Figure 5.7. For the synthesis of CeO_2 using a CN+GLC combustion system, there was an observed local maximum in BET surface area (28 m^2/g) for a stoichiometric combustion system, see Figure 5.7. Conversely, the CAN+GLC combustion system displayed a minimum in BET surface area (11 m^2/g) for the same fuel-oxidant ratio. Therefore, the effect of combustion temperature and gas evolution on the specific surface area of the CeO_2 supports synthesized using varying fuel-oxidant ratios and Ce-precursor type results in a complex behaviour. Mokkelbost *et al.* (2004) and Kang, Ozgur and Varma (2018) observed the same opposing trends in the specific surface areas of the CeO_2 (CN+GLC) and CeO_2 (CAN+GLC) supports as found in this study. It is understood that gas evolution has a suppressive effect on particle agglomeration thereby creating powders with large specific surface areas (Hwang *et al.*, 2006; Varma *et al.*, 2016; Kang *et al.*, 2018). In terms of BET surface area, it was not trivial to isolate the dominating factor controlling this physical property, rather, the resulting specific surface area was probably the result of the complex interaction of the simultaneous effects of the flame temperature and the gas evolution.

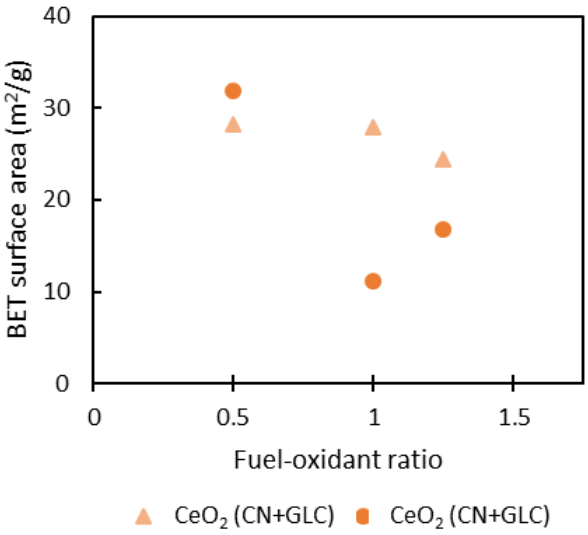

Figure 5.7: BET surface areas of the CeO_2 (CN+GLC) and CeO_2 (CAN+GLC) supports determined by N_2-physisorption.

5.4. Characterization of the Catalysts

This section details the physical and chemical characteristics of the two sets of catalysts synthesized using the conventional impregnation approach (IWI catalysts) and the one-shot SCS approach (SCS catalysts) as detailed in section 4.1.

5.4.1. Thermogravimetric measurements

Similar to the set of CeO_2 support powders, thermogravimetric measurements of the set of SCS catalyst powders were performed to determine the extent of combustion of the CN+GLC and CAN+GLC combustion systems used to synthesize these catalysts. The TGA-DTG-DTA curves of the SCS (CN+GLC) and SCS (CAN+GLC) support powders are shown in Figure 5.8 and Figure 5.9 respectively. The peak shapes of the TGA-DTG-DTA curves of the set of SCS catalysts were very similar to the set of CeO_2 supports. The SCS (CN+GLC) and SCS (CAN+GLC) catalysts exhibited analogous overall weight losses to the overall weight losses CeO_2 (CN+GLC) and CeO_2 (CAN+GLC) supports upon temperature-programmed treatment to 600 °C (in the range of 0.6 – 2.6 % compared to 0.8 – 3.7 % respectively).

Similar to the set of CeO_2 supports, the set of SCS catalysts also exhibited a weight loss (0.8 ± 0.1 %) over the temperature range of 50 – 200 °C which was also attributed to the removal of physisorbed water from the surface of the SCS catalysts. Furthermore, the SCS (CN+GLC) and SCS (CAN+GLC) catalysts synthesized using the fuel-lean conditions (φ = 0.5) also exhibited an additional weight loss peak above 100 °C similar to the CeO_2 (CN+GLC) and CeO_2 (CAN+GLC) supports also synthesized using these fuel-lean conditions. Since the temperature range for this broad weight loss (200 – 600 °C) of the SCS (CN+GLC) and SCS (CAN+GLC) catalysts also corresponded with the decomposition temperature ranges of the CN, CAN and GLC precursors (220 – 550 °C), this weight loss was also attributed to the incomplete combustion and thermal decomposition of the fuel and the nitrate Ce-precursors.

The thermogravimetric measurements of the set of SCS catalysts were very similar to those of the set of CeO_2 supports, and therefore their interpretation was also similar. Likewise, since the overall weight loss (in the range of 0.6 – 2.6 %) of the set of SCS catalysts upon temperature-programmed treatment to 600 °C is negligible compared to the average weight loss that occurred within the combustion reaction (~ 72 %), calcination of the set of SCS was not carried out prior to further characterization.

According to the results of this study, calcination is not required as a final preparations step for the removal of carbon and nitrate residues following SCS as complete combustion was achieved.

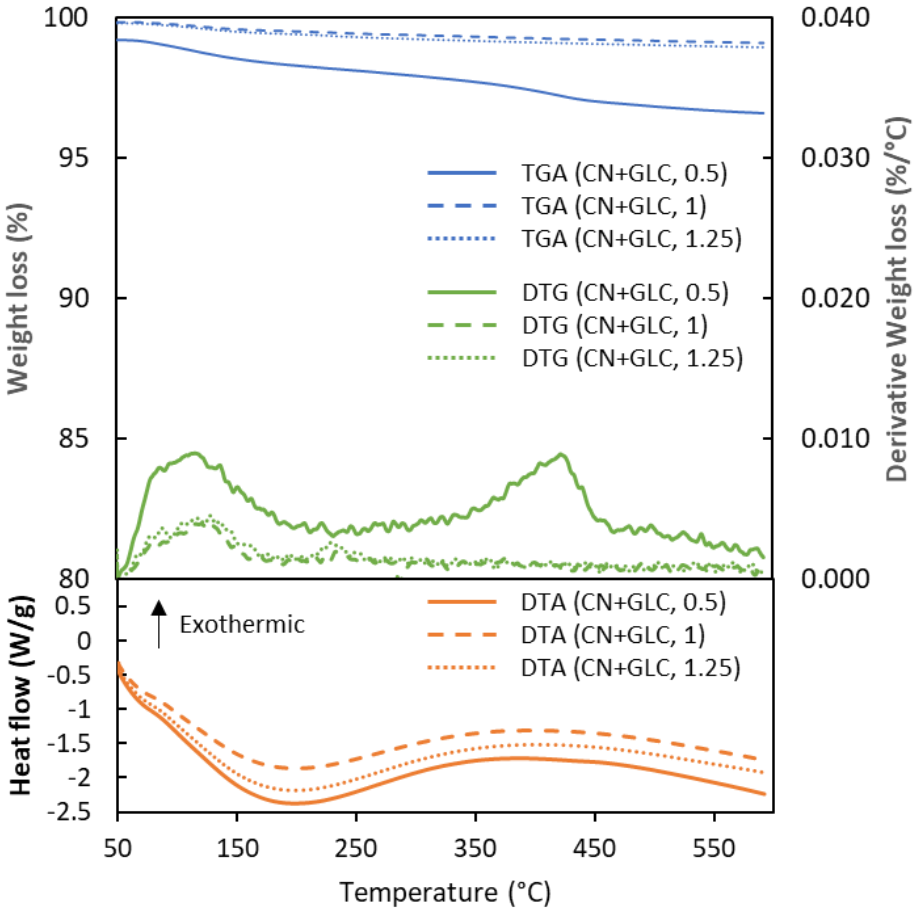

Figure 5.8: TGA-DTG-DTA curves of the SCS (CN+GLC) catalysts supports synthesized using varying fuel-oxidant ratios.

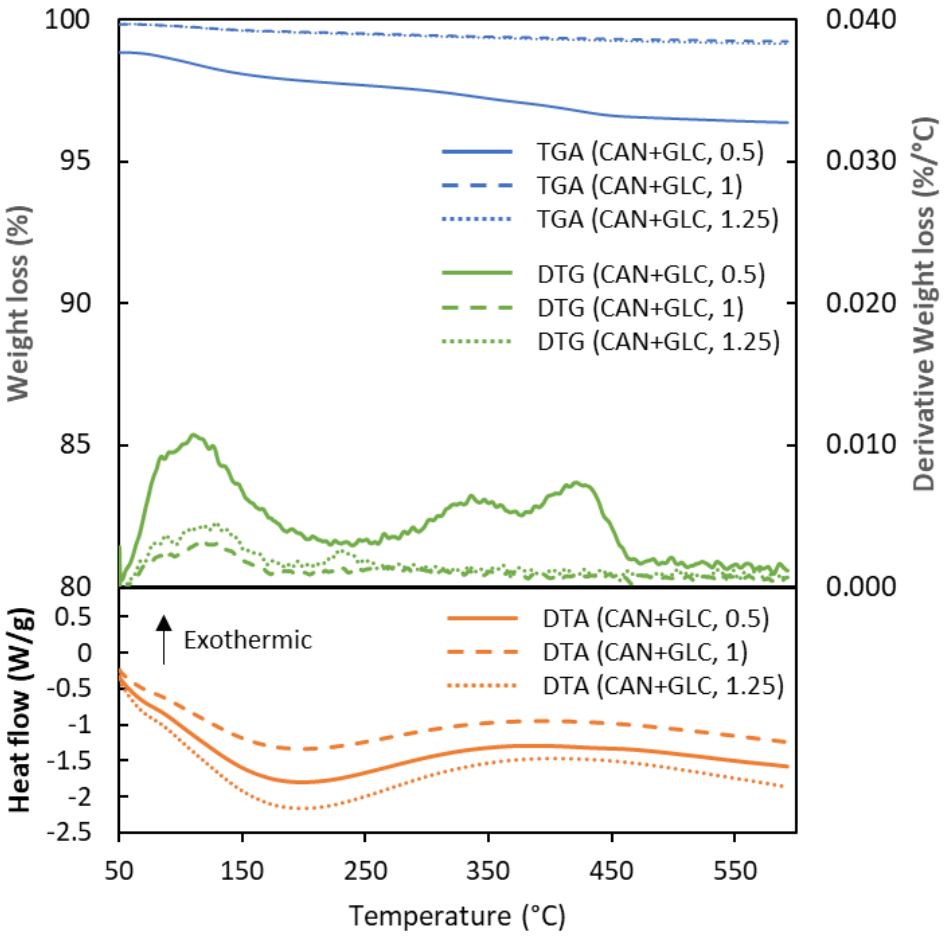

Figure 5.9: TGA-DTG-DTA curves of the SCS (CAN+GLC) catalysts supports synthesized using varying fuel-oxidant ratios.

Table 5.4: Evaluation of the TGA curves of the set of SCS catalysts (see Figure 5.8 and Figure 5.9).

CeO_2 Support	**Temperature range (°C)**	**Observed Mass Change (%)**
SCS (CN+GLC, 0.5)	50 – 200	0.9
	200 – 600	1.7
SCS (CN+GLC, 1)	50 – 600	0.7
SCS (CN+GLC, 1.25)	50 – 600	0.9
SCS (CAN+GLC, 0.5)	50 – 200	1.0
	200 – 600	1.5
SCS (CAN+GLC, 1)	50 – 600	0.6
SCS (CAN+GLC, 1.25)	50 – 600	0.7

5.4.2. X-Ray Diffraction

The XRD crystallite phases and sizes of the sets of SCS and IWI catalysts were very similar to those of the set of CeO_2 supports. The diffractograms of the set of CeO_2 supports (Figure 8.3), the set of SCS catalysts (Figure 8.4) and the set of IWI catalysts (Figure 8.5) are found in Appendix C: Summary of the Characterizations

This appendix provides supporting information for chapters 4 and 5.

The diffractograms of the sets of SCS and IWI catalysts exhibited similar variations in the diffraction intensity and line broadening as observed in the diffractograms of set of CeO_2 supports.

Consequently, the calculated crystallite sizes of the ceria supports in the set of SCS catalysts were very similar to the crystallite sizes of the set of CeO_2 supports. Similar to the set of CeO_2 supports, the crystallite sizes of the ceria supports for the set of SCS catalysts also exhibited a maximum for the SCS catalysts synthesized using the stoichiometric CN+GLC and CAN+GLC combustion systems (34 nm and 40 nm respectively), see Figure 5.10 a). Furthermore, there was no significant difference in the ceria crystallite sizes of the set of IWI catalysts compared to the ceria crystallite sizes of the set of CeO_2 supports. This indicates that impregnation of Pt and subsequent calcination at 350 °C of the set of CeO_2 supports applied in the synthesis of the set of IWI catalysts had no significant effect on the ceria crystallite sizes of the supports. Therefore, the set of CeO_2 supports retain their crystallographic properties during the conventional impregnation approach of the synthesis of the set of IWI catalysts.

To sum up, the crystallite sizes of the ceria supports for the set of CeO_2 supports, the sets of SCS and IWI catalysts were very similar to each other as the ceria supports were all synthesized using the same combustion systems (CN+GLC and CAN+GLC) and the same fuel-oxidant ratios (φ = 0.5, 1, 1.25). For this reason, the conclusions drawn for the sets of SCS and IWI catalysts are synonymous with the conclusions drawn for set of CeO_2 supports as detailed earlier in section 5.3.2. The results of this study confirm that the fuel-oxidant ratio determines the degree of crystallinity and crystallite size of ceria supports of the sets of SCS and IWI catalysts.

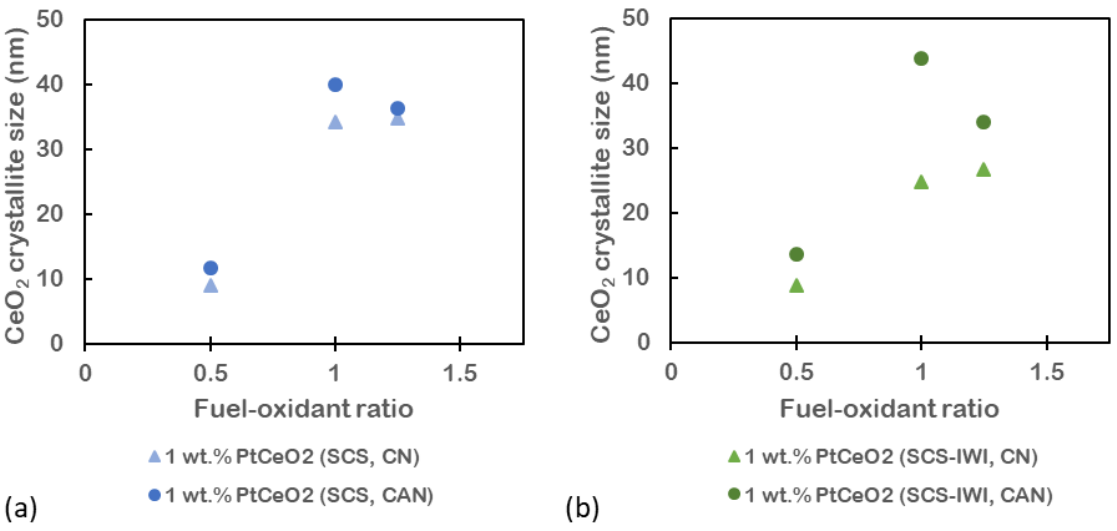

Figure 5.10: XRD crystallite sizes of the sets of (a) SCS and (b) IWI catalysts.

5.4.3. Brunauer-Emmet-Teller Specific Surface Area

N_2-physisorption of the sets of SCS and IWI catalysts demonstrated low surface areas (9 – 37 m^2/g), see Figure 5.11 a) and b).

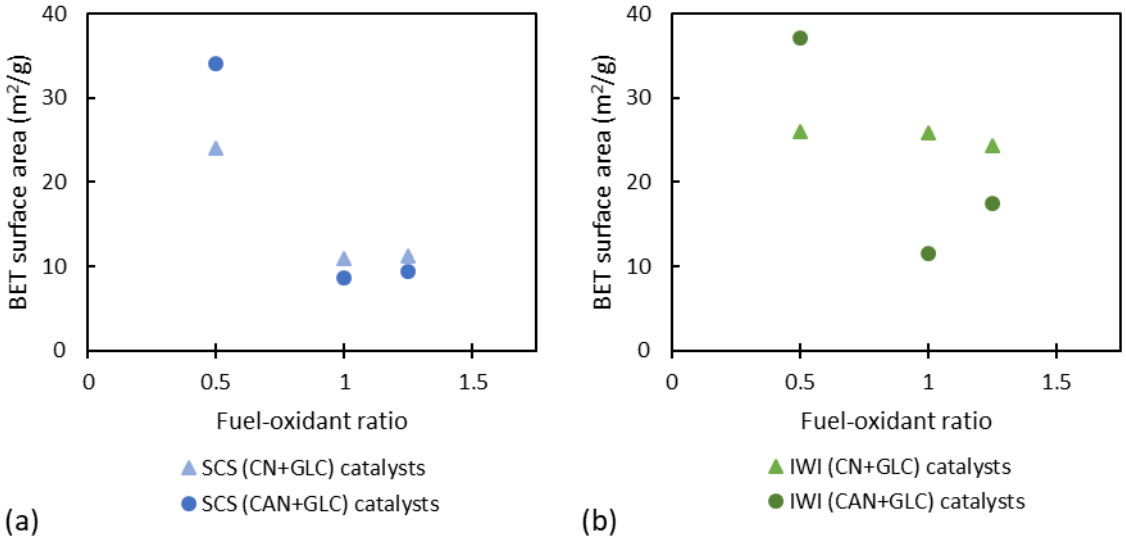

Figure 5.11: BET surface areas of the sets of (a) SCS and (b) IWI catalysts.

There was no significant difference in the specific surface areas of the SCS (CAN+GLC) catalysts and the CeO_2 (CAN+GLC) supports. Therefore, the addition of Pt-salt to the CAN+GLC combustion matrix for synthesis of the SCS (CAN+GLC) catalysts does not significantly alter the surface area of these catalysts with respect to the CeO_2 (CAN+GLC) supports. This similarity in the specific surface areas was as expected, as the combustion reactions for the synthesis of the CeO_2 (CAN+GLC) supports and the SCS (CAN+GLC) catalysts were very similar in exothermicity and gas evolution. The difference in exothermicity and gas evolution between the combustion reactions for the synthesis of the CeO_2 (CAN+GLC) supports and the SCS (CAN+GLC) catalysts was $-\Delta H^0$ (298K) = 5 kcal/mol and 0.06 mol of gas respectively.

A similarity in the specific surface areas of the CeO_2 (CN+GLC) supports and the SCS (CAN+GLC) catalysts was also expected due to the similarity in the exothermicity and gas evolution of the combustion reactions for the synthesis of these supports and catalysts. However, opposing trends were observed in the specific surface areas of the CeO_2 (CN+GLC) supports and the SCS (CAN+GLC) catalysts with varying fuel-oxidant ratio, see Figure 5.7 for the surface areas of the CeO_2 supports and Figure 5.11 a) for the surface areas of the SCS catalysts. The CeO_2 (CN+GLC) supports exhibited a maximum in specific surface area (28 m^2/g), whereas the SCS (CN+GLC) catalysts exhibited a minimum in specific surface area (11 m^2/g) for a stoichiometric combustion system. This suggests that there is an additional factor influencing the specific surface areas of these supports and catalysts. The presence of tetra-ammine platinum (II) nitrate, $Pt(NH_4)_4(NO_3)_2$, in combination with the CN in the combustion matrix must play a role in this difference in the trend of the specific surface area with varying fuel-oxidant ratio, as this is the sole factor separating the two sets of CeO_2 (CN+GLC) supports and SCS (CAN+GLC) catalysts. However, it is not clear why the combination of tetra-ammine platinum (II) nitrate with CN causes this difference.

The BET specific surface areas of the set of CeO_2 supports did not change with Pt impregnation and calcination at 350 °C for 3 hours, applied in the synthesis of the set of IWI catalysts (see Figure 5.7 for

the surface areas of the set of CeO_2 supports and Figure 5.11 b) for the surface areas of the set of IWI catalysts). This indicates that no significant sintering of the CeO_2 supports occurred during the calcination applied in the synthesis of the set of IWI catalysts.

The highest BET surface areas of the set of SCS and IWI catalysts were observed for fuel-lean ($\varphi = 0.5$) combustion systems.

5.4.4. Inductively Coupled Plasma – Atomic Emission Spectroscopy

Inductively Coupled Plasma – Atomic Emission Spectroscopy (ICP-AES) analysis was conducted to determine the Pt metal loading on the ceria supports. The target value was a loading of 1 wt.% Pt on the CeO_2 support.

Some of the SCS and IWI catalysts had much lower Pt loadings determined by ICP-AES compared with the target value of 1 wt.%, as low as 0.63 % and 0.88 % (see Table 5.5). It was noted that when doing ICP-AES analysis, not all of the 100 mg of catalyst sample was digested in the acid solution, even after digestion in the MARS-5 microwave digester at 180 °C. For the conventional impregnation synthesis approach, it is unlikely that a lower Pt loading was achieved. Therefore, as complete digestion was not achieved, the ICP-AES determined Pt metal loading was most likely lower than the actual Pt content in the IWI catalysts. For this reason, the ICP-AES determined Pt loadings of the set of SCS and IWI catalysts were slightly than the target value of 1 wt.%. Nonetheless, it was considered that the average Pt metal loadings of the set of SCS catalysts (0.97 ± 0.05 wt.%) and the set of IWI catalysts (0.92 ± 0.14 wt.%) corresponded well with the target value of 1 wt.%. Furthermore, the ICP-AES analysis of certain samples were repeated, and the standard deviation of the Pt loadings was between 0.02 and 0.05 %. Therefore, the lower Pt loadings measured for the SCS and IWI catalysts with Pt loadings of 0.63 % and 0.88 % were attributed to inaccuracies in that single measurement and it not an accurate reflection of the true loading.

Table 5.5: Pt loadings of the sets of SCS and IWI catalysts determined from ICP-AES analysis.

Notation	**Pt Loading (wt. %)**
SCS (CN+GLC, 0.5)	1.04
SCS (CN+GLC, 1)	0.96
SCS (CN+GLC, 1.25)	1.04
SCS (CAN+GLC, 0.5)	0.88
SCS (CAN+GLC, 1)	0.96
SCS (CAN+GLC, 1.25)	0.96
IWI (CN+GLC, 0.5)	1.08
IWI (CN+GLC, 1)	0.93
IWI (CN+GLC, 1.25)	1.02
IWI (CAN+GLC, 0.5)	0.88
IWI (CAN+GLC, 1)	0.96
IWI (CAN+GLC, 1.25)	0.63

5.4.5. Transmission Electron Microscopy

Transmission electron microscopy (TEM) was used to determine the Pt particle size distribution and dispersion on the sets of SCS and IWI catalysts synthesized using the CN+GLC and CAN+GLC combustion systems. The set of SCS catalysts were studied as prepared and the set of IWI catalysts were observed under TEM after calcination at 350 °C for 3 hours. Due to the similarity in the atomic masses of Pt and Ce, the contrast between the Pt particles and the cerium (IV) oxide support was low in bright-field TEM images. For this reason, HAADF images were also recorded as the contrast is improved using this technique. The bright-field detector captures the forward-scattered electrons whereas the HAADF detector captures the higher scattered electrons. In the bright-field TEM images, the dark spots would correspond to Pt and in HAADF images the lighter spots would correspond to Pt. Despite the availability of these two images, it was still difficult to differentiate between Pt particle clusters and thicker regions of the CeO_2 support, especially for the set of IWI catalysts. The bright-field TEM and corresponding HAADF images are shown in Figure 8.12 – Figure 8.17 in Appendix C.3 Transmission Electron Microscopy Images. The Pt particle size distribution graphs are also found in Appendix C.3 Transmission Electron Microscopy Images.

The Pt particles on the set of SCS catalysts were well dispersed over the CeO_2 support. Polyhedral-like holes/pits were observed in the ceria grains. Broad Pt particle size distributions were observed for the SCS catalysts synthesized using both the CN+GLC and CAN+GLC combustion systems. The Pt particle sizes were marginally affected by the fuel-oxidant ratio for the SCS (CN+GLC) and SCS (CAN+GLC) catalysts, see Table 5.6. The average Pt particle sizes for the CN+GLC and CAN+GLC combustion systems with varying the fuel-oxidant ratio varied between 2.3 – 3.1 nm and 2.9 – 3.5 nm respectively. The average Pt particle sizes of the SCS (CAN+GLC) catalysts were slightly larger in size compared to the average Pt particle sizes of the SCS (CN+GLC) catalysts. This could be due to the overall slightly higher flame temperature of the CAN+GLC combustion system compared to the CN+GLC combustion system (see Figure 2.5 in section 2.4.1). The average Pt particle sizes of set of IWI catalysts were much smaller than those of the set of SCS catalysts. Not all the bright-field and HAADF images taken for the IWI catalysts were used in determining the Pt particle size distribution as the contrast of some of these images was too poor to confidently distinguish between Pt particles and agglomerates of ceria support. In fact, for the IWI (CN+GLC, 0.5) and IWI (CAN+GLC, 1.25) catalysts none of the images taken yielded an appropriate level of contrast between the ceria support and the Pt particle to confidently determine the Pt particle size distribution. The overall average Pt particle size for the set of IWI catalysts was 1.1 ± 0.4 nm.

Table 5.6: TEM determined average Pt particle size for the sets of SCS and IWI catalysts.

Property	**SCS, CAN**			**SCS, CN**			**Units**
	0.5	**1**	**1.25**	**0.5**	**1**	**1.25**	
SCS catalysts	2.9 ± 1.4	3.1 ± 1.4	3.5 ± 1.3	2.3 ± 0.9	2.6 ± 0.9	3.1 ± 1.3	nm
IWI catalysts	1.7 ± 0.7	1.1 ± 0.3	-	-	1.1 ± 0.3	1.2 ± 0.4	nm

5.4.6. X-Ray Photoelectron Spectroscopy

X-Ray Photoelectron Spectroscopy (XPS) was used to determine the oxidation state of the Pt species on the surface of the set of SCS catalysts. The spectral analysis – background spectral subtractions and peak fittings – was carried out using IGOR Pro 6.37 software with the XPST extension package.

The high-resolution spectra of the C 1s peaks were best fitted with four singlets using a Gaussian-Lorentzian line shape (see Figure 5.12 and C.4.3. Fitted Peak Parameters

Table 8.3 in Appendix C.4 XPS Spectra for fitted peaks and peak parameters). The C 1s fittings exhibited evidence of charging as much as 2.4 ± 0.1 eV. All the C 1s spectra had a dominating hydrocarbon (C–C, C–H) signal which was used in the spectral correction to 284.4 ± 0.1 eV (Wagner *et al.*, 1979). The three additional singlets were fitted at higher binding energies (285.8 ± 0.2 eV, 287.2 ± 0.1 eV and 288.4 ± 0.2 eV) which were assigned to the alcohol/ether (–COH, –COC–), carbonyl (–C=O) and ester (–OC=O) functionalities (Gardner *et al.*, 1995; Estrade-Szwarckopf, 2004).

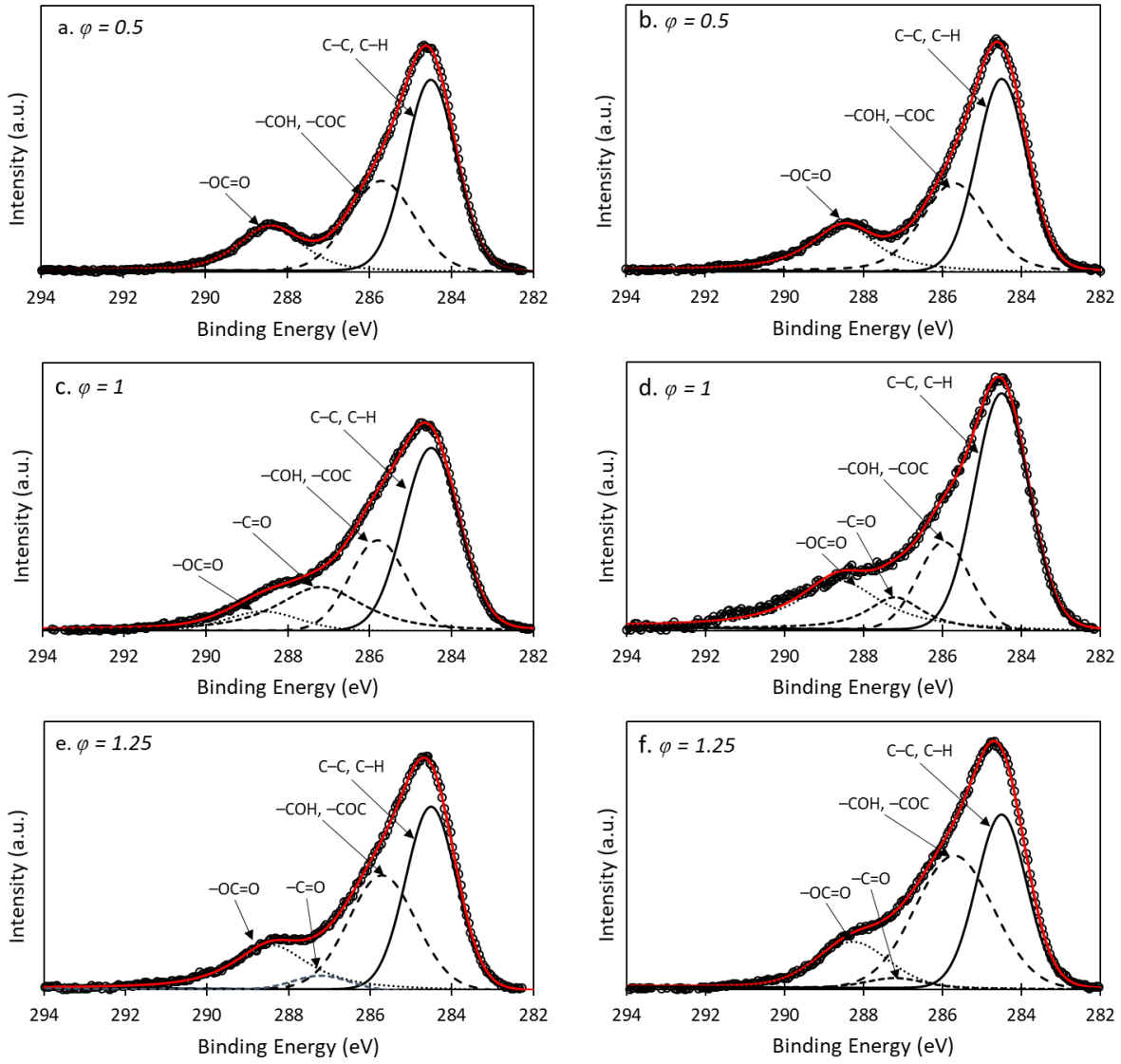

Figure 5.12: Fitted C 1s spectrum of the (a, c, e) SCS (CAN+GLC) catalysts and (b, d, f) SCS (CN+GLC) catalysts.

The high-resolution spectra of the Pt 4f peaks were fitted after spectral correction with three doublets representing the three expected Pt oxidation states (Pt^0, Pt^{2+} and Pt^{4+}), see Figure 5.13. The peak position of the doublet assigned to the Pt^0 state was constrained to the reference value of 71.2 $\pm$ 0.5 eV (Wagner *et al.*, 1979). The peak positions of the doublets assigned to the Pt^{2+} and Pt^{4+} oxidation states were constrained to a shift of +1.0 – 3.0 eV and +3.6 – 4.5 eV towards higher binding energies (BEs), with reference to the $4f_{5/2}$ Pt^0 doublet peak based on peak shifting observed in literature (Bera *et al.*, 2000; Bera *et al.*, 2003a; Bera *et al.*, 2003b; Hatanaka *et al.*, 2009).

See Table 5.7 for the relative amounts of the different Pt oxidation states calculated using the peak areas, also referred to as peak intensity. The valence distribution of the Pt species (the Pt^0, Pt^{2+} and Pt^{4+} contributions) was only slightly influenced by the fuel-oxidant ratio used in the synthesis of the set of SCS catalysts. Using a CAN+GLC combustion systems for the one-shot synthesis of 1 wt.% Pt/CeO_2 resulted in the preferential formation of the Pt^{2+} oxidation (> 53 %). Varying the fuel-oxidant ratio used in the synthesis of the SCS (CAN+GLC) catalysts resulted in a decrease in the Pt^{2+} oxidation from 75 % to 53 %. The contribution of the Pt^{4+} phase in the SCS (CAN+GLC) catalysts appeared to have reached a local maximum for a stoichiometric combustion mixture (φ = 1). Furthermore, the contribution of the Pt^0 phase in these catalysts was low across all fuel-oxidant ratios (< 11 %). For the SCS catalysts synthesized using the CN+GLC combustion system, there was not a clear preferential formation between the Pt^{2+} and Pt^{4+} phases across the fuel-oxidation ratios. Rather, the contribution of the Pt^{2+} phase increased (from 37% to 57%) while the contribution of the Pt^{4+} decreased (from 62 % to 40%) with increasing fuel-oxidant ratio. The contribution of the Pt^0 phase in the SCS (CN+GLC) catalysts also remained very low (< 6%) throughout.

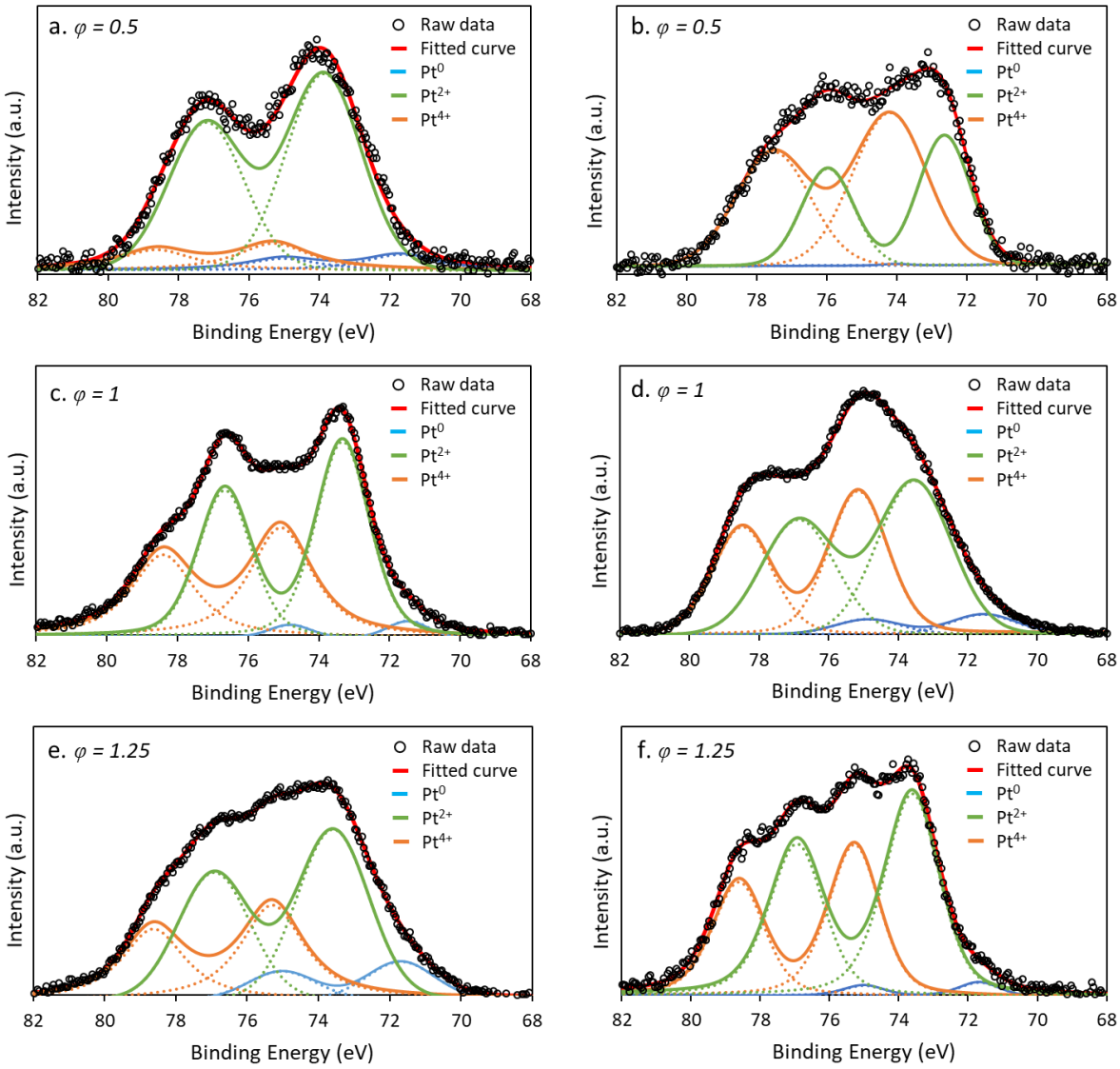

Figure 5.13: Fitted Pt 4f spectrum of the (a, c, e) SCS (CAN+GLC) catalysts and (b, d, f) SCS (CN+GLC) catalysts.

Table 5.7: Valence distribution of the Pt species (the Pt^0, Pt^{2+} and Pt^{4+} contributions) of the set of SCS catalysts.

Pt Oxidation State	**SCS, CAN**			**SCS, CN**		
	0.5	**1**	**1.25**	**0.5**	**1**	**1.25**
Pt^0	9%	3%	11%	0%	6%	3%
Pt^{2+}	75%	54%	53%	37%	52%	57%
Pt^{4+}	16%	43%	36%	62%	42%	40%

5.5. Water-Gas Shift Activity Measurements

Figure 5.14 depicts the CO conversions of the calcined set of IWI catalysts and the as-prepared set of SCS catalysts versus the Time-on-Stream (ToS). The catalysts were loaded in triplicate to obtain the experimental variation. The IWI catalyst supports and the SCS catalysts synthesized using the CN+GLC combustion system are depicted with triangles and the catalysts synthesized using the CAN+GLC combustion system are depicted with circles. The space velocities of the catalysts were the same, as the same catalysts mass (23 mg) was loaded for each IWI and SCS catalysts tested (see Appendix D.1. Catalyst Loading Procedure for the catalysts loadings and the random placements of the catalysts within the Flowrence setup).

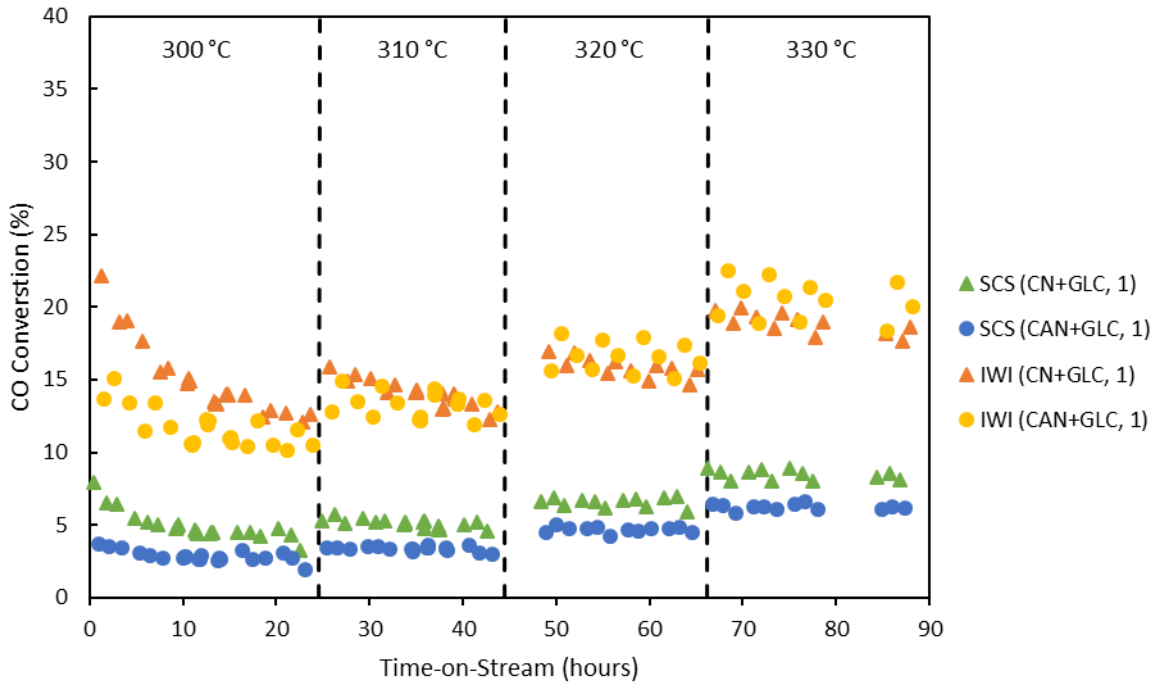

Figure 5.14: The CO conversion versus time-on-stream (in hours of the SCS and IWI catalysts.

The temperature of the WGS reaction was systematically increased from 300 °C to 330 °C. During the first 24 hours, there was a sharp decrease in CO conversion for both the IWI and SCS catalysts. This decrease in CO conversion is characteristic of the deactivation of the catalysts. Since catalysts can only be compared under stable conditions (where there is no deactivation) the WGS activity data for the run at 300 °C is disregarded in further evaluations. The average drop in CO conversion for the IWI and SCS catalysts for each of the runs at 310 °C, 320 °C and 330 °C was less than 1.7 % and 0.3 % respectively. Since the average drop in CO conversions for the IWI and SCS catalysts were very small, the catalysts were considered stable at 310 °C, 320 °C and 330 °C with no deactivation being observed. These conditions were therefore used in further evaluations.

The average CO conversions and standard deviation of the CO conversions of the triplicate IWI and SCS catalysts were calculated over the total Time-on-Stream ranges for each of the runs at 310 °C, 320 °C and 330 °C, see Table 5.8. The standard deviations of the CO conversions for the IWI and SCS catalysts fall within the expected range of experimental error as determined by statistical analysis by Luchters *et al.* (2017).

Table 5.8: Average CO conversions of the IWI and SCS catalysts

	Ave. CO Conversion (%)	Ave. CO Conversion (%)	Ave. CO Conversion (%)
SCS (CN+GLC, 1)	5.1 ± 0.3	6.6 ± 0.32	8.5 ± 0.3
SCS (CAN+GLC, 1)	3.4 ± 0.2	4.7 ± 0.2	6.2 ± 0.2
IWI (CN+GLC, 1)	14.0 ± 0.9	15.9 ± 0.7	18.9 ± 0.7
IWI (CAN+GLC, 1)	13.3 ± 0.9	16.6 ± 1.0	20.5 ± 1.3

The CO conversions of the IWI catalysts were roughly three time higher than the CO conversions of the SCS for each of the temperatures.

6. Discussion

The overall objective of this study was to compare the conventional impregnation approach of supports prepared via SCS and the one-shot SCS method for synthesizing Pt supported on CeO_2 catalysts for the WGS reaction. The WGS reactor is the largest component within fuel processors and thus remains one of the main obstacles in developing compact, commercially viable fuel processing units for the use with PEM fuel cells (Zalc and Loffler, 2002; Alijani and Irankhah, 2013). Within the context of South Africa's rich PGM reserves and the potential to add value to the mined Pt metal, Pt supported CeO_2 catalysts have been the focus of much research for the WGS reaction within HySA Catalysis.

This study hypothesizes that similar to the formation of metallic nickel particles under fuel-rich conditions (Kumar *et al.*, 2011; Manukyan *et al.*, 2013; Cross *et al.*, 2014), metallic phase Pt nano-crystallites supported on CeO_2 can be synthesized using a fuel-rich glycine-nitrate combustion system for the WGS reaction. This hypothesis stems from the formation of a reduction atmosphere (NH_3 gas) due to the combustion of the glycine fuel at the combustion front.

The 1 wt.% Pt/CeO_2 catalysts were prepared using two synthesis methods: (1) "conventional" incipient wetness impregnation of supports prepared via SCS and (2) one-shot SCS (preparation of the support and the active metal in one step), resulting in two different catalyst sets referred to as the IWI and SCS catalysts respectively.

Structural and spectroscopic characterizations reveal that the variation of the fuel-oxidant ratio used in both the CN+GLC and CAN+GLC combustion systems resulted in distinctive differences in the properties of the SCS catalysts and the CeO_2 supports of the IWI catalysts, namely the crystalline quality, the CeO_2 support crystallite sizes and the specific surface areas.

XRD characterization confirmed that the degree of crystallinity and crystallite size of the CeO_2 supports of the sets of IWI and SCS catalysts could be driven to a maximum using a stoichiometric fuel-oxidant ratio. This result agrees with the work of Kang, Ozgur and Varma (2018), Mokkelbost *et al.* (2004) and Purohit *et al.* (2001) where variation in crystalline quality and crystallite size was attributed to the difference in flame temperature for the combustion system which was more dependent on the fuel-oxidant ratio than the Ce-precursor type. The stoichiometric combustion systems ($\varphi = 1$) are associated with the maximum flame temperatures. Hence, the SCS catalysts and the CeO_2 supports prepared via SCS for the IWI catalysts prepared using this stoichiometric ratio had the highest crystalline quality and largest CeO_2 crystallite sizes.

The result of N_2-physisorption for the IWI and SCS catalysts indicated low surface areas (8 – 40 m^2/g). These low surface areas observed for the SCS catalysts and the CeO_2 supports prepared for the IWI catalysts correspond well with those obtained by Mokkelbost *et al.* (2004) and Kang, Ozgur and Varma (2018). The surface areas the sets of IWI and SCS catalysts could be driven to a maximum using fuel-lean combustion systems ($\varphi = 0.5$) as indicated in section 5.4.3. This result was unexpected as some literature sources claim that gas formation has a suppressive effect on particle growth and agglomeration (Alves *et al.*, 2013; Varma *et al.*, 2016). Therefore, theoretically, a higher fuel-oxidant ratio would increase the amount of gas formed during the reaction and therefore promote the formation of smaller and finer particles with high surface areas. However, the results of this study do not support this singular effect of gas evolution on surface area. Yet, there seems to be no other unified theory presented in literature to explain why the surface area is maximized using fuel-lean combustion systems. It appears that for fuel-lean conditions, the suppressive effect of gas evolution on particle

growth outweighs the effect of combustion temperature, thereby resulting in the synthesis of small particles with large surface areas.

The one-shot SCS approach was shown to achieve the desired loading of 1 wt.% Pt on CeO_2 (average loading of 0.97 $\pm$ 0.05 wt.%). This is in agreement with the Pt loadings obtained in the studies by Morfin *et al.* (2016) and Nguyen *et al.* (2015) who also synthesized 1 wt.% Pt/CeO_2 catalysts using a one-shot SCS approach and achieved the desired Pt loading. As expected, the use of the conventional impregnation approach resulted in the desired Pt loadings for the sets of IWI catalysts (average loading from ICP-AES analysis of 0.92 $\pm$ 0.14 wt.%).

There were several outliers within the sets of SCS and IWI catalysts for which the measured Pt loadings were less than expected, namely 0.63% and 0.88%, see section 5.4.4. A possible explanation is that during the digestion step of the ICP-AES analysis, not all of the catalyst sample was digested in the acid solution. Certain SCS and IWI catalyst samples were repeated to verify the accuracy of the ICP-AES measurement, and the standard deviation of the Pt loadings was between 0.2 and 0.5 %. Therefore, the incomplete digestion of the sample is likely responsible for the inaccuracy of the single ICP-AES measurements of the specific SCS and IWI catalysts with the lower Pt loadings of 0.63% and 0.88%.

The set of IWI catalysts synthesized using the conventional impregnation approach had much smaller Pt particles with narrow particle size distributions compared to the set of SCS catalysts (1.1 $\pm$ 0.4 nm compared to roughly 3.0 $\pm$ 1.2 nm). The larger Pt particle sizes of the SCS catalysts compared to the IWI catalysts can be attributed to sintering which occurred during SCS (high flame temperature). Particle growth rate was observed to increase with increasing temperature. Hence, despite the short duration of the combustion reaction, the elevated flame temperatures caused the Pt particles (during SCS) to attain larger sizes compared to the Pt particles of the IWI catalysts which were exposed to a lower temperature but for a longer period of time (adiabatic flame temperature of approximately 1900 °C for roughly 1 min compared to calcination at 350 °C for 3 hours). This result is in agreement with results found by Morfin *et al.* (2016) for which the 1 wt.% Pt/CeO_2 catalyst synthesized using the conventional impregnation approach had smaller Pt particle sizes compared to the same catalyst synthesized using the one-shot SCS approach (1.9 nm compared to 4.0 nm respectively).

TEM images of the set of SCS catalysts revealed highly dispersed Pt clusters on nanosized CeO_2 crystallites. The average Pt particle size was 3.0 $\pm$ 1.2 nm. The broad Pt particle size distribution ($\pm$ 1.2 nm) was in in good agreement with the Pt particle size distributions observed in the studies by Morfin *et al.* (2016) and Nguyen *et al.* (2015) who also synthesized 1 wt.% Pt/CeO_2 catalysts using a one-shot SCS approach. The Pt particle sizes of the SCS catalysts only marginally depended on the fuel-oxidant ratio used. Based on a literature search, there were no studies which describe the effect of the fuel-oxidant ratio on the Pt particle size for 1 wt.% Pt/CeO_2 catalysts synthesized using either a CN+GLC or a CAN+GLC combustion system to which these results can be directly compared. The one study that did investigate the influence of the fuel-oxidant ratio on supported metal catalysts concluded that ionic dispersion of the Mn ions into the ceria lattice was observed (Murugan *et al.*, 2008). Therefore, at present no comparisons can be made to any literature study.

XPS studies of the set of SCS catalysts showed that the Pt species on the surface of the CeO_2 support were predominantly stabilized in the 2+ and 4+ oxidation states (> 89% contribution). The Pt^{2+} valence state was the favoured state in the SCS (CAN+GLC) catalysts with more than > 53 % contribution. This strongly suggests that the Pt species on the ceria support is likely in the form of PtO and PtO_2 particles. Morfin *et al.* (2016) speculated that sub-stoichiometric Pt oxide phases were present in the 1wt.% Pt/CeO_2 catalysts synthesized in the study using a one-shot SCS approach. The Raman spectra

of these catalysts showed a broad Raman band from 500 to 750 cm^{-1} which coincides with peaks corresponding to the vibrations of Pt-O-Ce (548 cm^{-1}) and Pt-O (689 cm^{-1}) bonds. Morfin *et al.* (2016) attributed this to the formation of sub-stoichiometric Pt oxides. It should be noted that the crystallinity and stoichiometry of metal oxides strongly influence the strength of their Raman response (Brogan *et al.*, 1994; McBride *et al.*, 1998). On the other hand, XPS is a more sensitive technique in determining oxidation states of the Pt species on the surface of the ceria support as it does not rely on the species' crystallinity or stoichiometry. XPS spectra peaks are mainly affected by the loading of species of interest. The Pt loading of the SCS catalysts is far from the lowest detection limits of XPS which is 0.5 % (van der Heide, 2011). Therefore, since XPS is a more superior technique than Raman spectroscopy in determining Pt oxidation states of the Pt species on the ceria support, the results of this study are not in conflict with the results found by Morfin *et al.* (2016), but rather support the results found by Morfin *et al.* (2016). The deconvoluted XPS peaks revealed that there was some metallic Pt formation in the SCS catalysts although it was very low. According to literature, metallic phase formation is favoured under conditions in which there is excess NH_3 gas produced (Kumar *et al.*, 2011; Manukyan *et al.*, 2013; Cross *et al.*, 2014). This would explain why the SCS (CAN+GLC) catalysts had a higher contribution of the Pt^0 phase than the SCS (CN+GLC) catalysts as the decomposition of CAN also results in the formation of NH_3 gas. The highest contribution of Pt^0 was observed in the SCS (CAN+GLC, 1.25) catalyst, which was 11%. This indicates that fuel-rich conditions do favour the formation of some metallic Pt species by the reduction of the species due to the excess NH_3 produced from the combustion of the glycine fuel. However, this low contribution of metallic Pt does not support the hypothesis that predominantly metallic Pt species on ceria crystallites can be formed using a fuel-rich glycine-nitrate combustion system. The observations from TEM and XPS strongly suggest that using a one-shot glycine-nitrate combustion system results in the formation of mainly Pt oxide particles (PtO and PtO_2) on nanosized CeO_2 crystallites.

The WGS reaction with a synthetic reformate feed was used to compare the activity of the calcined IWI catalysts to the as-prepared SCS catalysts. The catalysts were chosen such that the same combustion systems (CN+GLC and CAN+GLC) and fuel-oxidant ratios ($\varphi = 1$) were used in the synthesis of the SCS catalysts and the CeO_2 supports for the IWI catalysts. Since the Pt oxidation state plays an important role in determining the activity of the catalysts towards the WGS reaction (Mei *et al.*, 2015), it is important to note that the Pt species of both of the SCS and IWI catalysts were in their oxidized states. XPS analysis showed that the Pt species of the as-prepared SCS catalysts were mainly present as Pt^{2+} and Pt^{4+} oxide species, with some formation of metallic Pt (less than 6 %). It is well-known and accepted that calcination results in the formation of metal oxide particles on the support, therefore the Pt species of the calcined IWI catalysts were also in their oxidized states. Hence, this renders the basis of comparison of the difference in WGS activity of the IWI and SCS catalysts to the difference in Pt particle sizes and the location of the Pt species in the 1 wt.% Pt/CeO_2 catalysts.

The results of the WGS activity measurements showed that the IWI catalysts were roughly three times more active as the SCS catalysts. The higher activity of the IWI catalysts compared to the SCS can be attributed to the smaller Pt particles achieved by the conventional impregnation approach. The average Pt particle size of the IWI catalysts was three times smaller than the average Pt particle size of the SCS catalysts (~ 1 nm compared to ~ 3 nm). It is well accepted that the WGS reaction occurs via the Pt particles at the interface of the Pt particle and the CeO_2 support (Liu *et al.*, 2010; Kalamaras *et al.*, 2011; Jain *et al.*, 2015). Therefore, smaller Pt particles would result in an increase in the exposed metal surface area and the interfacial area between the Pt particle and the CeO_2 support for the WGS reaction to occur. For this reason, the IWI catalysts were expected to be more active towards the WGS reaction than the SCS catalysts as the IWI catalysts had larger active surface areas.

However, the smaller Pt particles of the IWI catalysts is not the only explanation for their higher activity compared to the SCS catalysts: the location and accessibility of the Pt species in the SCS catalysts is another point of discussion.

Due to the intimate nature of mixing of the Pt-salt and the Ce-precursors within the aqueous solution for the one-shot synthesis of the SCS catalysts, partial incorporation of Pt into the CeO_2 lattice is possible. This incorporation of the Pt into the lattice would render some of the Pt in the SCS catalysts inaccessible to the WGS reaction and therefore inactive. However, XPS and XRD results of the SCS catalysts did not show positive results for the incorporation of Pt into the CeO_2 lattice.

This concept of Pt insertion into the CeO_2 achieved during one-shot SCS has been addressed in several other studies. The studies by Morfin *et al.* (2016) and Nguyen *et al.* (2015) synthesized the same 1 wt.% Pt/CeO_2 catalysts using the exact same one-shot CAN+GLC combustion system as used in this study. Both Morfin *et al.* (2016) and Nguyen *et al.* (2015) stated that although the lattice parameter data indicated some contraction of the ceria lattice, which is indicative of Pt incorporation into the CeO_2 lattice, this data alone could not prove nor disprove Pt insertion into the CeO_2 lattice. The 1 wt.% Pt loading was too low to induce significant measurable changes in the ceria lattice parameter to confidently ascertain Pt insertion into the lattice. It is therefore speculated that these variations in the ceria lattice could be due to the incorporation of some of the Pt species into the CeO_2 lattice while most of the Pt formed as particles on the CeO_2 support. Complete insertion of all of the Pt into the CeO_2 lattice at a 1 wt.% Pt loading has been observed in several other studies which used a different fuel, namely oxalyldihydrazide, in the one-shot SCS approach (Bera *et al.*, 2000; Bera *et al.*, 2003a; Bera *et al.*, 2003b). These oxalyldihydrazide combustion systems burn with roughly twice the exothermicity of the glycine combustion systems (ODH: $-\Delta H^0$ (298K) = 717 kcal/mol; GLC: $-\Delta H^0$ (298K) = 444 kcal/mol). It is speculated that this higher reaction enthalpy of the oxalyldihydrazide combustion provides enough energy to not only sustain the combustion reaction but also the activation energy for complete Pt inclusion into the CeO_2 lattice as this is a highly energy intensive process (Scanlon *et al.*, 2011).

Therefore, although XRD and XPS characterization results from this study could not conclusively prove Pt insertion into the CeO_2 lattice, the possibility of some Pt incorporation cannot be completely disregarded when synthesizing 1 wt.% Pt/CeO_2 catalysts using a glycine combustion system. Hence, the conjecture is that not all of the Pt species in the SCS catalysts were formed as particles but some of the Pt was incorporated into the CeO_2 lattice. For these reasons, it is hypothesized that the SCS catalysts had lower active surface areas compared to the IWI catalysts and therefore exhibited lower CO conversions.

It is important to bear in mind that this is a conjecture that still needs to be verified with additional characterization techniques, such as CO chemisorption to determine the Pt metal surface areas of the catalysts and possibly extended X-ray absorption fine structure (EXAFS) studies which would provide information regarding the coordination numbers and bond lengths and angles associated with the Pt species in the catalysts.

7. Conclusions and Recommendations

The aim of this study was to investigate the conventional impregnation and one-shot SCS approaches for the synthesis of 1 wt.% Pt/CeO_2 for the WGS reaction within fuel-processors. The WGS reactor remains the largest component within fuel-processors. Therefore, development of a highly active catalyst will reduce the amount of catalyst required and hence reduce the size of the WGS unit in the fuel-processor. The catalyst synthesis method intrinsically affects the activity of the catalysts as the synthesis method determines the morphological properties (active surface area / accessibility of the active sites) of the catalyst (Patil *et al.*, 2008).

This study has shown that Pt oxide clusters on low surface area nanosized CeO_2 crystallites can be prepared using the one-shot SCS approach. The fuel-oxidant ratio had the larger effect on the morphological properties of the SCS catalysts compared to the Ce-precursor type. XRD confirmed the synthesis of nano-sized CeO_2 crystallites with a cubic fluorite structure. The CeO_2 crystallite sizes were driven to maximum using a stoichiometric combustion system. This maximum in CeO_2 crystallite size was associated with a minimum in specific surface area. The specific surface area of the SCS catalysts could be driven to a maximum using fuel-lean SCS conditions. TEM and XPS analysis confirmed the presence of PtO and PtO_2 particles on the CeO_2 support. The SCS synthesis approach resulted in a reproducible metal loading with a reproducible, defined Pt particle size (average of 3 nm). The Pt particle sizes were only marginally affected by the fuel-oxidant ratio. Reduction of Pt particles to the metal is known to increase their WGS activity (Mei *et al.*, 2015), the fuel-rich combustion systems yielded Pt particles with the highest contribution of Pt^0 (11 %). The fuel-rich synthesis condition (φ = 1.25) obtained the best physical (reasonably high support surface area) and chemical properties (valence distribution of the Pt^0, Pt^{2+} and Pt^{4+} oxidation states with the highest contribution of Pt^0) of 1 wt.% Pt/CeO_2 catalysts.

The results of this study have shown that metallic Pt species supported on CeO_2 cannot be synthesized in one shot SCS using a fuel-rich glycine-nitrate combustion system, thus refuting the hypothesis. Future work to obtain metallic Pt may however may prove to be successful as the study by Cross *et al.* (2014) showed in their work that high surface area (155 m^2/g) metallic Ni catalysts supported on SiO_2 were synthesized using SCS under an inert atmosphere like argon. It is therefore recommended to repeat the one-shot SCS approach of synthesizing 1 wt.% Pt/CeO_2 using a fuel-rich synthesis condition (φ = 1.25) in an inert atmosphere instead of air as carried out in this study.

The one-shot SCS is a viable, one-step technique for synthesizing Pt supported on CeO_2 catalysts. However, the large Pt particle sizes of one-shot SCS catalysts synthesized using a glycine-nitrate combustion system render them less active for medium temperature WGS as compared to the Pt/CeO_2 catalysts prepared using the conventional impregnation approach. Therefore, it is recommended that other fuel types, such as urea, which burn with lower flame temperatures also be investigated. The study by Vita *et al.* (2015a) showed in their work on Ni/CeO_2 catalysts that the NiO particle size obtained using a urea combustion system was five times smaller than the NiO particle size achieved using a glycine combustion system due to a lower flame temperature of the urea combustion system. A urea combustion system could combine the good Pt dispersion achieved using the one-shot SCS approach with potentially smaller Pt particle sizes, thereby increasing the Pt/CeO_2 catalyst's activity towards the WGS reaction. It should be noted that the possible advantage of the *in-situ* reduction of the Pt species using the glycine system is not possible with the urea system, as it is known that the decomposition of urea does not result in the formation of NH_3 gas which is responsible for the reduction of the Pt species.

8. References

Ahmed, S. and Krumpelt, M. (2001) 'Hydrogen from hydrocarbon fuels for fuel cells', *International Journal of Hydrogen Energy*, 26, pp. 291–301.

Alijani, A. and Irankhah, A. (2013) 'Medium-Temperature Shift Catalysts for Hydrogen Purification in a Single-Stage Reactor', *Chemical Engineering and Technology*, 36(2), pp. 209–219.

Alves, A. K., Bergmann, C. P. and Berutti, F. A. (2013) *Novel Synthesis and Characterization of Nanostructured Materials*. Heidelberg, Germany: Springer.

Andrews, J. and Shabani, B. (2011) 'Re-envisioning the role of hydrogen in a sustainable energy economy', *International Journal of Hydrogen Energy*. Elsevier Ltd, 37(2), pp. 1184–1203.

de Araújo, G. C. and do Carmo Rangel, M. (2000) 'An environmental friendly dopant for the hightemperature shift catalysts', *Catalysis Today*, 62, pp. 201–207.

Aruna, S. T. and Mukasyan, A. S. (2008) 'Combustion synthesis and nanomaterials', *Current Opinion in Solid State and Materials Science*. Elsevier Ltd, 12(3–4), pp. 44–50.

Ayodele, B. V., Hossain, M.A., Chong, S.L., Soh, J.C., Abdullah, A., Khan, M.R. and Cheng, C.K. (2016) 'Non-isothermal kinetics and mechanistic study of thermal decomposition of light rare earth metal nitrate hydrates using thermogravimetric analysis', *Journal of Thermal Analysis and Calorimetry*. Springer Netherlands, 125(1), pp. 423–435.

Azzam, K. G., Babich, I.V., Seshan, K., and Leffrts, L. (2007) 'A bifunctional catalyst for the single-stage water-gas shift reaction in fuel cell applications. Part 2. Roles of the support and promoter on catalyst activity and stability', *Journal of Catalysis*, 251(1), pp. 163–171.

Bera, P., Patil, K.C., Jayaram, V., Subbanna, G.N. and Hedge, M.S. (2000) 'Ionic dispersion of Pt and Pd on CeO_2 by combustion method: Effect of metal-ceria interaction on catalytic activities for NO reduction and CO and hydrocarbon oxidation', *Journal of Catalysis*, 196(2), pp. 293–301.

Bera, P., Priolkar, K.R., Gayen, A., Sarode, P.R., Hedge, M.S., Emura, S., Kumashiro, R., Jayaram, V. and Subbanna, G.N. (2003a) 'Ionic dispersion of Pt over CeO_2 by the combustion method: Structural investigation by XRD, TEM, XPS, and EXAFS', *Chemistry of Materials*, 15(10), pp. 2049–2060.

Bera, P. Gayn, A., Hegde, M.S., Lalla, N.P., Spadaro, L., Frusteri, F., and Arena, F. (2003b) 'Promoting Effect of CeO_2 in Combustion Synthesized Pt/CeO_2 Catalyst for CO Oxidation', *The Journal of Physical Chemistry B*, 107(25), pp. 6122–6130.

Bera, P., Malwadkar, S., Gayen, A., Satyanarayana, C.V.V., Rao, B.S. and Hegde, M.S. (2004) 'Low-temperature water gas shift reaction on combustion synthesized $Ce_{1-x}Pt_xO_{2-\delta}$ catalyst', *Catalysis Letters*, 96(3–4), pp. 213–219.

Bianchetti, M. T., Juarez, R.E., Lamas, D.G., Walsoe de Reca, N.E., Perez, L., and Cabanillas, E. (2002) 'Nano-Blast Synthesis of Nano-size CeO_2–Gd_2O_3 Powders', *Journal of Materials Research*, 17(9), pp. 2185–2188.

Bohlbro, H. (1969) *Investigation on Kinetics of the Conversion of Carbon Monoxide with Water Vapour over Iron Oxide based Catalysts*. 2nd edition. Copenhagen: Haldor Topsoe Research Laborator.

Bondioli, F., Bonamartini Corradi, A., Leonelli, C., and Manfredini, T. (1999) 'Nanosized CeO_2 powders obtained by flux method', *Materials Research Bulletin*, 34(14), pp. 2159–2166.

Bouguer, P. (1729) *Essai d'Optique sur la Gradation de la Lumiere*. Paris, France: Claude Jombert.

Březina, F. and Rosický, J. (1963) 'Untersuchung des thermischen Zerfalles der Cernitratokomplexe', *Monatshefte für Chemie*, 94(1), pp. 306–311.

Brogan, M. S., Dines, T. J. and Cairns, J. A. (1994) 'Raman spectroscopic study of the Pt–CeO_2 interaction in the Pt/Al_2O_3–CeO_2 catalyst', *J. Chem. Soc., Faraday Trans.*, 90(10), pp. 1461–1466.

Brown, D. E. (2017) *Kinetic Models for the Pt/CeO_2 Catalysed Water-Gas Shift Reaction*. University of Cape Town.

Brunauer, S., Emmett, P. H. and Teller, E. (1938) 'Adsorption of Gases in Multimolecular Layers', *Journal of the American Chemical Society*, 60(2), pp. 309–319.

Chen, P. L. and Chen, I. W. (1993) 'Reactive cerium (IV) oxide powders by the homogeneous precipitation method', *Journal of the American Ceramic Society*, 76(6), pp. 1577–1583.

Chu, X., Chung, W. I. and Schmidt, L. D. (1993) 'Sintering of Sol—Gel-Prepared Submicrometer Particles Studied by Transmission Electron Microscopy', *Journal of the American Ceramic Society*, 76(8), pp. 2115–2118.

Cross, A., Roslyakov, S., Manukyan, K.V., Rouvimov, S., Rogachev, A.S., Kovalev, D., Wolf, E.E., and Mukasyan, A.S. (2014) 'In Situ Preparation of Highly Stable Ni-Based Supported Catalysts by Solution Combustion Synthesis', *The Journal of Physical Chemistry C*, 118(45), pp. 26191–26198.

Einstein, A. (1905) 'Ueber einen die Erzeugung and Verwandlung des Lichtes betreffenden heuristischen Gesichtspunkt', *Annalen der Physik*, 17, pp. 132–148.

Ersoz, A., Olgun, H. and Ozdogan, S. (2006) 'Reforming options for hydrogen production from fossil fuels for PEM fuel cells', *Journal of Power Sources*, 154, pp. 67–76.

Ertl, G., Knoezinger, H., Schueth, F., and Weitkamp, J. (eds) (2008) *Handbook of Heterogeneous Catalysis*. 2nd edn, *Wiley-VCH Verlag GmbH & Co. KGaA*. 2nd edn. Weinheim, Germany: Wiley-VCH Verlag GmbH & Co. KGaA.

Estrade-Szwarckopf, H. (2004) 'XPS photoemission in carbonaceous materials: A "defect" peak beside the graphitic asymmetric peak', *Carbon*, 42(8–9), pp. 1713–1721.

Faur Ghenciu, A. (2002) 'Review of fuel processing catalysts for hydrogen production in PEM fuel cell systems', *Current Opinion in Solid State and Materials Science*, 6(5), pp. 389–399.

Fogler, H. S. (2006) *Elements of Chemical Reaction Engineering*. 4th edn. Westford, Massachusetts: Pearson Eduction, Inc.

Fultz, B. and Howe, J. (2008) *Transmission Electron Microscopy and Diffractometry of Materials*. 3rd edn. Heidelberg, Germany: Springer-Verlag Berlin Heidelberg.

Gardner, S. D., Singamsetty, C.S.K., Booth, G.L., He, G., and Pittman, C.U. (1995) 'Surface characterization of carbon fibers using angle-resolved XPS and ISS', *Carbon*, 33(5), pp. 587–595.

Gayen, A., Boaro, M., de Leitenburg, C., Llorca, J., and Trovarelli, A. (2010) 'Activity, durability and microstructural characterization of ex-nitrate and ex-chloride Pt/$Ce_{0.56}Zr_{0.44}O_2$ catalysts for low temperature water gas shift reaction', *Journal of Catalysis*. Elsevier Inc., 270(2), pp. 285–298.

González-Cortés, S. L. and Imbert, F. E. (2013) 'Fundamentals , properties and applications of solid catalysts prepared by solution combustion synthesis (SCS)', *Applied Catalysis A, General*, 452, pp. 117–131.

Hadke, S., Kalimila, M.T., Rathkanthiwar, S., Gour, S., Sonkusare, R. and Ballal, A. (2015) 'Role of fuel and fuel-to-oxidizer ratio in combustion synthesis of nano-crystalline nickel oxide powders', *Ceramics*

International. Elsevier, 41(10), pp. 14949–14957.

Hatanaka, M., Takahashi, N., Takahashi, N., Tanabe, T., Nagai, Y, Suda, A., and Shinjah, H. (2009) 'Reversible changes in the Pt oxidation state and nanostructure on a ceria-based supported Pt', *Journal of Catalysis*. Elsevier Inc., 266(2), pp. 182–190.

van der Heide, P. (2011) *X-Ray Photoelectron Spectroscopy. An Introduction to Principles and Practices*. Hoboken, New Jersey: Wiley.

Hirano, M. and Kato, E. (1996) 'Hydrothermal synthesis of cerium (IV) oxide', *Journal of American Ceramic Society*, 79(3), pp. 777–780.

Hofmann, S. (2013) *Auger- and X-Ray Photoelectron Spectroscopy in Materials Science*.

Holladay, J. D., Hu, J., King, D.L, and Wang, Y. (2009) 'An overview of hydrogen production technologies', *Catalysis Today*, 139, pp. 244–260.

Hwang, C., Huang, T. and Tsai, J. (2006) 'Combustion synthesis of nanocrystalline ceria (CeO_2) powders by a dry route', *Materials Science and Engineering B*, 132, pp. 229–238.

International Centre for Diffraction Data (2008) *PDF-2 Release 2008 (Database)*. Newtown Square, USA.

International Energy Agency (2016) *World Energy Outlook 2016*. Available at: http://www.iea.org/newsroom/news/2016/november/world-energy-outlook-2016.html (Accessed: 19 April 2017).

Jacobs, G., Graham, U.M., Chenu, E., Patterson, P.M., Dozier, A., and Davis, B.H.(2005) 'Low-temperature water-gas shift: Impact of Pt promoter loading on the partial reduction of ceria and consequences for catalyst design', *Journal of Catalysis*, 229(2), pp. 499–512.

Jain, R., Poyraz, A.S., Gamliel, D.P., Valla, J., Suib, S.L., and Maric, R. (2015) 'Comparative study for low temperature water-gas shift reaction on Pt/ceria catalysts: Role of different ceria supports', *Applied Catalysis A: General*. Elsevier B.V., 507(October), pp. 1–13.

Jain, S. R., Adiga, K. C. and Verneker, V. R. (1981) 'A New Approach to Thermochemical Calculations of Condensed Fuel-Oxidizer Mixtures', *Combustion and Flame*, 40, pp. 71–79.

Jardim, E. O., Rico-Frances, S., Coloma, F., Anderson, J.A., Silvestre-Alvera, J. and Sepulveda-Escribano, A. (2015) 'Influence of the metal precursor on the catalytic behavior of Pt/Ceria catalysts in the preferential oxidation of CO in the presence of H_2 (PROX)', *Journal of Colloid and Interface Science*. Elsevier Inc., 443, pp. 45–55.

Kalamaras, C. M., Americanou, S. and Efstathiou, A. M. (2011) '"Redox" vs "associative formate with -OH group regeneration" WGS reaction mechanism on Pt/CeO_2: Effect of platinum particle size', *Journal of Catalysis*, 279(2), pp. 287–300.

Kang, W., Ozgur, D. O. and Varma, A. (2018) 'Solution Combustion Synthesis of High Surface Area CeO_2 Nanopowders for Catalytic Applications: Reaction Mechanism and Properties', *ACS Applied Nano Materials*, 1(2), pp. 675–685.

Kingsley, J. J. and Patil, K. C. (1988) 'A novel combustion process for the synthesis of fine particle a-alumina and related oxide materials', *Materials Letters*, 6(11–12), pp. 427–432.

Kleijn, R. and Voet, E. Van Der (2014) 'Resource constraints in a hydrogen economy based on renewable energy sources : An exploration Resource constraints in a hydrogen economy based on renewable energy sources ', *Renewable and Sustainable Energy Reviews*. Elsevier Ltd, 14(9), pp. 2784–

2795.

Kondarides, D. I. and Verykios, X. . (1998) 'Effect of Chlorine on the Chemisorptive Properties of Rh/CeO_2 Catalysts Studied by XPS and Temperature Programmed Desorption Techniques', *Journal of Catalysis*, 174(1), pp. 52–64.

Kumar, A., Cross, A., Manukyan, K., Bhosale, R.R., van den Broeke, L.J.P., Miller, J.T., Mukayan, A.S., and Wolf, E.E. (2015) 'Combustion synthesis of copper-nickel catalysts for hydrogen production from ethanol', *Chemical Engineering Journal*. Elsevier B.V., 278, pp. 46–54.

Kumar, A., Wolf, E. E. and Mukasyan, A. S. (2011) 'Solution combustion synthesis of metal nanopowders: nickel-reaction pathways', *American Institute of Chemical Engineers Journal*, 57(8), pp. 2207–2214.

Ladebeck, J. R. and Wagner, J. P. (2013) 'Catalyst development for water-gas shift', in Vielstich, W., Lamm, A., and Gasteiger, H. A. (eds) *Handbook of Fuel Cells – Fundamentals, Technology and Applications*. Chinchester: John Wiley & Sons, Ltd, pp. 190–201.

Larminie, J. and Dicks, A. (2003) *Fuel Cell Systems Explained*. West Sussex, England: John Wiley & Sons, Ltd,.

Lee, D. W. and Yoo, B. R. (2014) 'Advanced metal oxide (supported) catalysts: Synthesis and applications', *Journal of Industrial and Engineering Chemistry*. The Korean Society of Industrial and Engineering Chemistry, 20(6), pp. 3947–3959.

Li, J., Wang, Z., Yang, X., Hu, L. Liu, Y. and Wang, C. (2007) 'Evaluate the pyrolysis pathway of glycine and glycylglycine by TG-FTIR', *Journal of analytical and applied pyrolysis*, 80(1), pp. 247–253.

Liu, X., Ruettinger, W., Xu, X., and Farrauto, R. (2005) 'Deactivation of Pt/CeO_2 water-gas shift catalysts due to shutdown/startup modes for fuel cell applications', *Applied Catalysis B: Environmental*, 56(1–2), pp. 69–75.

Liu, Y., Wen, C., Guo, Y., Liu, X., Ren, J. Lu, G., and Wang, Y. (2010) 'Mechanism of CO Disproportionation on Reduced Ceria', *ChemCatChem*, 2(3), pp. 336–341.

Luchters, N. T. J., Fletcher, J.V., Roberts, S.J., Fletcher, J.C.Q. (2017) 'Variability of data in high throughput experimentation for catalyst studies in fuel processing', *Bulletin of Chemical Reaction Engineering and Catalysis*, 12(1), pp. 106–112.

Manukyan, K. V., Cross, A., Roslyakov, S., Rouvimov, S., Rogachev, A.S., Wolf, E.E., and Mukasyan, A.S. (2013) 'Solution Combustion Synthesis of Nano-Crystalline Metallic Materials: Mechanistic Studies', *The Journal of Physical Chemistry C*, 117(46), pp. 24417–24427.

Mazloomi, K. and Gomes, C. (2012) 'Hydrogen as an energy carrier : Prospects and challenges', *Renewable and Sustainable Energy Reviews*. Elsevier Ltd, 16(5), pp. 3024–3033.

McBride, J. R., Graham, G. W., Peters, C. R., and Weber, W. H. (1998) 'Growth and characterization of reactively sputtered thin-film platinum oxides', *Journal of Applied Physics*, 69(3), pp. 1596–1604.

Mei, Z., Li, Y., Fan, M., Zhao, L., and Zhao, J. (2015) 'Effect of the interactions between Pt species and ceria on Pt/ceria catalysts for water gas shift: The XPS studies', *Chemical Engineering Journal*. Elsevier B.V., 259, pp. 293–302.

Meira, D., Ribeiro, R., Mathon, O., Pascarelli, S., Bueno, J., and Zanchet, D. (2016) 'Complex interplay of structural and surface properties of ceria on platinum supported catalyst under water gas shift reaction', *Applied Catalysis B: Environmental*, 197, pp. 73–85.

Metson, J. B. (1999) 'Charge Compensation and Binding Energy Referencing in XPS Analysis', *Surface and Interface Analysis*, 27(July), pp. 1069–1072.

Micromeritics Instrument Corporation (2007) *TriStar 3000 Manual*.

Mokkelbost, T., Kaus, I., Grande, T. and Einarsrud, M. (2004) 'Combustion Synthesis and Characterization of Nanocrystalline CeO_2-Based Powders', *Chemistry of Materials*, 16, pp. 5489–5494.

Montini, T., Melchionna, M., Monai, M. and Fornasiero, P. (2016) 'Fundamentals and Catalytic Applications of CeO2-Based Materials', *Chemical Reviews*, 116(10), pp. 5987–6041.

Morfin, F., Nguyen, T., Rousset, J., and Piccollo, L. (2016) 'Synergy between hydrogen and ceria in Pt-catalyzed CO oxidation: An investigation on Pt/CeO_2 catalysts synthesized by solution combustion', *Applied Catalysis B: Environmental*. Elsevier B.V., 197, pp. 2–13.

Mukasyan, A.S. and Dinka, P. (2007) 'Novel approaches to solution-combustion synthesis of nanomaterials', *International Journal of Self-Propagating High-Temperature Synthesis*, 16(1), pp. 23–35.

Murugan, B., Ramaswamy, A. V., Srinivas, D., Gopinath, C. S., and Ramaswamy, V. (2008) 'Effect of fuel and its concentration on the nature of Mn in Mn/CeO_2 solid solutions prepared by solution combustion synthesis', *Acta Materialia*, 56(7), pp. 1461–1472.

Newsome, D. S. (1980) 'The water-gas shift reaction', *Catalysis Reviews Science and Engineering*, 21(2), pp. 275–318.

Nguyen, T. S., Morfin, F., Aouine, M., Bosselet, F., Rousset, J., and Piccolo, L. (2015) 'Trends in the CO oxidation and PROX performances of the platinum-group metals supported on ceria', *Catalysis Today*, 253, pp. 106–114.

Ogden, J. M. (1999) 'Prospects for Building a Hydrogen Energy Insfrastructure', *Annual Review of Energy and the Environment*, 24, pp. 227–279.

Panagiotopoulou, P., Papavasiliou, J., Avgouropoulos, G., Ioannides, T., and Kondarides, D.I. (2007) 'Water-gas shift activity of doped Pt/CeO_2 catalysts', *Chemical Engineering Journal*, 134(1–3), pp. 16–22.

Papastergiades, E., Argyropoulos, S., Rigakis, N., and Kiratzis, N.E. (2009) 'Fabrication of ceramic electrolytic films by the method of solution aerosol thermolysis (SAT) for solid oxide fuel cells (SOFC)', *Ionics*, 15(5), pp. 545–554.

Patil, K. C., Hedge, M.S., Rattan, T., and Aruna, S.T. (2008) *Chemistry of Nanocrystalline Oxide Materials Combustion Synthesis, Properties and Applications*. Singapore: World Scientific Publishing.

Pennycook, S. J. and Nellist, P. D. (eds) (2011) *Scanning Transmission Electron Microscopy: Imaging and Analysis*. Springer.

Pinna, F. (1998) 'Supported metal catalysts preparation', *Catal. Today*, 41(1–3), pp. 129–137.

Pino, L., Vita, A., Cordaro, M., Recupero, V., and Hedge, M.S. (2003) 'A comparative study of Pt/CeO_2 catalysts for catalytic partial oxidation of methane to syngas for application in fuel cell electric vehicles', *Applied Catalysis A: General*, 243(1), pp. 135–146.

Pino, L., Vita, A., Cipiti, F., Lagana, M., and Recupero, V. (2006) 'Performance of Pt/CeO_2 catalyst for propane oxidative steam reforming', *Applied Catalysis A: General*, 306, pp. 68–77.

Pokol, G., Leskelä, T. and Niinistö, L. (1994) 'Thermal behaviour of sulphato and nitrato complexes of cerium(IV)', *Journal of Thermal Analysis*, 42(2–3), pp. 343–359.

Purohit, R. D., Sharma, B.P., Pillai, K.T., and Tyagi, A.K. (2001) 'Ultrafine ceria powders via glycine-nitrate combustion', *Materials Research Bulletin*, 36(15), pp. 2711–2721.

Qi, A., Peppley, B. and Karan, K. (2007) 'Integrated fuel processors for fuel cell application : A review', *Fuel Processing Technology*, 88, pp. 3–22.

Radhakrishnan, R., Willigan, R.R., Dardas, X., and Vandersprut, T.H. (2006) 'Water Gas Shift Activity of noble Metals supported on Ceria-Zirconia Oxides', *AIChE Journal*, 56, pp. 1888–1894.

Rao, G. R., Mishra, B. G. and Sahu, H. R. (2004) 'Synthesis of CuO, Cu and CuNi alloy particles by solution combustion using carbohydrazide and N-tertiarybutoxy-carbonylpiperazine fuels', *Materials Letters*, 58(27–28), pp. 3523–3527.

Rasband, W. (2016) *ImageJ*, *National Institue of Mental Health*. Available at: https://imagej.nih.gov/ij/.

Regalbuto, J. (2006) *Catalyst Preparation: Science and Engineering By John R. Regalbuto*, *AIChE Journal*.

Ricote, S., Jacobs, G., Milling, M., Ji, Y., Patterson, P.M., Davis, B.H. (2006) 'Low temperature water – gas shift : Characterization and testing of binary mixed oxides of ceria and zirconia promoted with Pt', *Applied Catalysis A, General*, 303, pp. 35–47.

Roh, H. S., Potdar, H.S., Jeong, D.W., Kim, K.S., Shim, J.O., Jang, W.U., Koo, K.Y., and Yoon, W.L. (2012) 'Synthesis of highly active nano-sized (1 wt.% Pt/CeO_2) catalyst for water gas shift reaction in medium temperature application', *Catalysis Today*. Elsevier B.V., 185(1), pp. 113–118.

Scanlon, D. O., Morgan, B. J. and Watson, G. W. (2011) 'The origin of the enhanced oxygen storage capacity of Ce(1-x)(Pd/Pt)(x)O2.', *Physical chemistry chemical physics : PCCP*, 13(10), pp. 4279–4284.

Scherrer, P. (1912) 'Bestimmung der inneren Struktur und der Größe von Kolloidteilchen mittels Röntgenstrahlen', in *Kolloidchemie Ein Lehrbuch*. Berlin, Heidelberg.: Springer, pp. 387–409.

Semelsberger, T. A. and Borup, R. L. (2005) 'Fuel effects on start-up energy and efficiency for automotive PEM fuel cell systems', *International Journal of Hydrogen Energy*, 30(4), pp. 425–435.

Sepúlveda-Escribano, A., Coloma, F. and Rodríguez-Reinoso, F. (1998) 'Promoting effect of ceria on the gas phase hydrogenation of crotonaldehyde over platinum catalysts', *Journal of Catalysis*, 178(2), pp. 649–657.

Shekhawat, D., Spivey, J. J. and Berry, D. (2011) *Fuel Cells: Technologies for Fuel Processing*. Spain: Elsevier.

Shih, S. J. and Huang, J. P. (2013) 'Designing the morphology of ceria particles by precursor complexes', *Ceramics International*. Elsevier, 39, pp. 2275–2281.

Shirley, D. A. (1972) 'High-resolution x-ray photoemission spectrum of the valence bands of gold', *Physical Review B*, 5(12), pp. 4709–4714.

Shiryaev, A. (1995) 'Thermodynamics of SHS processes: An advanced approach', *International Journal of Self-Propagating High-Temperature Synthesis*, 4, pp. 351–362.

Sing, K. S. W. (1982) 'Reporting physisorption data for gas/solid systems with special reference to the determination of surface area and porosity (Provisional)', *Pure and Applied Chemistry*, 54(11).

Smith R J, B., Loganathan, M. and Shantha, M. S. (2010) 'A Review of the Water Gas Shift Reaction Kinetics', *International Journal of Chemical Reactor Engineering*, 8(1).

Specchia, S. (2011) 'Hydrocarbons valorisation to cleaner fuels: H2-rich gas production via fuel processors', *Catalysis Today*, 176(1), pp. 191–196.

Specchia, S., Ercolini, G., karimi, S., Italiano, C., and Vita, A. (2017) 'Solution combustion synthesis for preparation of structured catalysts: A mini-review on process intensification for energy applications and pollution control', *International Journal of Self-Propagating High-Temperature Synthesis*, 26(3), pp. 166–186.

Ssekimpi, K. (2018) *Determination of Pt Particle Size Distribution of TEM Images*. University of Cape Town.

Strydom, C. A. and Vuuren, C. P. J. Van (1987) 'The Thermal Decomposition Of Cerium (III) Nitrate', *Journal of Thermal Analysis*, 32, pp. 157–160.

Thommes, M., Kaneko, K., Neimark, A.V., Oliver, J.P., Rodriguez-Reinoso, F., Rouquerol, J. and Sing, K.S.W. (2015) 'Physisorption of gases, with special reference to the evaluation of surface area and pore size distribution (IUPAC Technical Report)', *Pure and Applied Chemistry*, 87(9–10), pp. 1051–1069.

Tougaard, S. (1988) 'Quantitative analysis of the inelastic background in surface electron spectroscopy', *Surface and Interface Analysis*, 11(9), pp. 453–472.

Trovarelli, A., Boaro, M. Rocchini, E., de Leitenburg, C. and Dolcetti, G. (2001) 'Some recent developments in the characterization of ceria-based catalysts', *Journal of Alloys and Compounds*, 323–324, pp. 584–591.

Twigg, M. V. (1989) *Catalyst Handbook*. 2nd edn. England: Wolfe Publishing Ltd.

United Nations (2015) *Paris Agreement*. Available at: https://unfccc.int/process-and-meetings/the-paris-agreement/the-paris-agreement (Accessed: 16 October 2018).

Varma, A., Rogachev, A.S., Mukasyan, A.S., and Hwang, S. (1998) 'Combustion synthesis of advanced materials: Principles and applications', in *Advances in Chemical Engineering*. Academic Press, pp. 79–226.

Varma, A., Mukasyan, A.S., Rogachev, A.S., and Manukyan, K.V. (2016) 'Solution Combustion Synthesis of Nanoscale Materials', *Chemical Reviews*, 116, pp. 14493–14586.

Vita, A., Cristiano, G., Italion, C., Specchia, S., Cipiti, F. and Specchia, V. (2014) 'Methane oxy-steam reforming reaction performances of Ru/Al_2O_3 catalysts loaded on structured cordierite monoliths', *International Journal of Hydrogen Energy*, 39, pp. 18592–18603.

Vita, A., Italiano, C., Fabiano, C., Lagana, M. and Pino, L. (2015a) 'Influence of Ce-precursor and fuel on structure and catalytic activity of combustion synthesized Ni/CeO2 catalysts for biogas oxidative steam reforming', *Materials Chemistry and Physics*, 163, pp. 337–347.

Vita, A., Cristiano, G., Italiano, C., Pino, L. and Specchia, S. (2015a) 'Syngas production by methan oxy-steam reforming on Me/CeO_2 (Me = Rh, Pt, Ni) catalyst lined on cordierite monoliths, *Applied Catalysis B, Environmental*, 162, pp. 551–563.

Vita, A., Italiano, C., Fabiano, C., Pino, L., Lagana, M., and Recupero, V. (2016) 'Hydrogen-rich gas production by steam reforming of n-dodecane: Part I: Catalytic activity of Pt/CeO_2 catalysts in optimized bed configuration', *Applied Catalysis B: Environmental*. Elsevier B.V., 199, pp. 350–360.

Wagner, C. D., Riggs, W.M., Davis, L.E., Moulder, J.F., and Muilenberg, G.E. (1979) *Handbook of X-Ray Photoelectron Spectroscopy*, *Perkin-Elmer Corporation*. Perkin-Elmer Corporation.

Webb, P. A. and Orr, C. (1997) 'Analytical methods in fine particle technology', *Micromeritics Instrument Corp*.

Wen, W. and Wu, J. (2014) 'Nanomaterials via solution combustion synthesis: a step nearer to controllability', *RSC Adv.* Royal Society of Chemistry, 4(101), pp. 58090–58100.

Wendlandt, W. W. (1956) 'The thermolysis of the rare earth and other metal nitrates', *Analytica Chimica Acta*, 15, pp. 435–439.

Williams, D. and Carter, C. (2009) *Transmission Electron Microscopy*. Springer.

Xu, W., Si, R., Senanayake, S.D., Lloraca, J., Idriss, H., Stacchiola, D., Hanson, J.C., and Rodriguez, J.A. (2012) 'In situ studies of CeO_2-supported Pt, Ru, and Pt-Ru alloy catalysts for the water-gas shift reaction: Active phases and reaction intermediates', *Journal of Catalysis*, 291, pp. 117–126.

Yablokov, V. Y., Smel'tsova, I.L., Zelyaev, I.A., Mitrofanova, S.V. (2009) 'Studies of the rates of thermal decomposition of glycine, alanine, and serine', *Russian Journal of General Chemistry*, 79(8), pp. 1704–1706.

Yahiro, H., Murawaki, K., Saiki, K., Yamamoto, T., and Yamaura, H. (2007) 'Study on the supported Cu-based catalysts for the low-temperature water–gas shift reaction', *Catalysis Today*, 126, pp. 436–440.

Yu, T., Joo, J., Park, Y., and Hyeon, T. (2005) 'Large-scale nonhydrolytic sol-gel synthesis of uniform-sized ceria nanocrystals with spherical, wire, and tadpole shapes', *Angewandte Chemie - International Edition*, 44(45), pp. 7411–7414.

Zalc, J. M. and Loffler, D. G. (2002) 'Fuel processing for PEM fuel cells: transport and kinetic issues of system design', *Journal of Pow*, 111(1), pp. 58–64.

Zhang, J., Kang, Z. C. and Eyring, L. (1993) 'The binary higher oxides of rate earths', *Journal of Alloys and Compounds*, 192(1–2), pp. 57–63.

Zhou, Q., Mou, Y., Ma, X., Xue, L., and Yan, Y. (2014) 'Effect of fuel-to-oxidizer ratios on combustion mode and microstructure of Li_2TiO_3 nanoscale powders', *Journal of the European Ceramic Society*. Elsevier Ltd, 34(3), pp. 801–807.

Zhuravlev, V. D., Bamburov, V.G., Bekerov, A.R., Perlyaeva, L.A., Baklanova, I.V., Sivtsova, O.V., Vasil'ev, V.G., Vladimirova, E.V., Shevchenko, V.G., and Grigorov, I.G. (2013) 'Solution combustion synthesis of α-Al_2O_3 using urea', *Ceramics International*, 39(2), pp. 1379–1384.

Appendix A: Summary of the Synthesis Redox Reactions

This appendix provides supporting information for chapter 2.4.

A.1. Redox Reactions

A.1.1. Synthesis of CeO_2 (SCS, CN+GLC) supports:

$$Ce(NO_3)_3.6H_2O \rightarrow CeO_2 + \frac{3}{2}N_2 + \frac{7}{2}O_2 + 6H_2O \quad \text{Equation 8.1}$$

$$nC_2H_5NO_2 + \frac{9}{4}nO_2 \rightarrow 2nCO_2 + \frac{1}{2}nN_2 + \frac{5}{2}nH_2O \quad \text{Equation 8.2}$$

$$Ce(NO_3)_3 + nC_2H_5NO_2 + \frac{7}{2}\left(\frac{9}{14}n - 1\right)O_2 \rightarrow CeO_2 + 2nCO_2 + \left(\frac{3}{2} + \frac{1}{2}n\right)N_2 + \frac{5}{2}nH_2O \quad \text{Equation 8.3}$$

$$\varphi = \frac{9}{14}n \quad \text{Equation 8.4}$$

$$Ce(NO_3)_3 + \frac{14}{9}\varphi C_2H_5NO_2 + \frac{7}{2}(\varphi - 1)O_2 \rightarrow CeO_2 + \frac{28}{9}\varphi CO_2 + \left(\frac{3}{2} + \frac{7}{9}\varphi\right)N_2 + \frac{35}{9}\varphi H_2O \quad \text{Equation 8.5}$$

A.1.2. Synthesis of CeO_2 (SCS, CAN+GLC) supports:

$$(NH_4)_2Ce(NO_3)_6 \rightarrow CeO_2 + 4N_2 + 4H_2O + 6O_2 \quad \text{Equation 8.6}$$

$$nC_2H_5NO_2 + \frac{9}{4}nO_2 \rightarrow 2nCO_2 + \frac{1}{2}nN_2 + \frac{5}{2}nH_2O \quad \text{Equation 8.7}$$

$$(NH_4)_2Ce(NO_3)_6 + nC_2H_5NO_2 + 6\left[\frac{3}{8}n - 1\right]O_2 \rightarrow CeO_2 + 2nCO_2 + \left[\frac{1}{2}n + 4\right]N_2 + \left[\frac{5}{2}n + 4\right]H_2O \quad \text{Equation 8.8}$$

$$\varphi = \frac{3}{8}n \quad \text{Equation 8.9}$$

$$(NH_4)_2Ce(NO_3)_6 + \frac{8}{3}\varphi C_2H_5NO_2 + 6[\varphi - 1]O_2 \rightarrow CeO_2 + \frac{16}{3}\varphi CO_2 + \left[\frac{4}{3}\varphi + 4\right]N_2 + \left[\frac{20}{3}\varphi + 4\right]H_2O \quad \text{Equation 8.10}$$

A.1.3. Synthesis of SCS (CN+GLC) catalysts:

$$Ce(NO_3)_3.6H_2O \rightarrow CeO_2 + \frac{3}{2}N_2 + \frac{7}{2}O_2 + 6H_2O$$ Equation 8.11

$$nC_2H_5NO_2 + \frac{9}{4}nO_2 \rightarrow 2nCO_2 + \frac{1}{2}nN_2 + \frac{5}{2}nH_2O$$ Equation 8.12

$$x(NH_3)_4\,Pt(NO_3)_2 + xO_2 \rightarrow xPtO_2 + 3xN_2 + 6xH_2O$$ Equation 8.13

$$\begin{aligned} Ce(NO_3)_3 + \; x(NH_3)_4\,Pt(NO_3)_2 + nC_2H_5NO_2 + \frac{7}{2}\left(\frac{9n+4x}{14} - 1\right)O_2 \\ \rightarrow xPtO_2 + \; CeO_2 + 2nCO_2 + \left(\frac{3}{2} + \frac{1}{2}n + 3x\right)N_2 \\ + \; \left(\frac{5}{2}n + 6x\right)H_2O \end{aligned}$$ Equation 8.14

$$\varphi = \frac{9n+4x}{14}$$ Equation 8.15

For SCS catalysts using the cerium (III) nitrate hexahydrate (CN) precursor:

$$m[CeO_2] = 1\,mol \times 172.14\frac{g}{mol} = 172.14\,g$$

$$m[Pt] = 1\% \times 172.14\,g = 1.7214\,g$$

$$n[Pt] = \frac{1.7214\,g}{195.084\,g/mol} = 0.0088\,mol$$

$$n[Pt] = n[(NH_3)_4\,Pt(NO_3)_2] = 0.0088\,mol$$

$$\therefore x = 0.0088\,mol$$

$$\therefore \varphi = \frac{9n + 0.0353}{14} \rightarrow n = \frac{14\varphi - 0.0353}{9}$$

$$\begin{aligned} Ce(NO_3)_3.6H_2O + \; x(NH_3)_4\,Pt(NO_3)_2 + \left(\frac{14\varphi - 0.0353}{9}\right)C_2H_5NO_2 \\ + \frac{7}{2}(\varphi - 1)O_2 \\ \rightarrow 0.0088PtO_2 + \; CeO_2 + \left(\frac{28\varphi - 0.0706}{9}\right)CO_2 \\ + \left(\frac{3}{2} + \frac{14\varphi - 0.0353}{18} + 3x\right)N_2 \\ + \; \left(\frac{5}{2}\left(\frac{14\varphi - 0.0353}{9}\right) + 6.2118\right)H_2O \end{aligned}$$ Equation 8.16

A.1.4. Synthesis of SCS (CAN+GLC) catalysts:

$$(NH_4)_2Ce(NO_3)_6 \rightarrow CeO_2 + 4N_2 + 4H_2O + 6O_2$$ Equation 8.17

$$nC_2H_5NO_2 + \frac{9}{4}nO_2 \rightarrow 2nCO_2 + \frac{1}{2}nN_2 + \frac{5}{2}nH_2O$$ Equation 8.18

$$x(NH_3)_4\,Pt(NO_3)_2 + xO_2 \rightarrow xPtO_2 + 3xN_2 + 6xH_2O$$ Equation 8.19

$$\begin{aligned}(NH_4)_2Ce(NO_3)_6 + x(NH_3)_4\,Pt(NO_3)_2 + nC_2H_5NO_2 + 6\left(\frac{9n+4x}{24} - 1\right)O_2 \\ \rightarrow xPtO_2 + CeO_2 + 2nCO_2 + \left(\frac{1}{2}n + 4 + 3x\right)N_2 \\ + \left(\frac{5}{2}n + 4 + 6x\right)H_2O\end{aligned}$$ Equation 8.20

$$\varphi = \frac{9n + 4x}{24}$$ Equation 8.21

For 1wt.% Pt/CeO_2 using the cerium (IV) ammonium nitrate (CAN) precursor:

$$m[CeO_2] = 1\,mol \times 172.14\frac{g}{mol} = 172.14\,g$$

$$m[Pt] = 1\% \times 172.14\,g = 1.7214\,g$$

$$n[Pt] = \frac{1.7214\,g}{195.084\,g/mol} = 0.0088\,mol$$

$$n[Pt] = n[(NH_3)_4\,Pt(NO_3)_2] = 0.0088\,mol$$

$$\therefore x = 0.0088\,mol$$

$$\therefore \varphi = \frac{9n + 0.0353}{24} \rightarrow n = \frac{24\varphi - 0.0353}{9}$$

$$\begin{aligned}(NH_4)_2Ce(NO_3)_6 + 0.0088\,(NH_3)_4\,Pt(NO_3)_2 + nC_2H_5NO_2 + 6(\varphi - 1)O_2 \\ \rightarrow 0.0088PtO_2 + CeO_2 + \left(\frac{48\varphi - 0.0706}{9}\right)CO_2 \\ + \left(4.1.059 + \frac{24\varphi - 0.0353}{18}\right)N_2 \\ + \left(4.2118 + \frac{5}{2}\left(\frac{24\varphi - 0.0353}{9}\right)\right)H_2O\end{aligned}$$ Equation 8.22

A.2 Chemicals Used

Table 8.1 tabulates the Ce-precursors, fuel and Pt-salt used within the two synthesis approaches and the details regarding the suppliers.

Table 8.1: Chemicals used

Cerium (III) nitrate hexahydrate (CN), $Ce(NO_3)_3.6H_2O$	Sigma Aldrich 99.99% trace metals basis, Lot no.: MKCB3831
Cerium (IV) ammonium nitrate (CAN), $(NH_4)_2Ce(NO_3)_6$	Alfa Aesar, 99.95%, Lot no.: U19A045
Glycine (GLC), $C_2H_5NO_2$	Sigma Aldrich ≥ 99% for electrophoresis, Lot no.: SZBG0470V
Tetra-ammine platinum (II) nitrate, $Pt(NH_3)_4(NO_3)_2$	Sigma Aldrich ≥ 50% Pt basis, Lot no.: MKCC6718

Appendix B: Stainless-steel Mesh Cage Design

This appendix provides supporting information for chapter 0.

A stainless-steel mesh cage was designed and made by Trust Engineering to use for the SCS reactions. The cage consists of a stainless-steel 304 frame with a ceramic fibre board bottom and lid. The sides of the cage are made of a 50 μm stainless-steel mesh. The ceramic crucible is place inside the cage, and the entire cage is placed in the furnace. This allows for any fine powder product that forms to be captured within the cage.

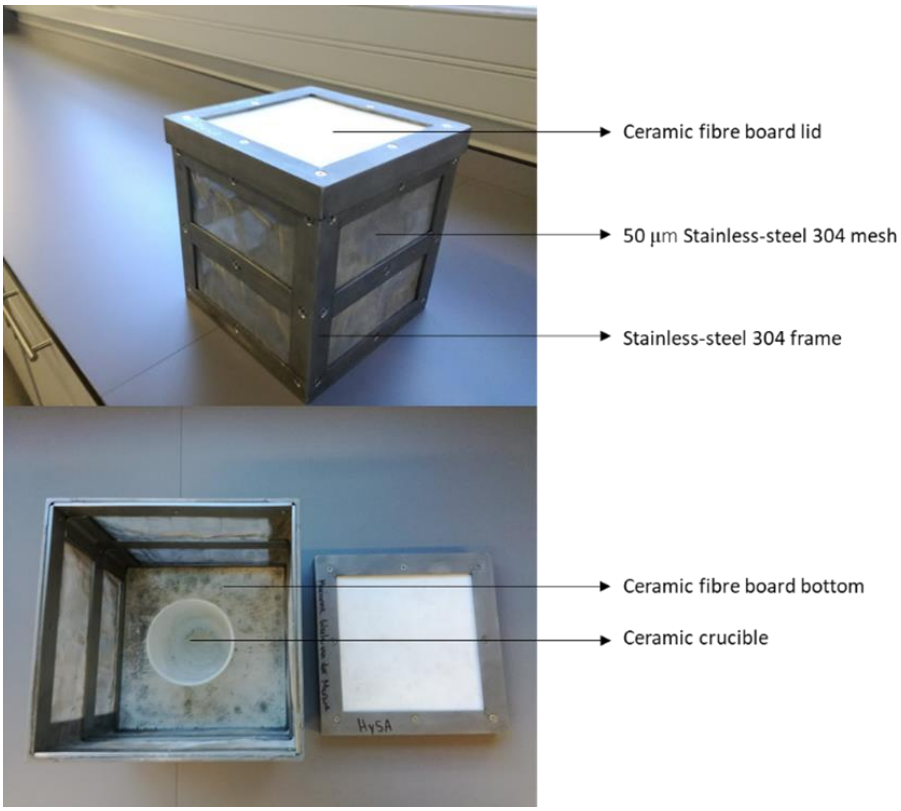

Figure 8.1: Stainless-steel Mesh Cage

Appendix C: Summary of the Characterizations

This appendix provides supporting information for chapters 4 and 5.

C.1. X-Ray Diffractograms

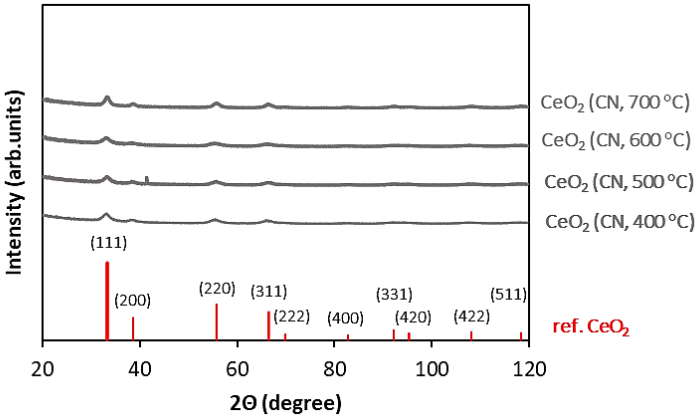

Figure 8.2: XRD diffraction patterns of CeO_2 (SCS) powders synthesized using cerium nitrate hexahydrate (CN) and a fuel-oxidant ratio = 0.50 with varying furnace temperatures (400 °C, 500 °C, 600 °C, 700 °C) with the referenced pattern for cubic CeO_2 (JCPDS01-081-0792).

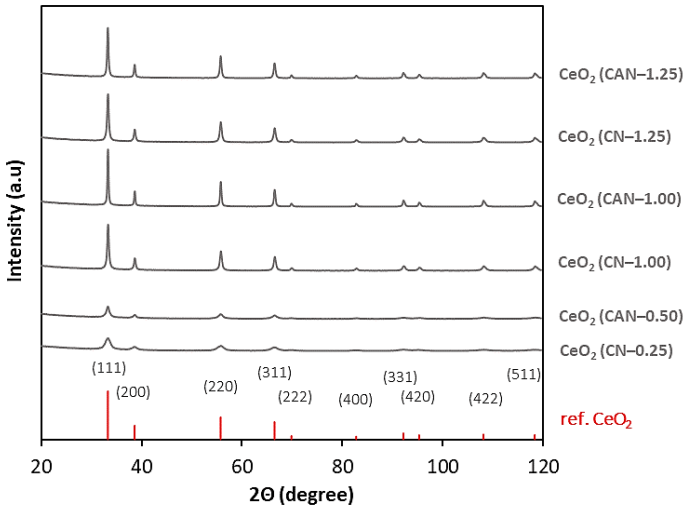

Figure 8.3: XRD diffraction patterns of CeO_2 (SCS) powders synthesized using cerium nitrate hexahydrate (CN) and cerium (IV) ammonium nitrate (CAN) and varying fuel-oxidant ratios (φ = 0.50, 1.00, 1.25) with the referenced pattern for cubic CeO_2 (JCPDS01-081-0792).

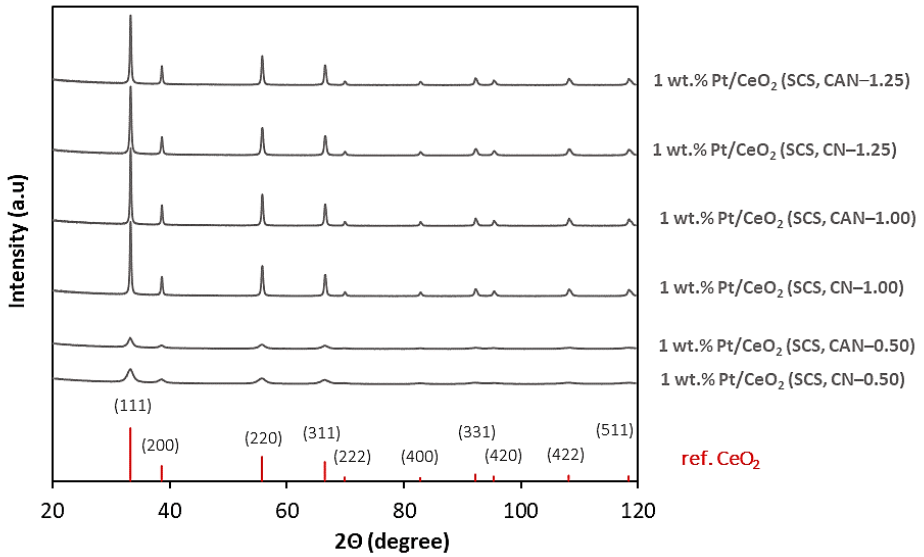

Figure 8.4: XRD diffraction patterns of 1 wt.% Pt/CeO_2 (SCS) powders synthesized using cerium nitrate hexahydrate (CN) and cerium (IV) ammonium nitrate (CAN) and varying fuel-oxidant ratios (φ = 0.50, 1.00, 1.25) with the referenced pattern for cubic CeO_2 (JCPDS01-081-0792).

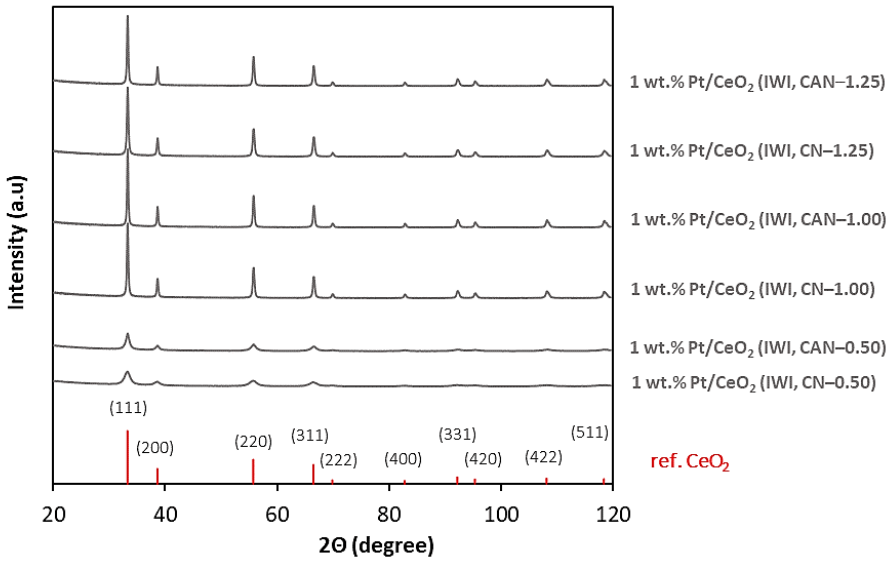

Figure 8.5: XRD diffraction patterns of 1 wt.% Pt/CeO_2 (IWI) powders with the referenced pattern for cubic CeO_2 (JCPDS01-081-0792).

C.2. N_2-physisorption

C.2.1. N_2 adsorption-desorption isotherms

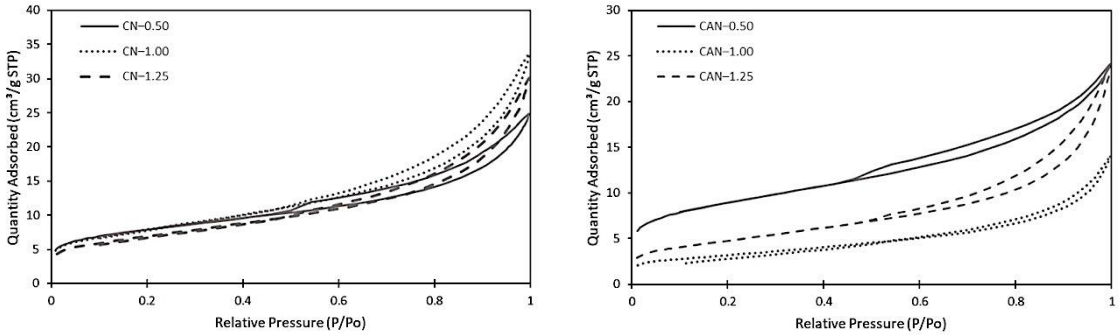

Figure 8.6: N_2-physisorption isotherms of the set of CeO_2 supports synthesized using cerium nitrate hexahydrate (CN) and cerium (IV) ammonium nitrate (CAN) and varying fuel-oxidant ratios (φ = 0.5, 1, 1.25).

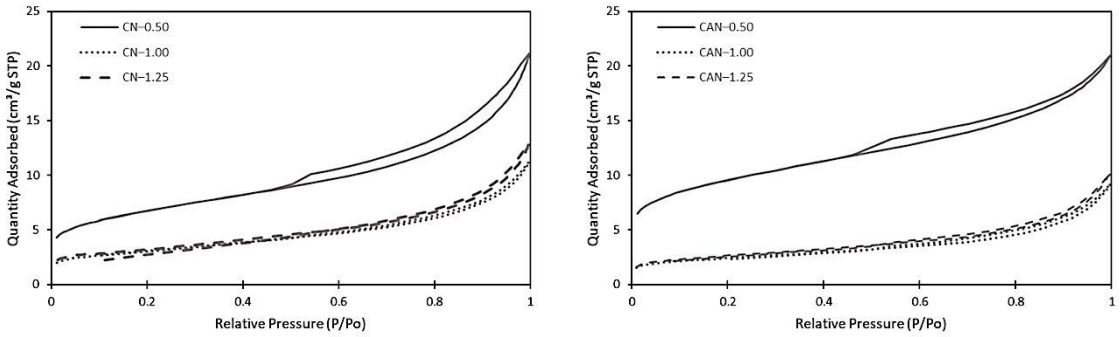

Figure 8.7: N_2-physisorption isotherms of the set of SCS catalysts synthesized using cerium nitrate hexahydrate (CN) and cerium (IV) ammonium nitrate (CAN) and varying fuel-oxidant ratios (φ = 0.5, 1, 1.25).

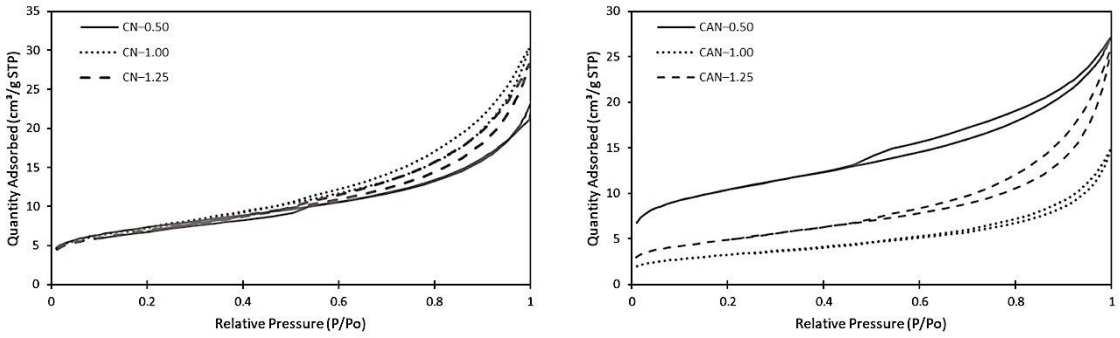

Figure 8.8: N_2-physisorption isotherms of the set of IWI catalysts synthesized using the set of CeO_2 supports synthesized using cerium nitrate hexahydrate (CN) and cerium (IV) ammonium nitrate (CAN) and varying fuel-oxidant ratios (φ = 0.5, 1, 1.25).

C.2.2. Linearized BET fitted isotherms

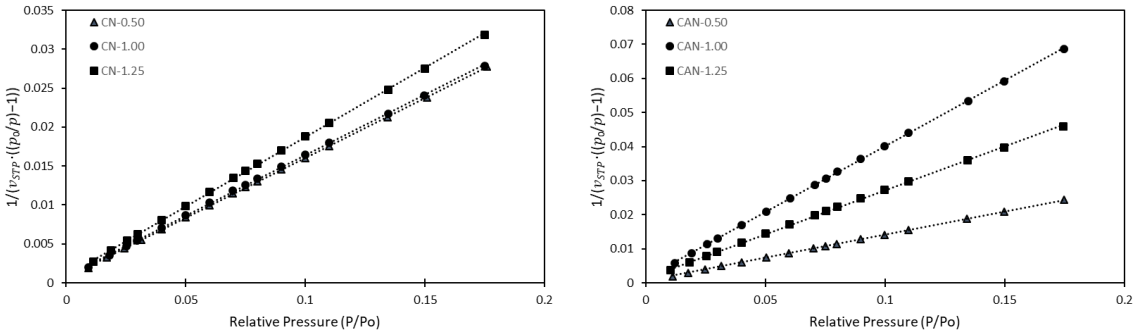

Figure 8.9: Linearized BET fitted isotherms of CeO_2 supports synthesized using cerium nitrate hexahydrate (CN) and cerium (IV) ammonium nitrate (CAN) and varying fuel-oxidant ratios (φ = 0.5, 1, 1.25).

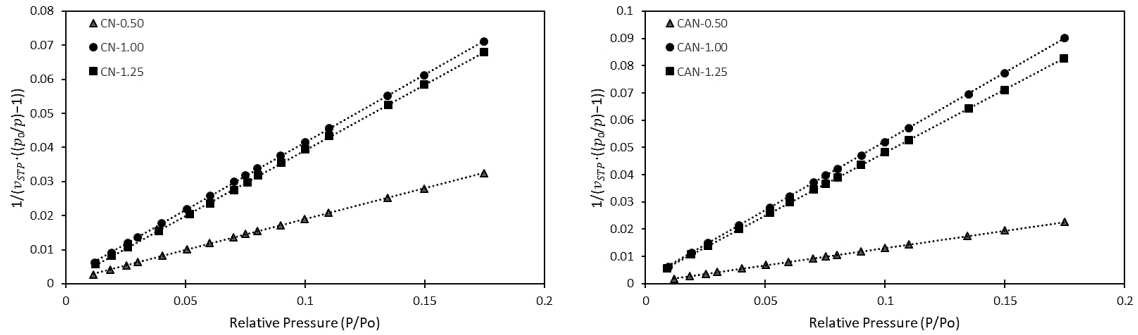

Figure 8.10: Linearized BET fitted isotherms of SCS catalysts synthesized using cerium nitrate hexahydrate (CN) and cerium (IV) ammonium nitrate (CAN) and varying fuel-oxidant ratios (φ = 0.5, 1, 1.25).

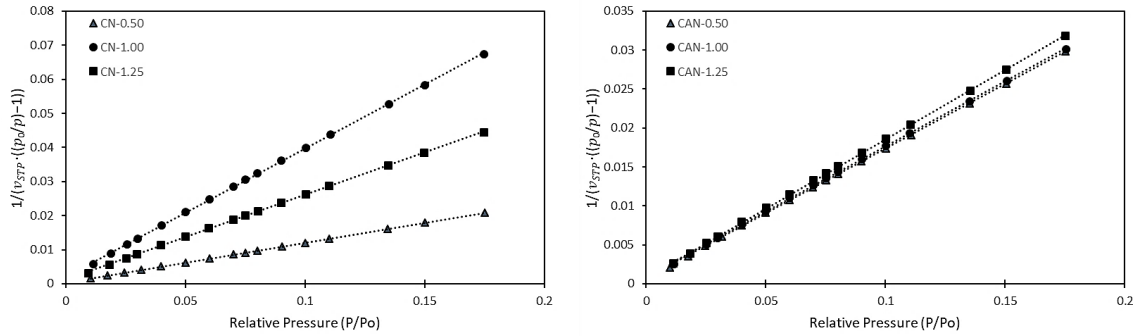

Figure 8.11: Linearized BET fitted isotherms of IWI catalysts synthesized using cerium nitrate hexahydrate (CN) and cerium (IV) ammonium nitrate (CAN) and varying fuel-oxidant ratios (φ = 0.5, 1, 1.25).

Table 8.2: Fitted BET "c" constant

Catalyst	**R^2 value**	**c constant**
CeO_2 (CN+GLC, 0.5)	0.99	223
CeO_2 (CN+GLC, 1)	0.99	188
CeO_2 (CN+GLC, 1.25)	0.99	193
CeO_2 (CAN+GLC, 0.5)	0.99	247
CeO_2 (CAN+GLC, 1)	0.99	268
CeO_2 (CAN+GLC, 1.25)	0.99	177
SCS (CN+GLC, 0.5)	0.99	202
SCS (CN+GLC, 1)	0.99	232
SCS (CN+GLC, 1.25)	0.99	578*
SCS (CAN+GLC, 0.5)	0.99	291
SCS (CAN+GLC, 1)	0.99	312*
SCS (CAN+GLC, 1.25)	0.99	235
IWI (CN+GLC, 0.5)	0.99	290
IWI (CN+GLC, 1)	0.99	187
IWI (CN+GLC, 1.25)	0.99	199
IWI (CAN+GLC, 0.5)	0.99	290
IWI (CAN+GLC, 1)	0.99	187
IWI (CAN+GLC, 1.25)	0.99	199

*these constants were outside of the required range for c, however changing the relative pressure range used for the fittings to reduce the value of the c constant did not significantly change the BET surface area.

C.3 Transmission Electron Microscopy Images

C.3.1.1. Background theory of TEM

Transmission Electron Microscopy (TEM) is a valuable characterization technique as it provides highly magnified images which provides information such as the shape and size distribution of any nanosized particles (Fultz and Howe, 2008; Williams and Carter, 2009; Pennycook and Nellist, 2011). This technique is based on combining electrons using an electromagnetic objective lens to obtain an image on a phosphorescent plate which glows when hit by electrons. Electrons are emitted from a field emission gun (FEG) which are focussed using several electromagnetic lenses onto the sample. Two types of electron signals are generated upon the incidence of the electron beam with the sample: (1) a primary signal due to unscattered (also called forward-scattered) electrons which pass through the sample, and (2) a secondary signal of scattered electrons due to the interaction of the electrons with the sample. Two different images can be formed by adjusting the position of the objective aperture to either the primary signal (which is called a Bright Field (BF) image), or to the secondary signal of electrons (which is called a dark field image). In both images, the difference in density of the sample provides contrast to the image. In the BF images, the darker areas represent the denser material whereas in the dark field images it is the lighter areas. A Scanning TEM (STEM) is necessary for the detection of the scattered electrons. The dark field image formed using this technique offers better structural resolution in comparison to BF images. This is because the annular darkfield detector's inner angle is large enough to allow for the collection of non-Bragg scattered electrons. These electrons have passed close to the atomic nuclei and are elastically scattered. The image formed from these elastically scattered electrons provides between resolution between materials with similar densities, which is required in this study due to the similarity in the atomic masses of Pt (195.084 u) and Ce (140.116 u).

C.3.1.2. Bright-field and HAADF Images

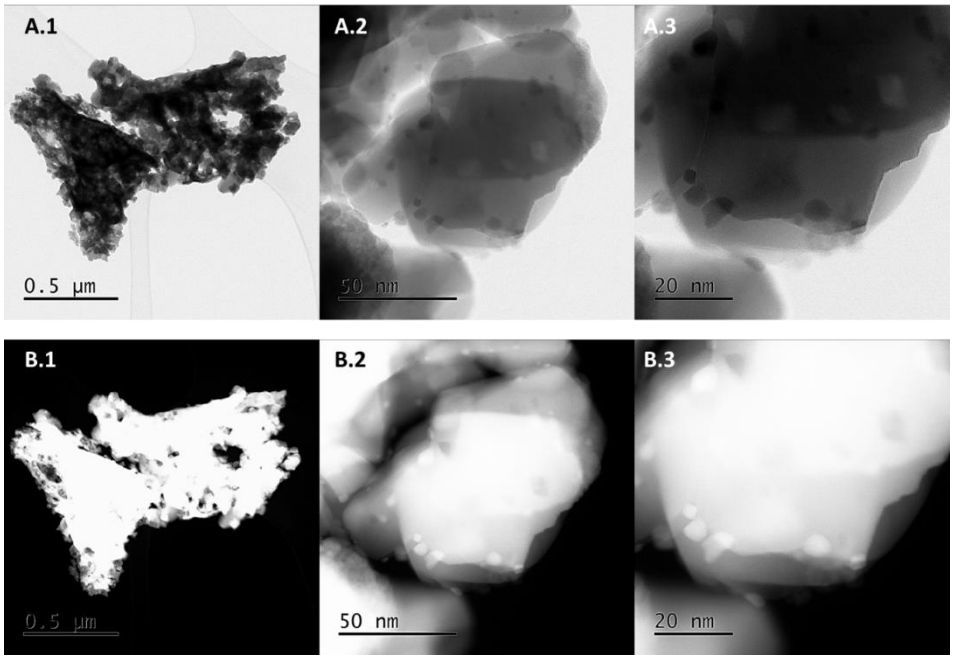

Figure 8.12: (A) Bright field TEM images and corresponding (B) HAADF images of the SCS (CAN+GLC, 0.5) catalyst.

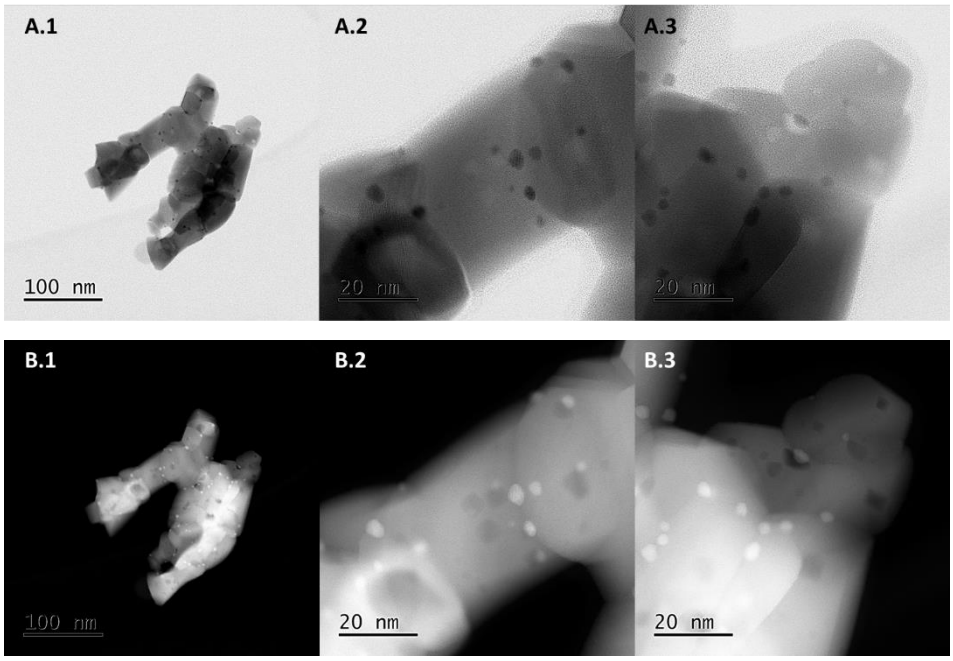

Figure 8.13: (A) Bright field TEM images and corresponding (B) HAADF images of the SCS (CAN+GLC, 1) catalyst.

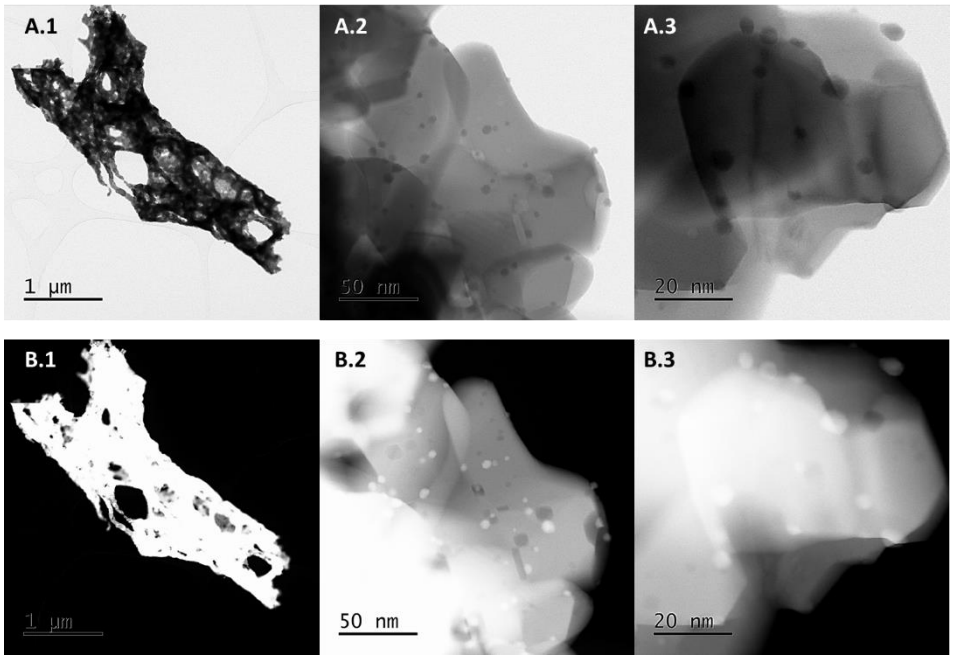

Figure 8.14: (A) Bright field TEM images and corresponding (B) HAADF images of the SCS (CAN+GLC, 1.25) catalyst.

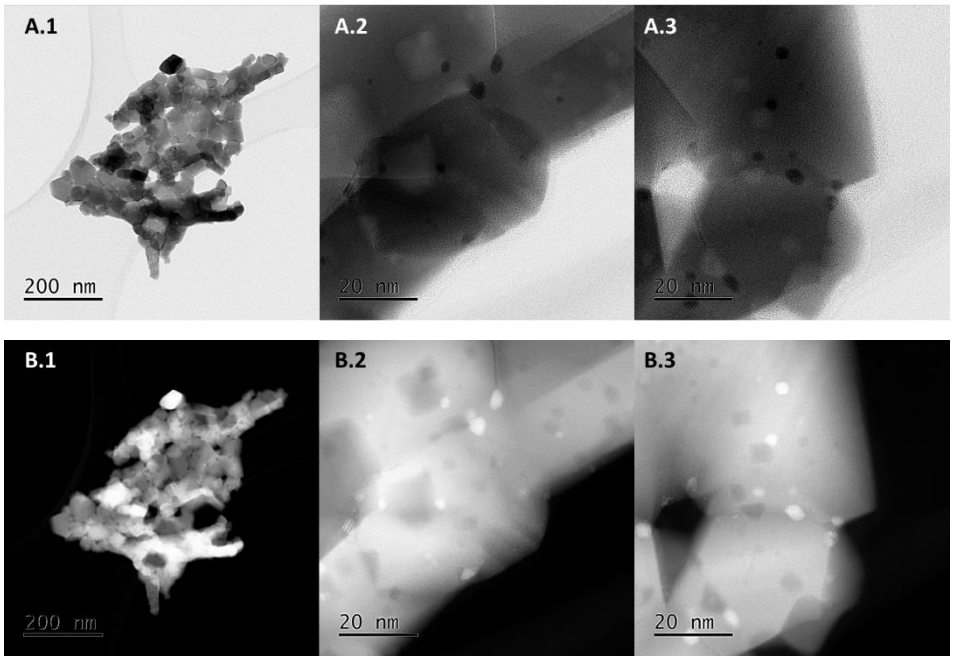

Figure 8.15: (A) Bright field TEM images and corresponding (B) HAADF images of 1.0 wt.% Pt/CeO_2 (SCS, CN–0.50) catalyst.

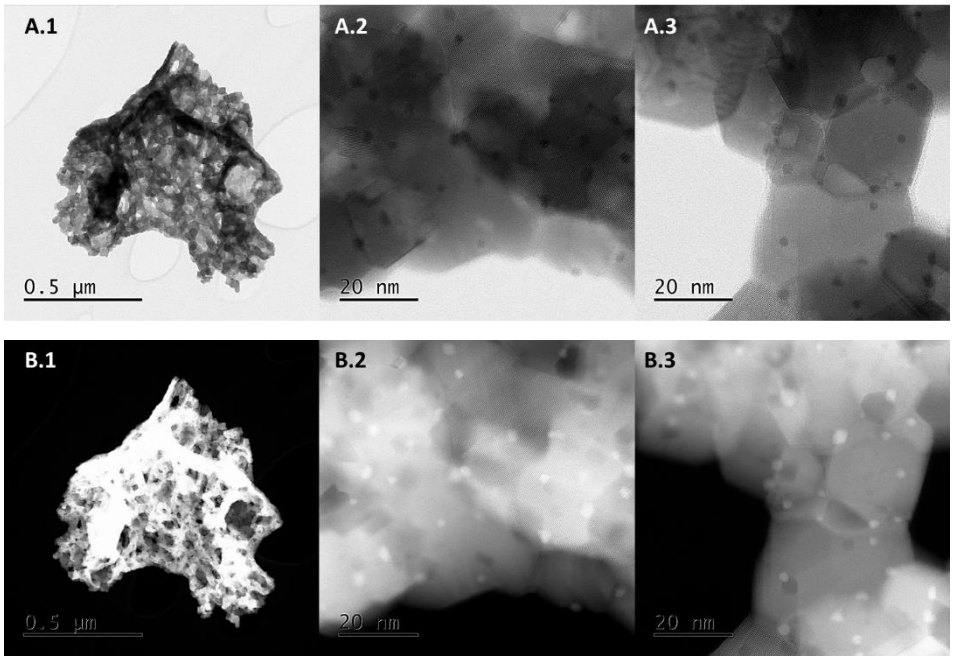

Figure 8.16: (A) Bright field TEM images and corresponding (B) HAADF images of 1.0 wt.% Pt/CeO_2 (SCS, CN–1.00) catalyst.

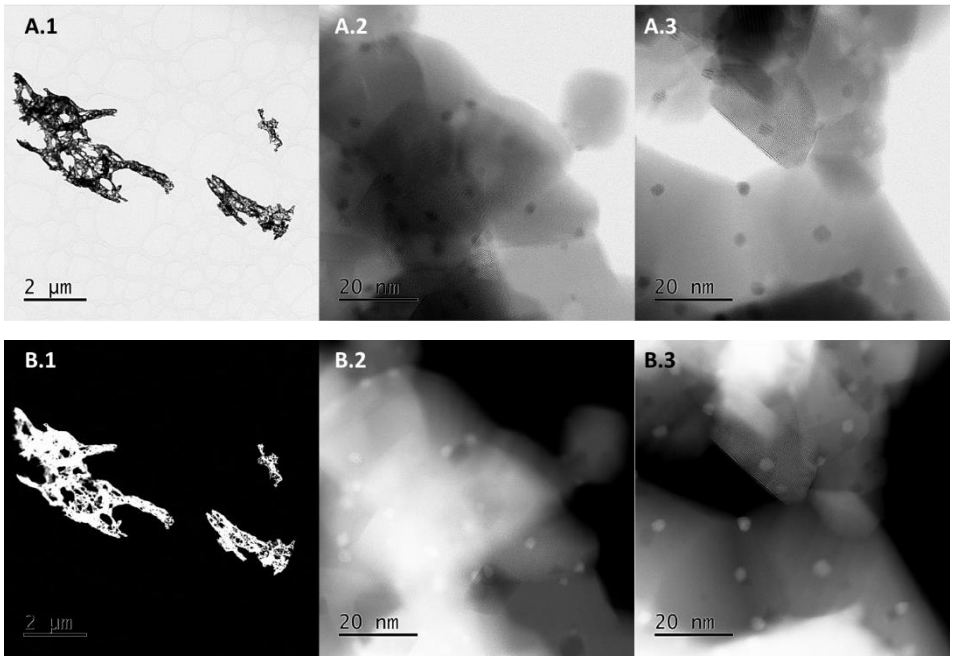

Figure 8.17: (A) Bright field TEM images and corresponding (B) HAADF images of 1.0 wt.% Pt/CeO_2 (SCS, CN–1.25) catalyst.

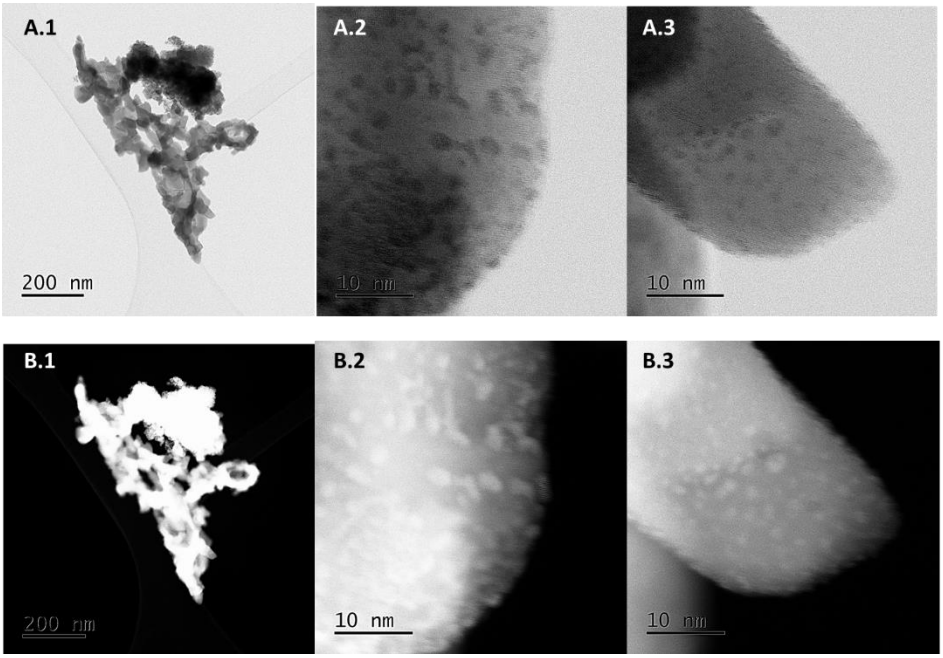

Figure 8.18: (A) Bright field TEM images and corresponding (B) HAADF images of 1.0 wt.% Pt/CeO_2 (IWI, CN–0.50) catalyst.

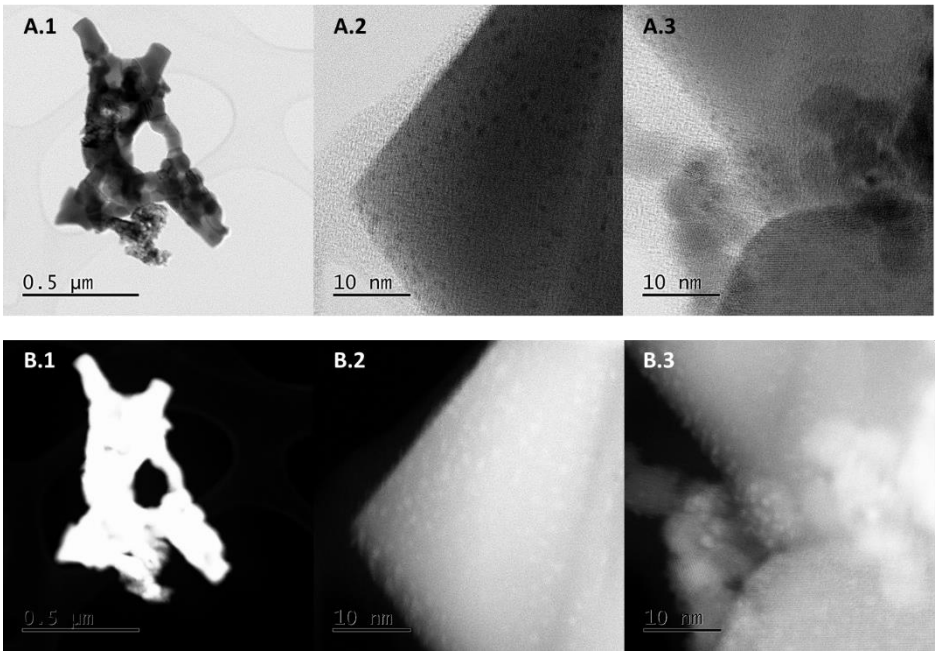

Figure 8.19: (A) Bright field TEM images and corresponding (B) HAADF images of 1.0 wt.% Pt/CeO_2 (IWI, CN–1.00) catalyst.

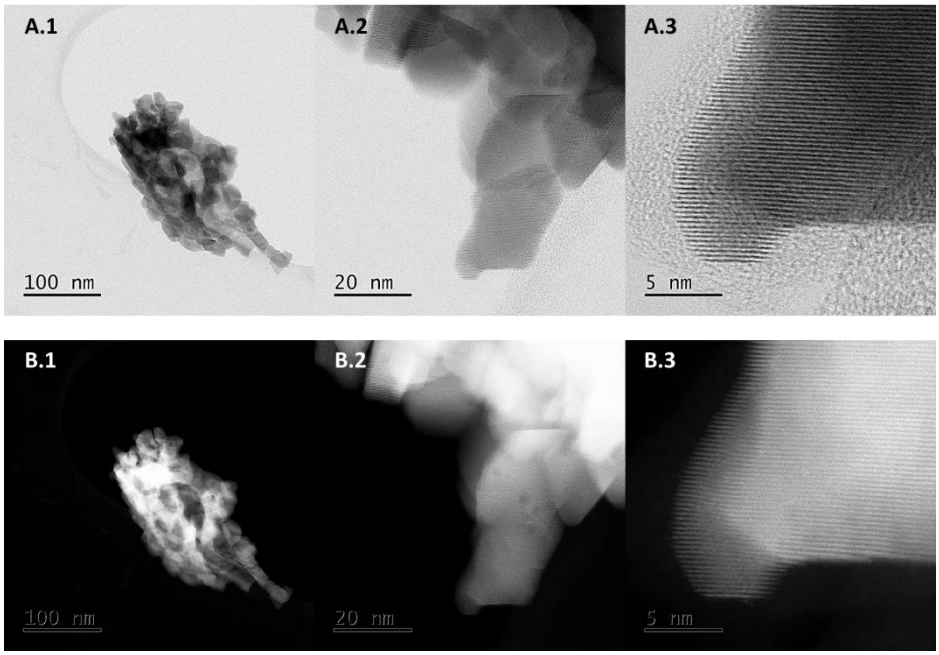

Figure 8.20: (A) Bright field TEM images and corresponding (B) HAADF images of 1.0 wt.% Pt/CeO_2 (IWI, CN–1.25) catalyst.

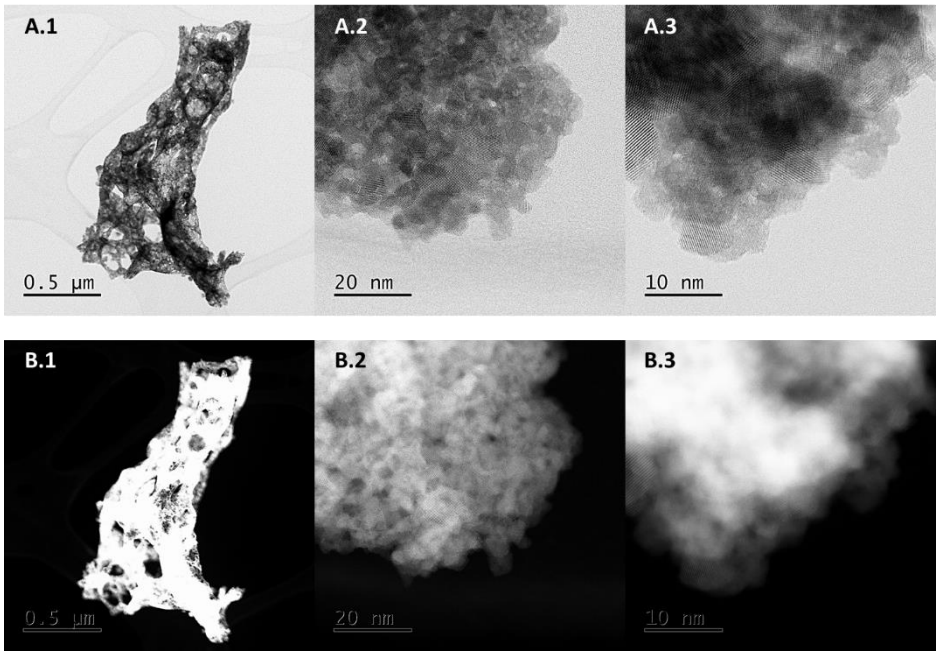

Figure 8.21: (A) Bright field TEM images and corresponding (B) HAADF images of 1.0 wt.% Pt/CeO_2 (IWI, CAN–0.50) catalyst.

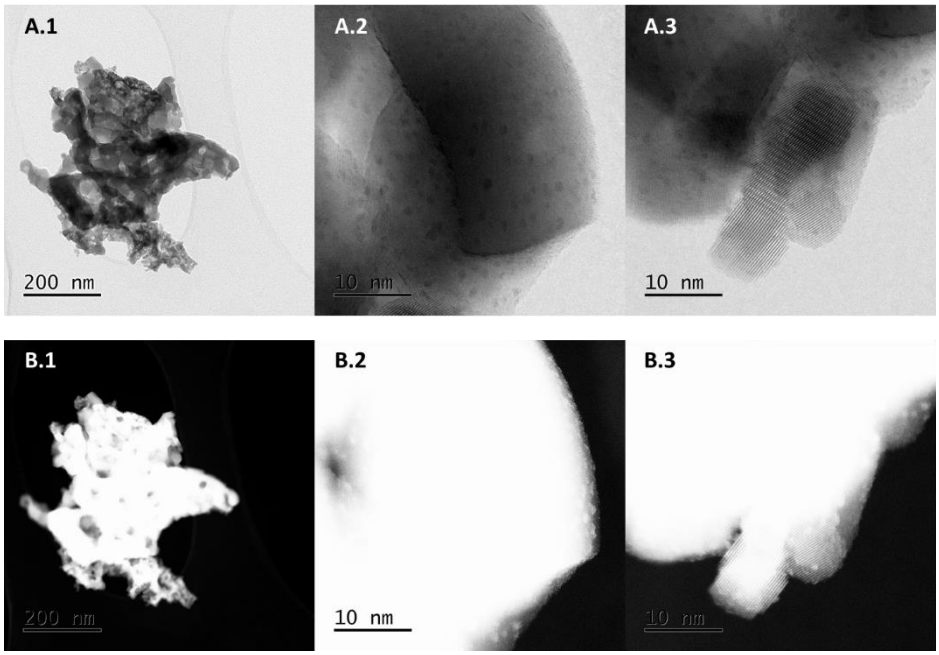

Figure 8.22: (A) Bright field TEM images and corresponding (B) HAADF images of 1.0 wt.% Pt/CeO_2 (IWI, CAN–1.00) catalyst.

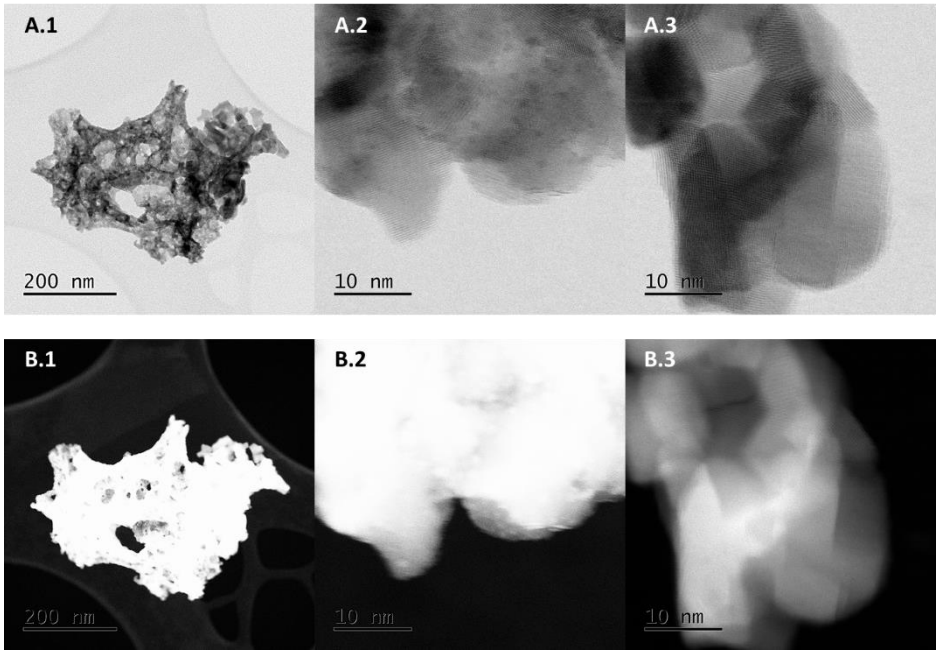

Figure 8.23: (A) Bright field TEM images and corresponding (B) HAADF images of 1.0 wt.% Pt/CeO_2 (IWI, CAN–1.25) catalyst.

C.3.1.2. Pt particle size distributions

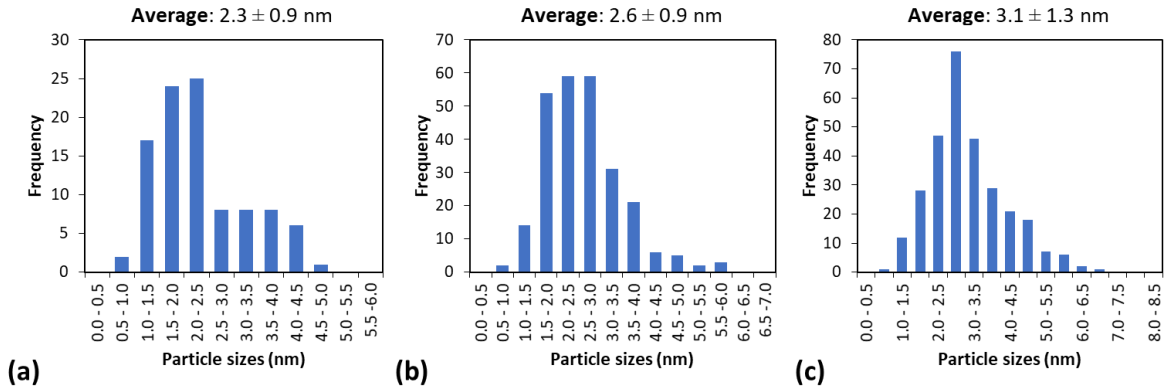

Figure 8.24: Pt particle size distributions of the SCS (CN+GLC) catalysts: (a) φ = 0.50, 99 particles counted, (b) φ = 1.00, 256 particles counted and (c) φ = 1.25, 296 particles counted.

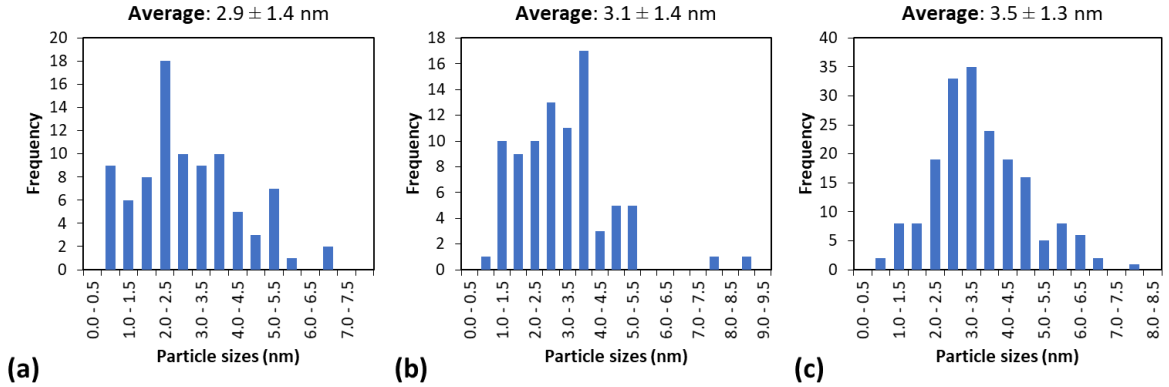

Figure 8.25: Pt particle size distributions of the SCS (CAN+GLC) catalysts: (a) φ = 0.50, 88 particles counted, (b) φ = 1.00, 86 particles counted and (c) φ = 1.25, 186 particles counted.

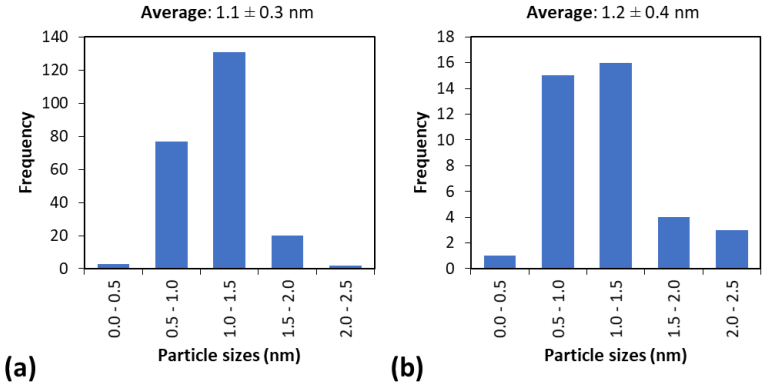

Figure 8.26: Pt particle size distributions of the IWI (CN+GLC) catalysts: (a) φ = 1.00, 233 particles counted and (b) φ = 1.25, 39 particles counted.

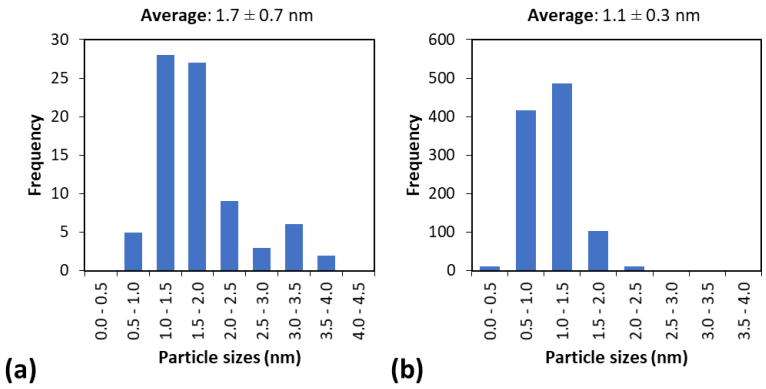

Figure 8.27: Pt particle size distributions of the IWI (CAN+GLC) catalysts: (a) φ = 0.50, 80 particles counted and (b) φ = 1.00, 1032 particles counted.

C.4 XPS Spectra

C.4.1. Theoretical Background of XPS

X-Ray Photoelectron Spectroscopy (XPS) is often used to determine oxidation states of elements of interest on the surface of a sample. It is an analytical technique based on the photoemission process. X-Rays are used to irradiate a surface under an Ultra-High Vacuum (UHV). The incident X-Ray collides with a valence and/or core electron in a surface species. If energy of the X-Ray is sufficient, the electron is excited and emitted from the electronic shell with a specific kinetic energy. This excitation process is called the photoelectric effect (see Figure 8.28 below). The ejection of inner core electrons leads to a secondary emission process. The ejected core electrons leave an unstable hole in the electronic shell of the atom. An electron from the valence band will 'relax' and fill the unstable. To conserve energy, an Auger electron is emitted from the valance band. Auger emissions occur roughly 10^{-14} s after the photoelectric event (Wagner *et al.*, 1979).

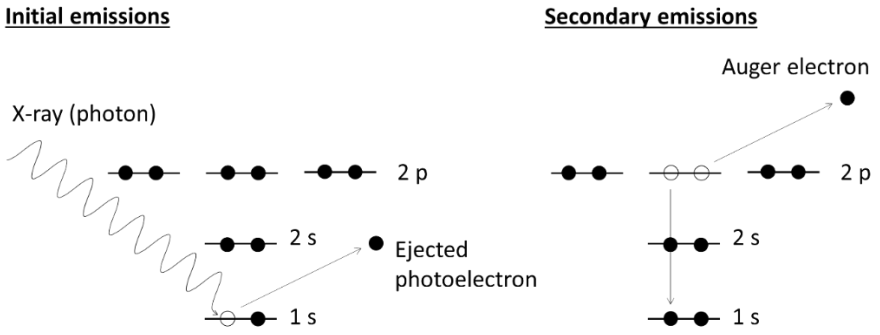

Figure 8.28: Photoelectric Effect: Initial adsorption of a photon and resultant ejection of an Oxygen 1s level photoelectron and the secondary emission of an Auger electron due to relaxation.

The kinetic energies of all the emitted photoelectrons are measured by the instrument. The electrons' kinetic energies (KE) are directly related to their binding energies (BE) by the following equation (Einstein, 1905):

$$hv = KE + BE + \varphi_{spectrometer} \qquad \text{Equation 8.23}$$

$$v = \frac{c_{light}}{\lambda} \qquad \text{Equation 8.24}$$

where h is Planck's constant, v is the frequency of the incident X-Rays which can be calculated from Equation 8.24, c is the speed of light, λ is the wavelength of the incident X-Rays and $\varphi_{spectrometer}$ is the work function of the analyser. The work function is the minimum energy required to emit an electron from the instrument, assuming a conductive sample is analysed (van der Heide, 2011). The work function is defined by the Fermi level of a conductive sample; this phenomenon provides the energy reference used in the measurement of the energy of the electrons. The work function is hence unique to the spectrometer used.

X-Rays will only penetrate several micrometres into the surface (Wagner *et al.*, 1979). For the photoelectrons to be detected, they need to escape from the surface. Interaction with the overlaying atoms results in inelastic scattering. The Beer-Lambert law approximates the probability of a photoelectron reaching the surface of the solid sample without losing any of its KE:

$$I_{depth\ d} = I_0 e^{-\frac{d}{\lambda_{IMFP}}}$$ Equation 8.25

where $I_{depth\ d}$ is the intensity of the photoelectrons originating from a depth d, I_0 is the intensity of the photoelectrons emanating from the surface atoms and λ_{IMFP} is the Inelastic Mean Free Path (IMFP). The IMFP is the average distance a photoelectron of a specific KE can travel in a solid before it interacts and losses energy to the surroundings. The Beer-Lambert law is based on the original finding by (Bouguer, 1729), but later restated by Lambert and reformulated by Beer. Typical escape depths of photoelectrons are in the order of a few angstroms (Wagner *et al.*, 1979). Therefore, XPS is an extremely surface sensitive technique.

XPS Spectral Features

XPS spectra are typically given as intensity (counts per second) as a function of BE (see Figure 8.29).

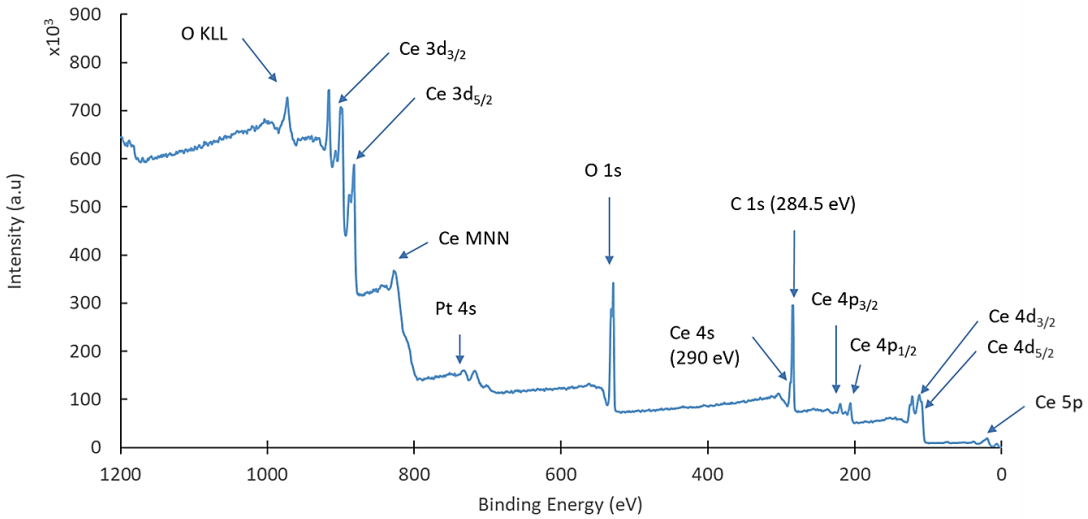

Figure 8.29: Survey spectra of SCS (CAN+GLC, 1) catalyst.

Because BEs decrease with increasing KE, the x-axis scale is conventionally plotted with decreasing BE from left to right (see Figure 8.29). XPS spectra contains a large, persistent background signal due to the inelastic scattering of electrons. The spectra can be divided into two main regions: (1) Auger peaks from secondary electron emissions and (2) photoelectron core level and valence band peaks from the initial electron emission process. Auger peaks exhibit complex patterns and appear in the higher BE range. The kinetic energy of the Auger electrons is independent of the ionizing radiation; thus, their peak positions are dependent on the photoelectron energy used and vary with different X-Ray sources. On the other hand, the photoelectron peaks are independent of the photoelectron energy used. They are sharp intense peaks, unique in shape and location for core shell and each element. These peaks are used in spectral analysis.

Photoelectron peaks are not sharp straight lines, but rather exhibit a Lorentzian function line shape. This natural broadening of the photoelectron peak is due to the lifetime of the core hole state left by the photoemission process. The natural line width (ΔE_0) is estimated by the uncertainty principle (Hofmann, 2013).:

$$\Delta E_0 = \frac{h}{\tau}$$ Equation 8.26

where h is Planck's constant in eV and τ is the lifetime of the core hole in seconds. A typical core lifetime of 10^{-14} s corresponds to a natural line width of 0.4 eV. Sample and instrumental features also introduce broadening of the photoelectron peaks. Crystalline materials exhibit a Gaussian broadening due to atomic vibrations. Instrumental line broadening is a function the type of analyser. As a result, XPS spectra are fitted using a combination of both types of line shapes.

One of the features of photoelectron peaks is multiplet splitting. Multiplet splitting is formation of a doublet photoelectron peak due to spin-orbital coupling which occurs for the p (n = 2), d (n = 3) and f (n = 4) orbitals. The electrons in these orbitals can have two different energy states due to the different possible spin states (parallel or anti-parallel). This energy difference resolves into a doublet photoelectron peak with an energy separation. Depending on the electron spin states, the electron spin quantum number (s) can either be +½ or –½. Hence, the total angular momentum (j) of an electron can have two different states as given by the formula below:

$$j = l + s$$ Equation 8.27

where (l) is the electron angular momentum. The electron angular momentum is given by the principal quantum number (n):

$$l = n - 1$$ Equation 8.28

For example, the 4f orbital (n = 4, l = 3) splits into two different energy states j = 5/2 and j = 7/2. The two energy states are annotated as $4f_{7/2}$ and $4f_{5/2}$. The ratio of the intensities of the doublet peaks are determined by the occupation probability of the two energy states which is expressed as the multiplicity (M):

$$M = 2j + 1$$ Equation 8.29

Hence, the intensity ratio ($M_{7/2}/M_{5/2}$) of 4f doublet is 4:3. This ratio can be calculated for each of the p, d and f orbital and is the same for all elements (Hofmann, 2013). However, the energy separation of each energy state – the energy separation between the doublet peaks – is unique to each element. This energy separation of the two adjacent peaks increases with atomic number for the same orbital (Hofmann, 2013).

Furthermore, a shift in the observed BE of a photoelectron peak from the referenced BE provides information about the chemical state (oxidation state) of element of interest. Withdrawal of valence electrons results in a shift towards higher binding energies; addition of valence electrons results in a shift towards lower binding energies (Hofmann, 2013).

Background subtraction models

There are three types of background subtraction models: linear, Shirley and Tougaard (Wagner *et al.*, 1979; van der Heide, 2011; Hofmann, 2013). Linear subtraction is a straight-line subtraction between the two endpoints of a peak (see Figure 8.30). Linear background subtraction is not common as it is physically unrealistic although simple and convenient (Hofmann, 2013). The Shirley

approach (Shirley, 1972) assumes a S-shaped background per peak based on a subjective weighted average approach. This type of signal shape is based on the assumption that the background signal is mainly due to the inelastic scattering of photoelectrons which is a more realistic approach than the Linear subtraction method (Wagner *et al.*, 1979; van der Heide, 2011; Hofmann, 2013). The Tougaard method (Tougaard, 1988) is more physically realistic as it mathematically approximates of the inelastic scattering of photoelectrons taking into account their initial energy distribution. However, this method requires a large energy range (50 eV) for a reasonable fit (Hofmann, 2013).

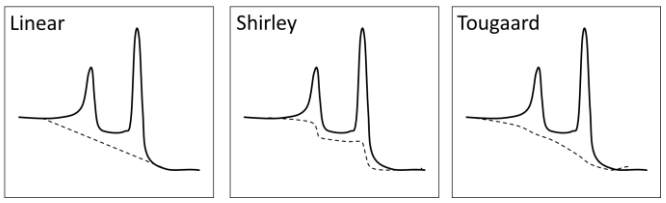

Figure 8.30: The Linear, Shirley and Tougaard spectral background subtraction methods.

Charge compensation

When measuring an insulating material, the continued exposure to the X-ray beam results in differential charging over the analysed area (Wagner *et al.*, 1979; van der Heide, 2011; Hofmann, 2013). A positive charge builds up as photoelectrons are emitted during the photoemission process but are not replaced through the connection to the analyser. This problem of charge build-up does not exist for conductive materials because the Fermi levels of the sample and the analyser are the same. The conduction band of insulators is empty, hence such a connection to the analyser does not exist. This causes charge accumulation on the surface of the sample which causes a shift in the Fermi potential. As a result of differential charging, the KE of the emitted photoelectrons decreases resulting in broadened photoelectron peaks which are shifted towards higher BEs. Spectral analysis of the photoelectron peaks becomes challenging as the there is a significant difference between the measured and the referenced BE values (Hofmann, 2013). Most commonly, charge build-up is counteracted by replacing the emitted electrons by co-irradiating the surface of the sample with a low-energy electron flood gun (Wagner *et al.*, 1979; van der Heide, 2011; Hofmann, 2013). This shifts the measured photoelectron peaks back towards lower BEs. Nonetheless, post-measurement charge compensation is still required to shift the photoelectron peaks towards lower BEs with reference to an internal standard which is commonly the C 1s photoelectron peak (Metson, 1999).

C.4.2. Raw XPS Spectra

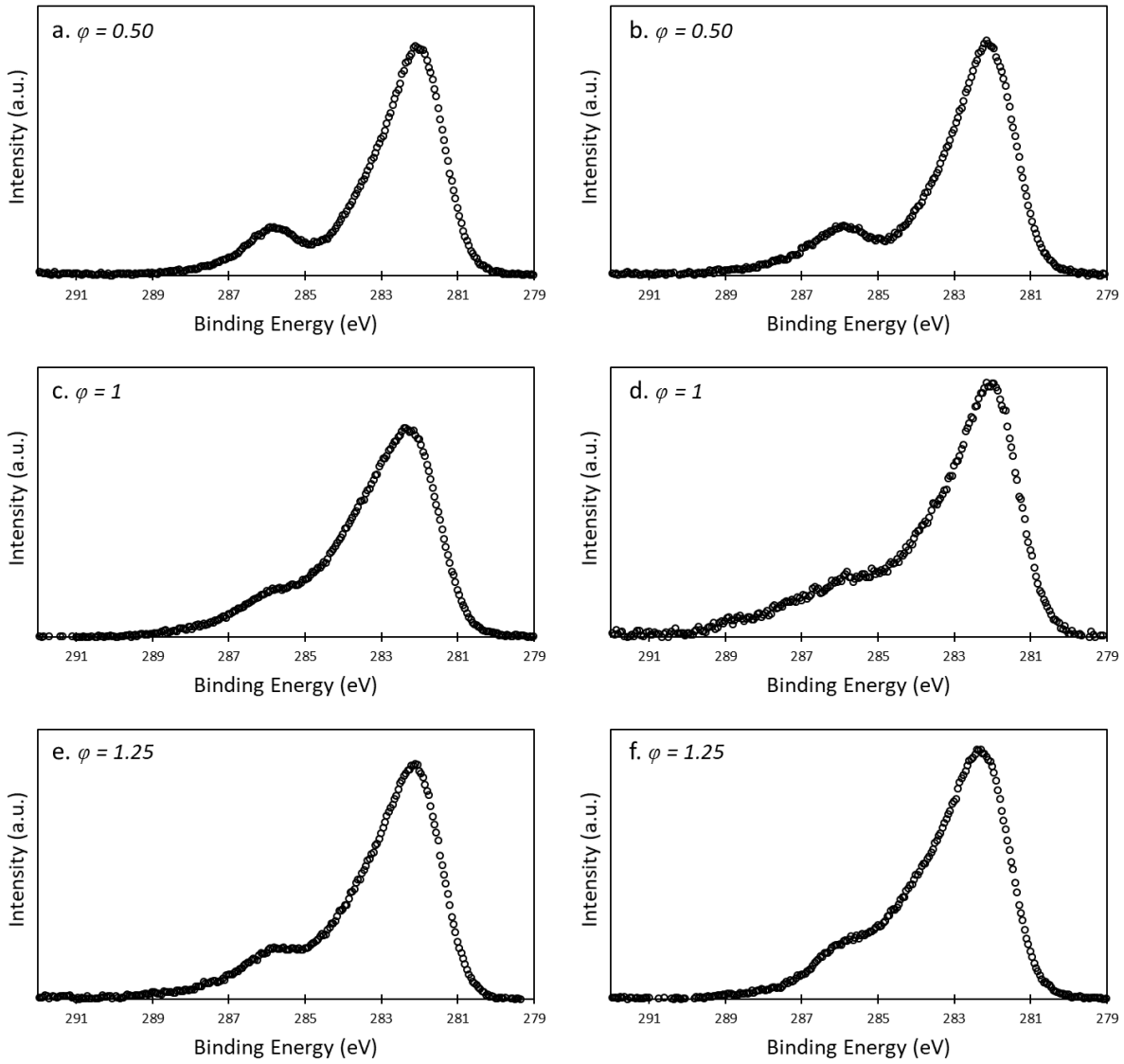

Figure 8.31: Raw C 1s spectrum of the (a, c, e) SCS (CAN+GLC) catalysts and (b, d, f) SCS (CN+GLC) catalysts.

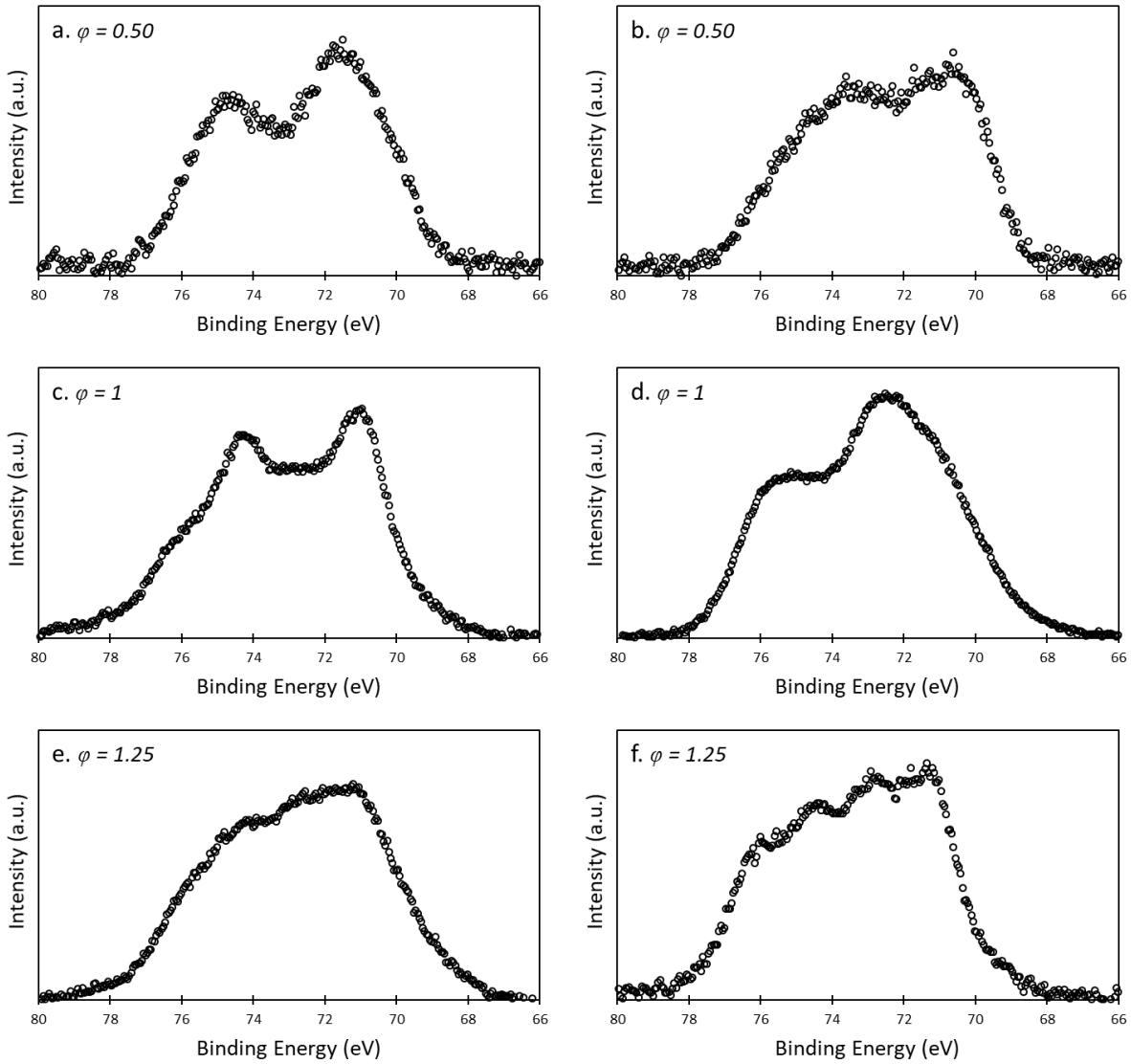

Figure 8.32: Raw Pt 4f spectrum of the (a, c, e) SCS (CAN+GLC) catalysts and (b, d, f) SCS (CN+GLC) catalysts.

C.4.3. Fitted Peak Parameters

Table 8.3: C 1s Fitted Singlet Peak Parameters

Catalyst	**Species**	**Binding energy $4f_{7/2}$ (eV)**	**FWHM (eV)**	**GL Ratio (%)**
SCS (CAN+GLC, 0.5)	C-C, C-H	281.9	1.4	7.9%
	-COH, -COC	283.1	1.9	7.5%
	-C=O	-	-	-
	-OC=O	285.8	1.8	55%
SCS (CAN+GLC, 1)	C-C, C-H	282.2	1.6	5%
	-COH, -COC	283.5	1.6	5%
	-C=O	284.9	2.5	81%
	-OC=O	286.3	2.1	31%
SCS (CAN+GLC, 1.25)	C-C, C-H	282.0	2.0	5%
	-COH, -COC	283.2	2.0	5%
	-C=O	284.7	1.6	5%
	-OC=O	285.9	2.2	87%
SCS (CN+GLC, 0.5)	C-C, C-H	282.0	1.5	5%
	-COH, -COC	-	-	-
	-C=O	284.7	0.4	30%
	-OC=O	286.0	2.0	88%
SCS (CN+GLC, 1)	C-C, C-H	282.0	1.6	5%
	-COH, -COC	283.5	1.6	5%
	-C=O	284.7	1.7	95%
	-OC=O	286.1	2.5	95%
SCS (CN+GLC, 1.25)	C-C, C-H	282.1	1.5	5%
	-COH, -COC	283.3	2.4	5%
	-C=O	284.8	1.7	30%
	-OC=O	285.9	2.2	30%

Table 8.4: Pt 4f Fitted Doublet Peak Parameters

Catalyst	**Species**	**Binding energy $4f_{7/2}$ (eV)**	**Relative Intensity (%)**	**FWHM (eV)**
SCS (CAN+GLC, 0.5)	Pt^0	71.7	9%	2.5
	Pt^{2+}	73.9	75%	2.5
	Pt^{4+}	75.3	16%	2.5
SCS (CAN+GLC, 1)	Pt^0	71.5	3%	1.3
	Pt^{2+}	73.3	54%	1.8
	Pt^{4+}	75.1	43%	2.1
SCS (CAN+GLC, 1.25)	Pt^0	71.7	11%	2.2
	Pt^{2+}	73.6	53%	2.4
	Pt^{4+}	75.3	36%	2.1
SCS (CN+GLC, 0.5)	Pt^0	70.7	0%	0.9
	Pt^{2+}	72.6	37%	1.8
	Pt^{4+}	74.2	62%	2.5
SCS (CN+GLC, 1)	Pt^0	71.5	6%	2.2
	Pt^{2+}	73.5	52%	2.5
	Pt^{4+}	75.1	42%	2.0
SCS (CN+GLC, 1)	Pt^0	71.7	3%	1.4
	Pt^{2+}	73.6	57%	1.9
	Pt^{4+}	75.3	40%	1.8

C.5. Summary of Characterizations

Table 8.5: Summary of morphological properties of the CeO_2 supports, and IWI and SCS catalysts

Catalyst	Furnace temp. (°C)	Weight loss[a] (%)	CeO_2 crystallite size[b] (nm)	SA_{BET} (m^2/g)	Pt Loading[c] (wt.%)	Pt particle size[d] (nm)	$Pt^0{}_{47/2}$ (eV)	Area (%)	$Pt^{2+}{}_{47/2}$ (eV)	Area (%)	$Pt^{4+}{}_{47/2}$ (eV)	Area (%)
CeO_2 (CN+GLC, 0.25)	700	-	9	-	-	-	-	-	-	-	-	-
CeO_2 (CN+GLC, 0.25)	600	-	6	-	-	-	-	-	-	-	-	-
CeO_2 (CN+GLC, 0.25)	500	-	7	-	-	-	-	-	-	-	-	-
CeO_2 (CN+GLC, 0.25)	400	-	6	-	-	-	-	-	-	-	-	-
CeO_2 (CN+GLC, 0.5)	400	2.87%	8	28	-	-	-	-	-	-	-	-
CeO_2 (CN+GLC, 1)	400	1.38%	25	28	-	-	-	-	-	-	-	-
CeO_2 (CN+GLC, 1.25)	400	1.17%	21	24	-	-	-	-	-	-	-	-
CeO_2 (CAN+GLC, 0.5)	400	3.45%	14	32	-	-	-	-	-	-	-	-
CeO_2 (CAN+GLC, 1)	400	0.81%	39	11	-	-	-	-	-	-	-	-
CeO_2 (CAN+GLC, 1.25)	400	0.97%	27	17	-	-	-	-	-	-	-	-
SCS (CN+GLC, 0.5)	400	2.61%	9	24	1.04 %	2.3 ± 0.9	71.7	9%	73.9	75%	75.3	16%
SCS (CN+GLC, 1)	400	0.74%	34	11	0.96 %	2.6 ± 0.9	71.5	3%	73.3	54%	75.1	43%
SCS (CN+GLC, 1.25)	400	0.86%	35	11	1.04 %	3.1 ± 1.3	71.7	11%	73.6	53%	75.3	36%
SCS (CAN+GLC, 0.5)	400	2.48%	12	34	0.88 %	2.9 ± 1.4	70.7	0%	72.6	37%	74.2	62%
SCS (CAN+GLC, 1)	400	0.61%	40	9	0.96 %	3.1 ± 1.4	71.5	6%	73.5	52%	75.1	42%
SCS (CAN+GLC, 1.25)	400	0.70%	36	9	0.96 %	3.5 ± 1.3	71.7	3%	73.6	57%	75.3	40%
IWI (CN+GLC, 0.5)	-	-	9	26	1.08 %	-	-	-	-	-	-	-
IWI (CN+GLC, 1)	-	-	25	26	0.93 %	1.1 ± 0.3	-	-	-	-	-	-
IWI (CN+GLC, 1.25)	-	-	27	24	1.02 %	1.2 ± 0.4	-	-	-	-	-	-
IWI (CAN+GLC, 0.5)	-	-	14	37	0.88 %	1.7 ± 0.7	-	-	-	-	-	-
IWI (CAN+GLC, 1)	-	-	44	12	0.96%	1.1 ± 0.3	-	-	-	-	-	-
IWI (CAN+GLC, 1.25)	-	-	34	18	0.63 %	-	-	-	-	-	-	-

[a] Determined from thermogravimetric measurements

[b] Calculated from X-ray line broadening of the (111) reflection using the Scherrer equation $d = K\lambda/\beta cost\theta$

[c] Determined from ICP-AES

[d] Determined from Bright Field and HAADF TEM images

Appendix D: Water Gas-Shift Activity Evaluation

This appendix provides supporting information for chapter 4.3.

D.1. Catalyst Loading Procedure

The catalysts loadings were performed as follows:

1. Marks were made along the reactor tube at 10.7 cm and 11 cm from the bottom
2. A porous quartz filter was placed at the bottom of the reactor tube to ensure the contents of the reactor tube does not to the effluent section of the Flowrence
3. Silicon carbide (300 μm) was loaded to the 10.7 cm mark. The tube was tapped to ensure compacting of the inert.
4. A 3 mm layer of quartz wool was then loaded onto of the silicon carbide bed. This ensures the catalyst bed remains separate from the silicon carbide and within the isothermal zone of the PBR.
5. The catalyst was loaded onto of the silicon carbide layer. The tube was tapped again to ensure compacting of the catalyst bed.
6. Another 3 mm layer of quartz wool was loaded onto top of the catalyst bed.
7. The reactor tube was then filled to ~ 5 mm from top with silicon carbide.

Figure 8.33 depicts the packing layers within the reactor tube.

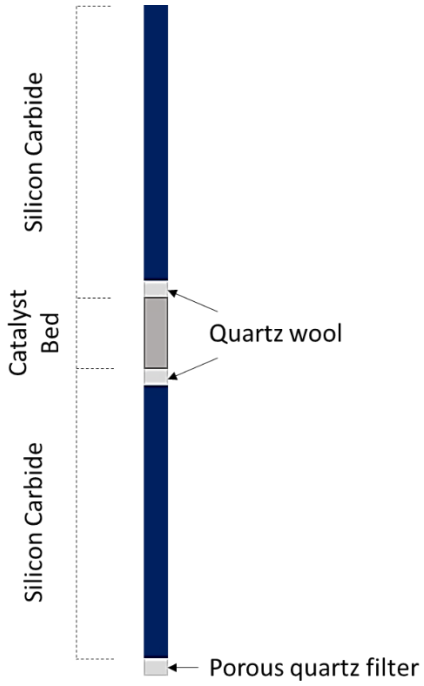

Figure 8.33: Reactor tube packing layers

D.2. WGS Temperature Programme

The operating of the Flowrence follows three main procedures:

1. Start-up (Steps A and B)
2. Catalyst performance evaluation (Steps C - J)
3. Shut down (Steps K and L)

Figure 8.34 depicts the operating procedures' individual steps and Table 8.6 corresponds to the conditions of each step.

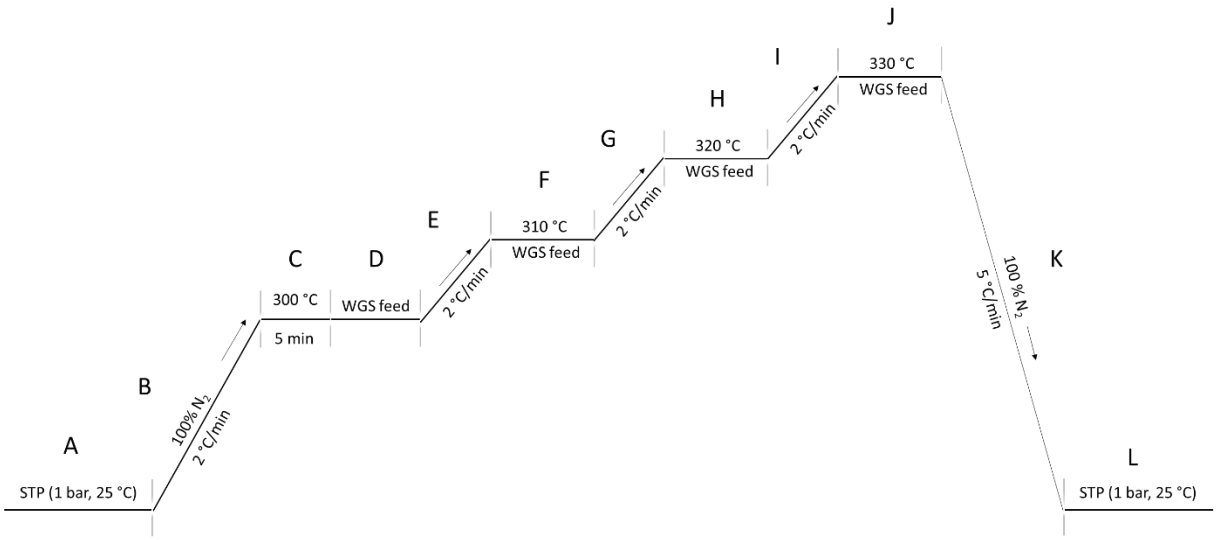

Figure 8.34: Flowrence Water Gas Shift Operating Procedure

Table 8.6: Water-Gas Shift operating procedure steps

Step	Action taken
A	Starting temperature (25 °C)
B	Increase the temperature at a 2 °C/min ramp rate under 100 % N_2 to 300 °C
C	Hold at 300 °C for 5 min to allow for temperature stabilization (this step was repeated after every increase in temperature but neglected in consequent steps for visual ease in Figure 8.34)
D	Water pump switched on and gas feed started. GC analysis started after 2 hours if stabilization
E	Increase the temperature at a 2 °C/min ramp rate to 310 °C
F	GC sampling and analysis
G	Increase the temperature at a 2 °C/min ramp rate to 320 °C
H	GC sampling and analysis
I	Increase the temperature at a 2 °C/min ramp rate to 330 °C
J	GC sampling and analysis
K	Gas feed and water pump switched off and the flow of N_2 was set to 25 ml/min per reactor. The reactors are cooled at a rate of 5 °C/min to 30 °C.
L	Heating blocks and gas flows switched off

D.3. Catalyst loading sheet

Table 8.7 below details the reactor loadings. Reactors 2 and 9 were loaded as blanks to allow for GC sampling of the feed; reactors 3 and 14 were not used within this study.

Table 8.7: Catalyst loading sheet of the IWI and SCS catalysts for the WGS activity measurements

Reactor	Catalyst code	Description	Target weight (mg)	Glass wool bedlength (mm from bottom)	Weight without catalyst (g)	Cat weight (mg)	Cat bedlength (mm from bottom)	Reactor with cat (g)
1	FP0546	SCS (CN+GLC, 1)	30	113	3.0168	-	195	3.0469
2	Blank							
4	FP0549	SCS (CAN+GLC, 1)	30	110	3.0224	30.6	175	3.0519
5	FP0552	IWI (CN+GLC, 1)	30	110	3.0128	30.6	129	3.0435
6	FP0555	IWI (CAN+GLC, 1)	30	110	2.7066	30.5	130	2.7363
7	FP0546	SCS (CN+GLC, 1)	30	112	3.0342	30.2	191	3.0647
8	FP0549	SCS (CAN+GLC, 1)	30	112	3.0216	30.5	185	3.0518
9	Blank							
10	FP0555	IWI (CAN+GLC, 1)	30	110	2.9799	30.8	138	3.0109
11	FP0546	SCS (CN+GLC, 1)	30	110	3.0107	30.2	199	3.0414
12	FP0552	IWI (CN+GLC, 1)	30	114	2.9922	30	133	3.0222
13	FP0549	SCS (CAN+GLC, 1)	30	113	3.0143	30.3	188	3.0448
15	FP0552	IWI (CN+GLC, 1)	30	114	3.0139	30.7	133	3.0446
16	FP0555	IWI (IWI, CAN–1)	30	111	3.0085	30.9	132	3.0388

Appendix E: EBE Faculty "Assessment of Ethics in Research Projects Form"

Application for Approval of Ethics in Research (EiR) Projects
Faculty of Engineering and the Built Environment, University of Cape Town

APPLICATION FORM

Please Note:
Any person planning to undertake research in the Faculty of Engineering and the Built Environment (EBE) at the University of Cape Town is required to complete this form **before** collecting or analysing data. The objective of submitting this application *prior* to embarking on research is to ensure that the highest ethical standards in research, conducted under the auspices of the EBE Faculty, are met. Please ensure that you have read, and understood the **EBE Ethics in Research Handbook**(available from the UCT EBE, Research Ethics website) prior to completing this application form: http://www.ebe.uct.ac.za/usr/ebe/research/ethics.pdf

APPLICANT'S DETAILS		
Name of principal researcher, student or external applicant		Marianne Werle van der Merwe
Department		Chemical Engineering
Preferred email address of applicant:		WRLMAR001@myuct.ac.za
If a Student	Your Degree: e.g., MSc, PhD, etc.,	MSc. (Eng)
	Name of Supervisor (if supervised):	Prof. JCQ Fletcher, N. Lutchers & JV Fletcher
If this is a research contract, indicate the source of funding/sponsorship		
Project Title		Solution Combustion Synthesis Catalysts for Propane Steam Reforming

I hereby undertake to carry out my research in such a way that:

- there is no apparent legal objection to the nature or the method of research; and
- the research will not compromise staff or students or the other responsibilities of the University;
- the stated objective will be achieved, and the findings will have a high degree of validity;
- limitations and alternative interpretations will be considered;
- the findings could be subject to peer review and publicly available; and
- I will comply with the conventions of copyright and avoid any practice that would constitute plagiarism.

SIGNED BY	Full name	Signature	Date
Principal Researcher/ Student/External applicant	Marianne Werle van der Merwe		**26 Apr 2017**

APPLICATION APPROVED BY	Full name	Signature	Date
Supervisor (where applicable)	Prof. JCQ Fletcher		**26 Apr 2017**
HOD (or delegated nominee) Final authority for all applicants who have answered NO to all questions in Section1; and for all Undergraduateresearch (Including Honours).	J. Peters		24 Ap 2017
Chair : Faculty EIR Committee For applicants other than undergraduate students who have answered YES to any of the above questions.			

Page **1** of **2**